



Dmi

Ministry of Transport and Energy

DMI Scientific Report SR-06-04

Polar Cap (PC) Index

Unified PC-N (North) Index Procedures and Quality

by

Peter Stauning (1), Oleg Troshichev (2), Alexander Janzhura (2)

(1) Danish Meteorological Institute, Copenhagen

(2) Arctic and Antarctic Research Institute, St. Petersburg

Colophon

Serial title:

Scientific Report SR-06-04

Title:

Polar Cap (PC) Index

Subtitle:

Unified PC-N (North) Index Procedures and Quality

Author(s):

Peter Stauning, Danish Meteorological Institute, Copenhagen

Oleg Troshichev and Alexander Janzhura, Arctic and Antarctic Research Institute, St. Petersburg

Other contributors:

Ole Rasmussen, Lars William Pedersen and Svend-Erik Ascanius, DMI

Responsible institution:

Danish Meteorological Institute (DMI)

Language:

English

Keywords:

Polar Cap Index, PCN index, Polar magnetic disturbances, Geomagnetism, Solar Wind

Url:

www.dmi.dk/dmi/sr_06-04

Digital ISBN:

87-7478-537-0

ISSN:

1399-1949

Version:

Revised 10.10.2007

Website:

www.dmi.dk

Copyright:

DMI

Contents:

Abstract.....	2
Resumé.....	2
1. Introduction.....	3
2. Solar wind satellite observations.....	7
3. Processing of QL values for PC index calculations,,,	17
4. Optimum angle calculations.....	25
5. Calculation of slope and intercept.....	32
6. Calculation of Polar Cap (PCN) index.....	40
7. Quality of PCN index.....	48
Summary and conclusions.....	59
References.....	60
Previous reports.....	61

Polar Cap (PC) Index

Abstract.

Basically, the Polar Cap (PC) index is derived from polar magnetic variations from the quiet level. The PC index values are calibrated on a statistical basis to approximate values in units of mV/m of the interplanetary "merging" (or "geo-effective") electric field ($V_{sw}B_T \sin^2(\theta/2)$) conveyed by the solar wind. The PC index is a measure of the intensity of the transpolar ionospheric current related to the polar cap antisunward ionospheric plasma convection driven by the dawn-dusk electric field generated by the solar wind. The index thus provides a measure of the global magnetic activity related to solar wind conditions. The PC index can be used to analyze magnetically disturbed conditions and provide forecast of geomagnetic storms.

The Polar Cap index was originally introduced by Troshichev and Andrezen (1985) in order to derive a measure for the geo-effective interplanetary electric field from available polar ground-based magnetic observations. The PC index concept was further developed by Vennerstrøm (1991) and Vennerstrøm et al. (1994). They derived coefficients to calculate a PC-N (North) index from Thule magnetic data. The development of a PC index was recommended by IAGA in 1999 and the index was later adopted by IAGA on the condition that the derivation of PC-S (South) and PC-N (North) indices was unified, and a joint procedure for the PC index calculations was defined. This unification has now been accomplished through cooperation between the Arctic and Antarctic Research Institute (AARI), St. Petersburg, and the Danish Meteorological Institute (DMI). The PCN index data are available from the Wold Data Center WDCC1 at DMI back to 1975. Since the calculation procedure requires 3 months of data (past, current and following month) to check the quality of all data and produce the best possible reference quiet level (QL) then PCN data from present year are preliminary values only and will be replaced by final values in due time (in the beginning of every new year).

Resumé

The present report gives a description of the adopted unified procedures for processing of polar magnetometer data and interplanetary satellite observations to derive scaling parameters for PC index calculations. The report analyzes properties of the IMP 8, WIND and ACE satellite interplanetary magnetic field and solar wind velocity data used in correlation statistics to calibrate PC index values against the so-called merging electric field. Diagrams and tables of the relevant parameters used for the PCN index calculations are provided in the report. In a final chapter the quality of the derived PCN index is examined thoroughly.

1. Introduction

Around 95% of the geomagnetic field observed at a ground-based observatory arises from the main field generated within the Earth's fluid core. This part varies on time scales of tens or hundreds of years (secular variations). A further few percent of the total field arises from magnetization (induced and remnant) in the crust. The induced part varies with the main field while the remnant part varies on geological time scales (millions of years). Another few percent of the total field is generated by currents in the upper atmosphere and further out. This fraction shows variations on time scales spanning from fraction of a second to a few years. The large differences in time scales is one of the tools used to separate the different contributions.

The ionospheric and magnetospheric currents causing variations in the geomagnetic field observed near either geomagnetic pole depend to a large degree on the conditions in the solar wind plasma and its embedded interplanetary magnetic field (IMF). Their intensities also depend on location of the observatory as well as local time and season partly because of the changing upper atmospheric ionization depending, among other, on the varying solar illumination and partly because of the varying geomagnetic field morphology relative to the solar wind flow (e.g., varying tilt of dipole axis).

Typical examples of polar geomagnetic observations are presented in Fig. 1.1. The three top fields display the data from Thule, Greenland, located at corrected geomagnetic (CGM) latitude of 85.30° . The next three fields display data from Vostok, Antarctica, located at corrected geomagnetic latitude of -83.44° . The blue traces in the two sets of three top fields in the diagram show hourly average values of the field resolved in the H-component (geomagnetic North), D-component (East) and Z-component (down for Thule, up for Vostok) through the year 2001.

Hourly values of the interplanetary magnetic field at the Earth's position derived from the OMNI data base for the same year, 2001, are shown in the three bottom fields. These magnetic data are resolved in Geocentric Solar Magnetospheric (GSM) coordinates, B_X (toward the Sun), B_Y (perpendicular to the Earth-Sun line and to the Earth's magnetic dipole axis) and B_Z (completing an orthogonal system, almost in the direction of the (negative) dipole axis). Throughout the diagrams in Fig. 1.1. the red continuous curves depict smoothed averages.

In these data several features are noteworthy:

- (i) The polar magnetic data, particularly the D -component of the Thule observations, display significant steady changes through the year. This is the result of secular variations in the main field.
- (ii) There is a low-frequency modulation on time scales from one to a few weeks in as well the ground-based Thule and Vostok data, seen most distinctly in the Z -component, as in the interplanetary B_X and B_Y magnetic field components. This modulation is indicative of the interplanetary sector structure where the preferred field direction is either toward or away from the Sun. The associated change in the polar magnetic field is the so-called Svalgaard-Manzurov effect.
- (iii) Strong high-frequency excursions, here on time scales of one or a few hours, are seen in all three components of the ground-based data as well as in the interplanetary data. In the ground-based data for Thule these excursions are strongest during the northern summer months occurring at the middle of the diagram. In the data from Vostok, correspondingly, the strongest excursions are seen in the southern summer months occurring at either ends of the diagram. The excursions observed at ground and in space are strongly correlated. This correlation is the fundamental basis for defining a Polar Cap (PC) index.

The highest degree of correlation between polar cap horizontal magnetic field variations F and various constellations of solar wind parameters is found to exist between F and E_M , the so-called "Merging (or "Geo-effective") Electric Field", MEF .

$$E_M = MEF = V_{SW} B_T \sin^2(\theta/2) \quad (1.1)$$

where V_{SW} is the solar wind velocity, B_T is the transverse component of the IMF ($B_T = \sqrt{B_Y^2 + B_Z^2}$), while θ is the polar angle between the Z -axis of a Geocentric Solar-Magnetospheric (GSM) coordinate system and the transverse IMF component.

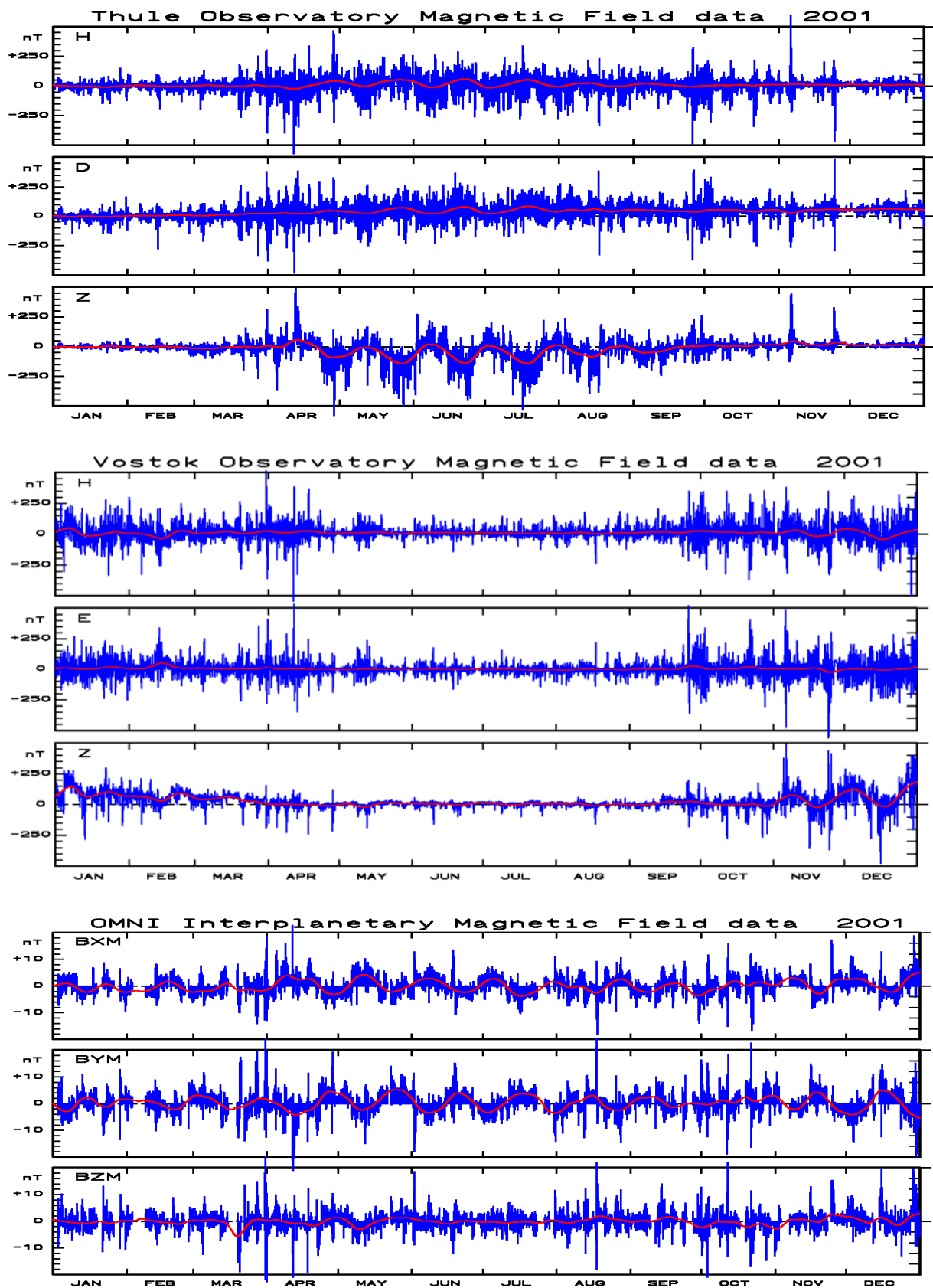


Figure 1.1. Polar geomagnetic field measurements from observatories in Thule, Greenland, and Vostok, Antarctica, and OMNI interplanetary magnetic field data base. Hourly values 2001.

A simplified physics-based explanation of the correlation between geophysical disturbances and the quantity defined by Eq. 1.1 can be given with reference to the schematic representation in Fig. 1.2. (from GEM Source Book) of the structure, current systems and magnetic fields in the Earth's magnetosphere exposed to the solar wind flow. The solar wind electric field ($\mathbf{E}=\mathbf{V}\times\mathbf{B}$) extends over the Earth's magnetosphere. However, the interaction is strongly enhanced by a southward ($\theta=180^\circ$) IMF since this direction favors merging with the northward, and thus oppositely directed, geomagnetic field at the frontal magnetopause boundary. The merging of magnetic fields enhances the entry of solar wind plasma into the magnetospheric regions. This explains the construction in Eq. 1.1. of the merging (geoeffective) electric field.

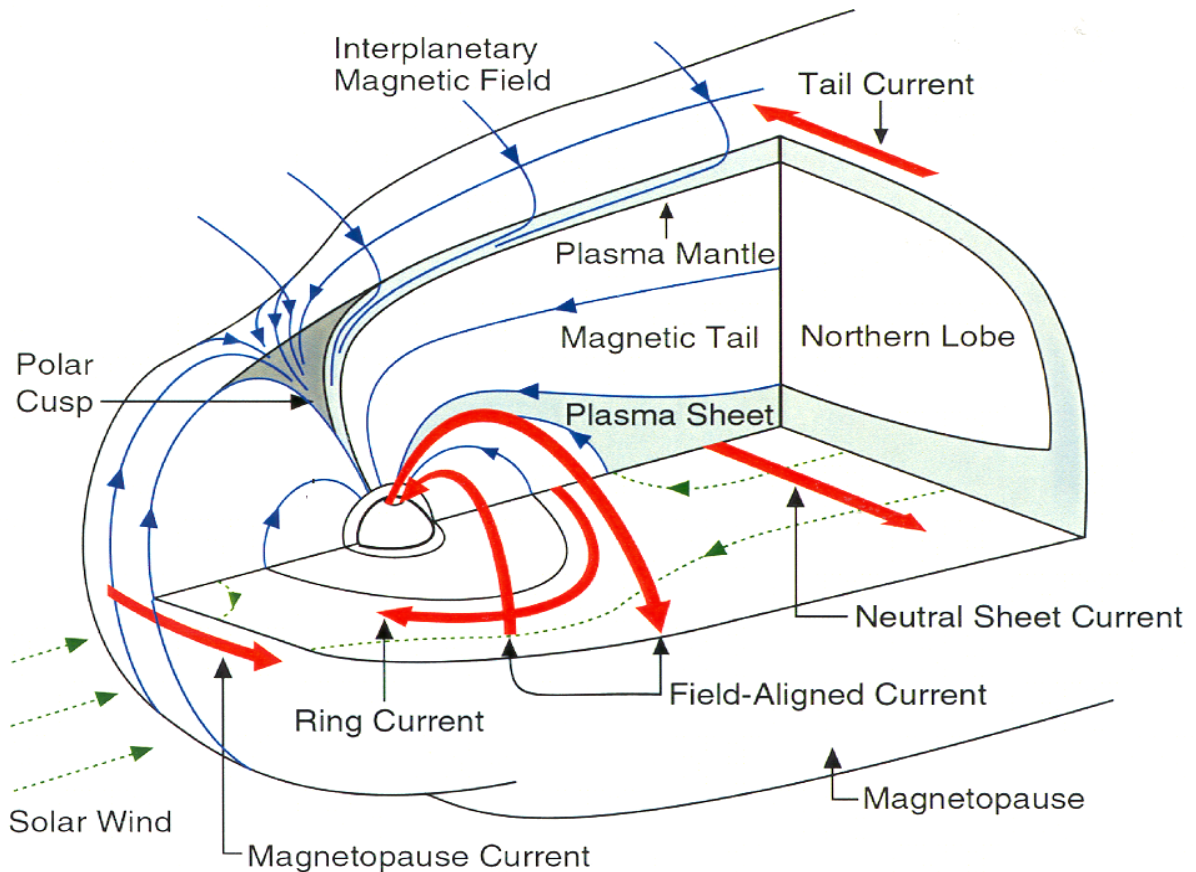


Figure 1.2. Simplified sketch of magnetospheric structure (from GEM Source Book)

This field extending from dawn to dusk drives currents along field lines from the outer magnetospheric regions interfacing the solar wind to the northern and southern polar ionospheres. The dominant type of such field-aligned currents (FAC) are the so-called "Region 1" FAC generated in the "Low-Latitude Boundary Layer" (LLBL) regions. The precise generation mechanism is still open for discussion. However, there is a close statistical relation between these currents and the merging electric field.

The projected ionospheric intensities of such field-aligned currents (FAC) detected from satellites are shown in colour code in Fig. 1.3. together with the accompanying electric potential distribution for cases where the IMF is directed in the azimuthal directions ($\theta=-90^\circ$, $\theta=+90^\circ$). The two cases both represent the typical two-cell polar convection vortex structure which is the prevailing mode except during cases of strong northward IMF.

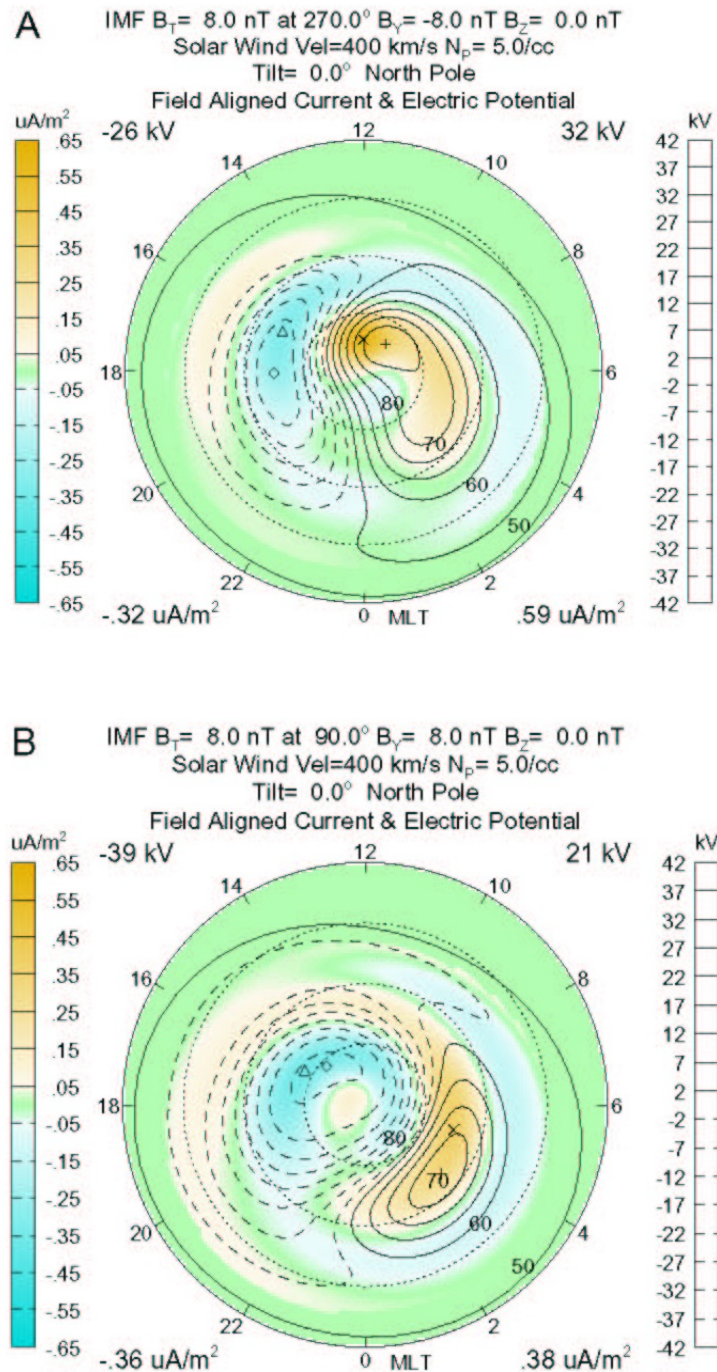


Figure 1.3. North-polar field-aligned currents and electric potential distribution in typical cases with IMF $B_Y < 0$ (A) and IMF $B_Y > 0$ (B), respectively. [Weimer, 2001]

The strongly yellow colored region at the morning side at $70^\circ - 80^\circ$ (geomagnetic) latitude indicates the location of the downward Region 1 (R1) FAC while the strongly blue colored region at the dusk side represents the upward R1 FAC leaving the ionosphere. These two R1 FAC currents are partly connected via dawn-dusk Pedersen currents flowing horizontally in the polar ionosphere. The electric potential distribution, in addition, drives an ionospheric convection largely along equipotential contours. Due to differences in ion and electron mobility (the ions are more impeded by the neutral atmosphere than the electrons), the convection is equivalent to an oppositely directed Hall current system closing within the ionosphere. The magnetic variations measured at ground level are dominated by the contributions from the Hall currents since the contributions from the Pedersen currents are reduced by the contributions from the associated FAC's. The polar magnetic variations are related to the solar wind *MEF* through the steps outlined above.

Additionally, like seen in Fig. 1.3., the direction of the convection or of the equivalent ionospheric current in the central polar cap depend on the sign of azimuthal component, IMF B_y , of the interplanetary magnetic field. For similar numerical values but opposite sign in IMF B_y the convection, and hence the ionospheric currents are equally strong, but shifted in clockwise direction for the northern hemisphere going from negative to positive IMF B_y . Accordingly, for dealing correctly with the sector structure modulation this shift in angle must be compensated for as part of the data processing.

The two top fields in Figure 1.4. present the variation of the total magnitude of the disturbance vector HH and the angle "DD" between the disturbance vector and a fixed direction in space, that is, a fixed direction in diagrams like Figure 1.3. The raw data (hourly values) have been plotted in blue line while the running averages over around 10 days have been plotted in red line. The cyclic modulation, which indicates the sector structure, is clearly seen in the Z-component in the bottom field. It is also seen clearly in the figure that the angle DD displays the sector structure modulation as the running average (red line) alternate between angles indicative of preferred either positive or negative IMF B_y levels. A positive IMF B_y value gives a negative perturbation of the angle DD. The effects in the amplitudes of the H and D components seen in Fig. 1.1. relate to the change in convection direction with the IMF B_y component as indicated in Fig. 1.3. The positive peak in H (or D) occurs when the local magnetic North (or East) direction is aligned with the magnetic perturbation vector generated by the transpolar Hall current (i.e., the convection direction rotated 90° CW). For any given level of the merging electric field (which is independent of the sign of IMF B_y) a positive IMF B_y value rotates the transpolar convection in the clockwise (CW) direction. Hence, the positive peaks in H or D occur earlier in local time, that is, closer to local noon, and are therefore enhanced due to the normal daily variation in the response to the merging electric field (see Chap. 5). The negative peaks, correspondingly, occur closer to midnight and are therefore reduced in amplitudes. In Fig. 1.4 the values of the disturbance vector projected to the "Optimum Direction" (see Chap. 4) are displayed in the second field from bottom.

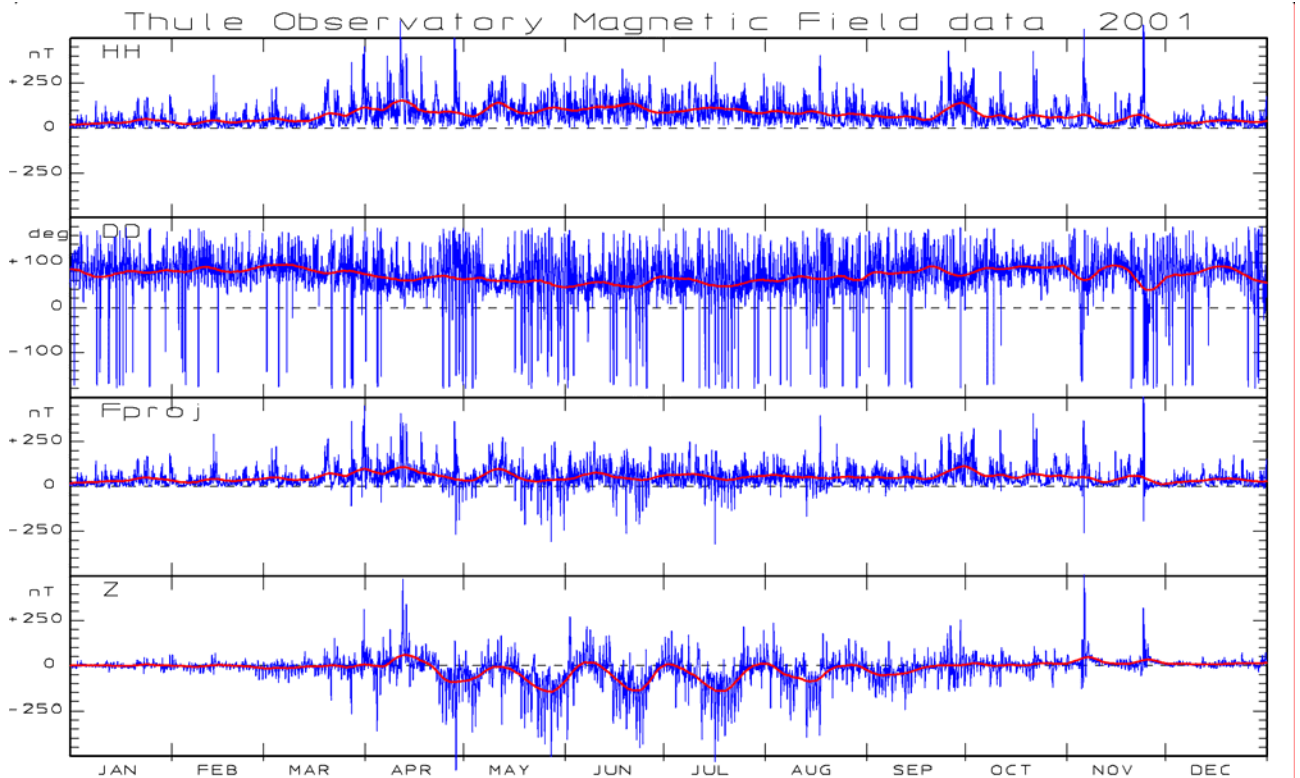


Figure 1.4. Polar geomagnetic field measurements from the observatory in Thule, Greenland.. Hourly values of the magnitude, HH , of the disturbance vector, the angular displacement in a Sun-Earth system, DD , the projected disturbance vector $Fproj$ and the vertical component, Z , through 2001. Raw data are plotted in blue line. Running averages are plotted in red line.

2. Solar Wind satellite observations.

During the time interval from 1975 to present, where high-quality digital magnetic data are available from Thule or Vostok there are three main sources of solar wind plasma and interplanetary magnetic field data. These sources are IMP 8, WIND and ACE satellite data.

2.1. IMP 8 satellite

The IMP 8 satellite was launched 1973-10-26 into an orbit with inclination varying between 0 deg and 55 deg. Apogee and perigee were around 40 and 25 earth radii, respectively. Data are available up to year 2000. The spacecraft was located in the solar wind for 7 to 8 days of every 12.5 days orbit. Telemetry coverage has been varying between around 60 and 90%. With around 25 years (i.e. more than two solar activity cycles) of steady operation and stable orbit conditions in positions relatively near to the Earth, but still in the undisturbed solar wind during most of the time, this satellite, compared to Wind and ACE, provides by far the best basis for statistical studies of relations between solar wind parameters and polar geomagnetic disturbances. The daily variation in the availability of IMP-8 magnetic field and solar wind velocity data is illustrated in Fig. 2.1. For each year along the horizontal axis the field has a UT time scale ranging from 00 to 24 UT.

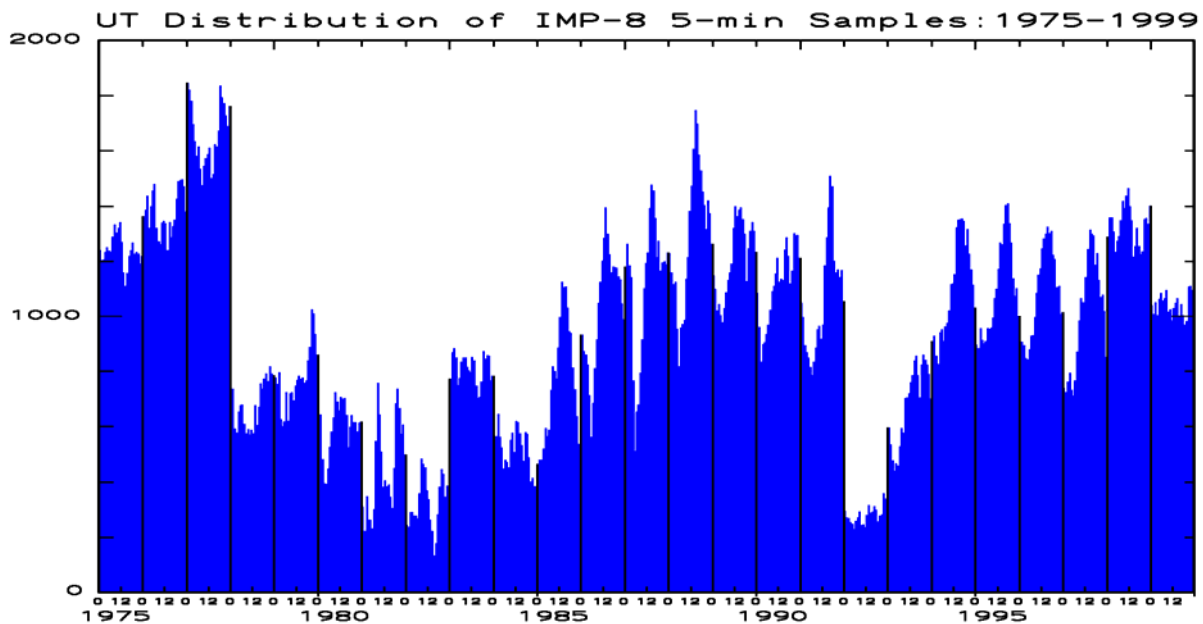


Figure 2.1. Daily (UT) variation in the availability of IMP-8 magnetic field and solar wind velocity data during years 1975-1999 combined into 5-min samples of the merging electric field (MEF).

2.2. Wind satellite

The Wind satellite was launched 1994-11-01 to spend the first 9 months of operation (1995) in a double-lunar swing-by orbit near the ecliptic plane, with apogee from 80 to 250 Re and perigee ranging from 5 to 10 Re. During the next couple of years Wind was inserted in a halo orbit around the L1 point in front of the Earth at a distance varying from 235 to 265 Re. During more recent years Wind has been moved around to various positions ranging from orbits near the frontal magnetopause and near-Earth tail to highly eccentric orbits taking the satellite far away from the Sun-Earth line.

In this report we have analyzed Wind magnetic data and solar wind velocity data from 1995 through 2004. The drastic changes in satellite orbit make the data less useful for studies involving long-term correlation with ground-based observations. However, the strongly varying satellite position provides unique opportunities to investigate the effects of variations in the distance between the satellite and the Earth along the Sun-Earth line (varying delay) as well as variations in solar wind uniformity with the transverse distance from the Sun-Earth line.

2.3. ACE satellite

The ACE satellite was launched 1997-08-25 into a halo orbit about the L1 Earth-Sun libration point. The satellite instruments and telemetry has provided almost 100% recovery of magnetic data and solar wind velocity data since the beginning of 1998. The satellite is still active.

In the present report we have analyzed ACE data from February 1998 through 2004. The main advantage of using ACE data for the present study is their regularity over the years which are getting close to span a full solar activity cycle. The main disadvantage of using ACE data in the present study is the large distance of around 240 Re ($\sim 1.500.000$ km) from the Earth to the satellite. This large distance causes a delay of typically around 1 hour for the solar wind with its embedded magnetic field to travel from the satellite position to the encounter with the Earth's magnetosphere.

2.4. Processing satellite data

In order to provide a uniform basis for satellite-ground correlation studies all IMP 8/Wind/ACE data have been referred to a fixed position at 12 Re in front of the Earth. This modification is accomplished by shifting the data in time with an amount corresponding to the solar wind travel time from the actual satellite position to the GSE X-coordinate of the reference position assuming uniform conditions in planes perpendicular to the Sun-Earth line (GSE X-axis).

In order to make sure that the relevant observations are made in the solar wind undisturbed by the presence of the Earth, i.e. outside the magnetosphere and upstream relative to the bow shock, we have limited the data selection by requiring the GSE X-coordinate to be positive (has effects for IMP 8 and Wind) and the geocentric distance to be greater than 20 Re (has effects only for Wind).

For IMP 8 the upper limit on the X-coordinate is around 40 Re. This leaves a span for the solar wind travel from the satellite to the reference location to deal with distances between -12 Re (at $X_{GSE} = 0$) and +30 Re, which with typical solar wind velocities of 350 km/sec corresponds to delays ranging between around -4 min and +10 min.

For Wind the relevant delay spans from around - 4 min at $X_{GSE} = 0$ (in Earth orbits) to around 60 min at $X_{GSE} = \sim 240$ Re (in halo orbits around L1).

For ACE the typical delay is around 60 min between solar wind observations at the satellite and the encounter of the same solar wind volume at the Earth's magnetosphere (12 Re reference position).

All the above-mentioned delays are just typical values. In actual cases the precise satellite position and the observed solar wind velocity are used to calculate the relevant delays.

The calculations are the following. First, from observations at the satellite of the solar wind velocity V_{SW} in the $-X_{GSE}$ direction and the X_{GSE} coordinate of the satellite position at (UT) time T_S the delay to the $X_{GSE} = 12$ Re plane is calculated:

$$\Delta T (T_S) = (X_{GSE} (T_S) - 12 \text{ Re}) / (-V_{X,SW}(T_S)) \quad (2.2)$$

This delay is referred to the time T_R at the 12 Re position by shifting the time scale appropriately:

$$\Delta T (T_R) = \Delta T (T_S - \Delta T (T_S)) \quad (2.3)$$

In order to avoid effects from simple fluctuations in the solar wind velocity observations we form "sorted" averages of the calculated delays over 10 min. The sorting is accomplished by taking the maximum and minimum values out of the summation required to form the average values. Thus the influence from irregular "spikes" is most often avoided. Subsequently, the precise value of the delay at any given time is estimated from interpolation between these 10-min averages.

The next step is the shifting of observed solar wind velocities and magnetic field intensities to apply at the reference position. We want a regular time series in T_R , for instance 1-min samples, of these data at 12 Re. Hence we derive the appropriate values by shifting back in time by the calculated delay to the relevant field ($IMF \mathbf{B}$) and velocity (V_{SW}) values at the satellite position (X_{GSE}).

$$V_{SW} (T_R, 12 \text{ Re}) = V_{SW} (T_R - \Delta T (T_R), X_{GSE} (T_R - \Delta T (T_R))) \quad (2.4a)$$

$$IMF \mathbf{B} (T_R, 12 \text{ Re}) = IMF \mathbf{B} (T_R - \Delta T (T_R), X_{GSE} (T_R - \Delta T (T_R))) \quad (2.4b)$$

If the solar wind velocity and the satellite position were constant we could simply shift the entire time series of field and solar wind by a constant delay. With the present procedure we do the smoothing on the solar wind velocity, which is assumed to be the parameter of least "natural" variability compared to the interplanetary magnetic field intensity. We end up with regular time series (equidistant samples) for the parameters at the reference (12 Re) position.

Basically, using the above outlined procedure, all the relevant solar wind field and velocity parameters have been converted into 1-min samples at the reference 12 Re position. For some of the statistics we proceed to calculate 5-min sorted averages (excluding max and min values). We are now in a position to compare the data collected by the three satellites in question.

2.5. IMP 8 - ACE comparison

The IMP 8 and ACE satellites have overlapping data from 1998 through 2000. Fig. 2.2. displays a direct comparison of GSM components of the interplanetary magnetic field and of the solar wind velocities observed from the two satellites. The IMP 8 data define the X-coordinates of the points.

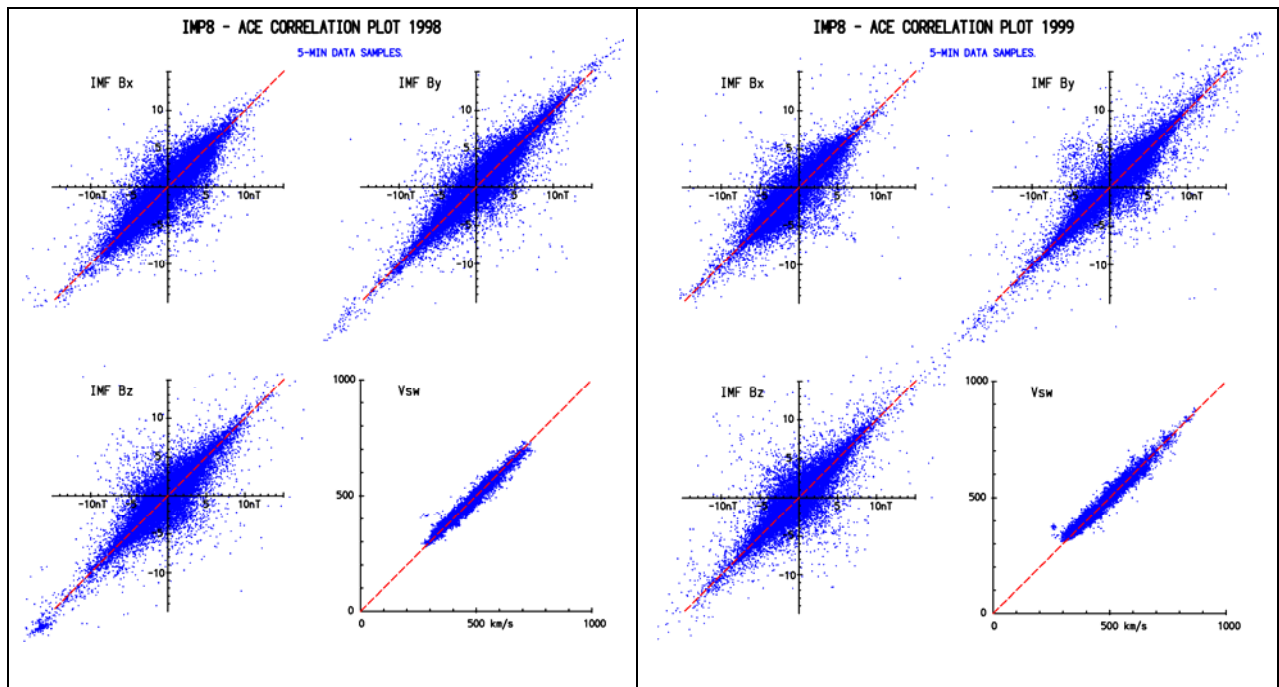


Figure 2.2. Comparison of GSM components of the IMF and of solar wind velocities from ACE and IMP 8 observations. ACE data from $X_{GSE} \sim 240$ Re and IMP 8 data from $R \sim 30$ Re all shifted to $X_{GSE} = 12$ Re.

The data displayed in Fig. 5 are 5-min samples of the observations from ACE at ~ 240 Re and from IMP 8 at ~ 30 Re from 1998 and 1999. All data have been referred to 12 Re by the procedure outlined above. The comparison of ACE and IMP 8 solar wind velocities displayed in the lower right field of each of the two sets shows quite good agreement. One may also note, that there are no cases of IMP 8 velocities much lower than ACE velocities; hence all selected IMP 8 data displays undisturbed IMF and solar wind conditions outside the Earth's bow shock which slows down the velocities to sub-Alfvénic level.

The magnetic data, on the contrary, show a good deal of scatter. It seems that the statistical averages of the ACE and IMP 8 data for the three IMF components are equal since the distributions appear to be symmetrical with respect to the diagonal drawn with the red dashed line.

Fig. 2.3. provides a closer look on the agreement between values of the merging electric field referenced to 12 Re as calculated from data from ACE and IMP 8, respectively.

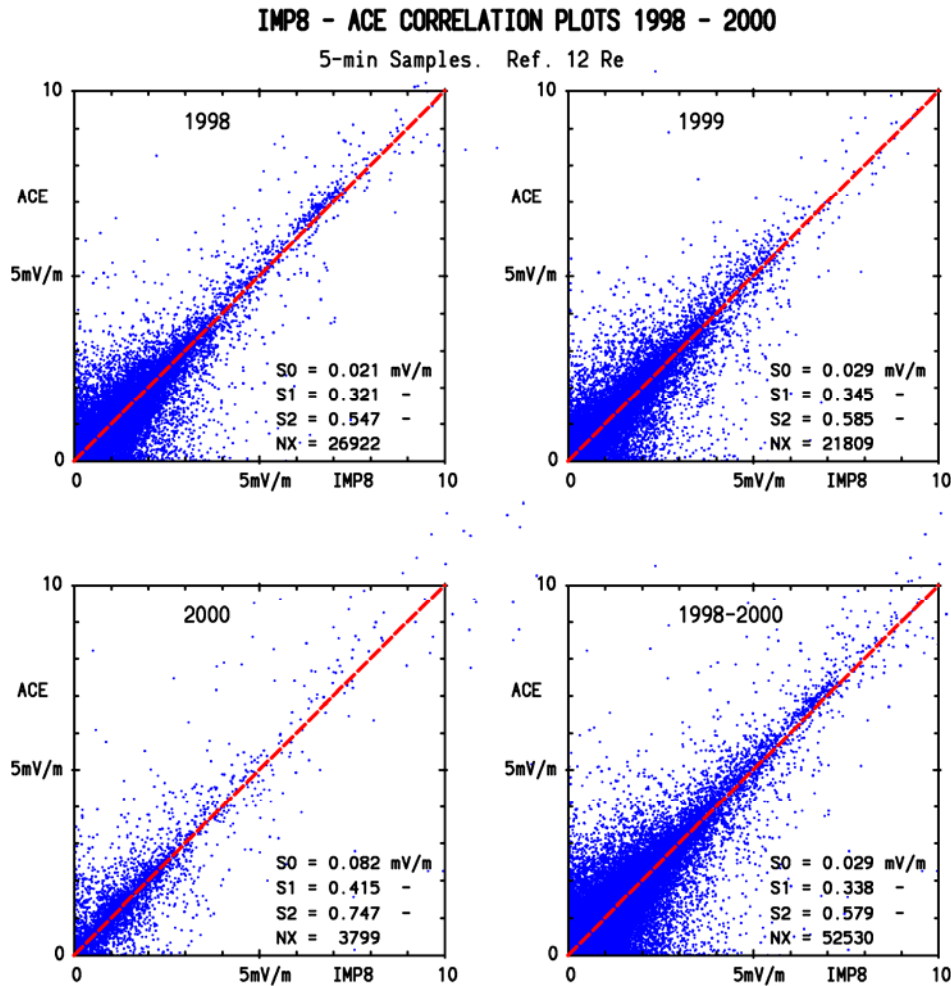


Figure 2.3. Correlation scatter plots for 1998 through 2000 of 5-min samples of the merging electric field ($V_{sw}B_T \sin^2(\theta/2)$) calculated from ACE and IMP 8 data, respectively. All data shifted to 12 Re.

The parameters S0, S1 and S2 are "quality figures" for the fit between the two sets of merging electric field (MEF) data.

S0 : Average signed difference between ACE and IMP 8 MEF values.

S1 : Average unsigned ("robust") difference between ACE and IMP 8 MEF values.

S2 : RMS difference of ACE values over IMP 8 MEF values.

NX : Number of 5-min MEF samples.

It is seen directly from the fields in Fig. 2.3. that the distributions appear to be symmetrical with respect to the diagonal (equal ACE and IMP 8 MEF values) drawn with the red dashed line. This is confirmed by the low values of the S0 parameter which shows that the average difference between ACE and IMP 8 is only 0.02-0.03 mV/m (ACE larger). The difference should be compared to the typical MEF values, which range from 0 to ~5 mV/m with an average value a little over 1 mV/m.

There is, however, a considerable scatter in the individual values observed from ACE and IMP 8. The RMS difference is around 0.5 to 0.6 mV/m, which is quite large compared to the above-mentioned typical MEF values of around 1 mV/m. The main cause of this difference, as shall be demonstrated below, is the high level of fluctuations in the solar wind parameters such that separations of only a few Earth radii between any two satellites result in quite large differences between observed values.

2.6. IMP 8 - Wind comparison.

The IMP 8 and Wind satellites have overlapping data from 1995 through 1999 (and a sparse amount in 2000). During this interval the IMP 8 satellite maintains its orbit at distances varying from around 25 to 40 Re from the Earth. The Wind satellite, however, is moved around between highly eccentric Earth orbits and halo

orbits around the L1 liberation point approximately 240 Re in front of the Earth along the Sun-Earth line (GSE/GSM X-axis). The comparison of data from the two satellites offers an opportunity to analyze the effects of varying the distance between them. Fig. 2.4a and Fig. 2.4b illustrates in correlation scatter plots the comparison of IMP 8 and Wind observations of the GSM components of the IMF and of the solar wind velocities. All data have been shifted to the reference location at 12 Re. The varying geocentric distance of the Wind satellite is illustrated with a color code using blue signature for data points where the Wind X_{GSM} distance from the Earth is less than 50 Re, green between 50 and 150 Re, and red for distances between 150 and 250 Re. In all selected cases the transverse distance of the Wind satellite from the Sun-Earth line is less than 50 Re.

An inspection of the color coding displayed in the diagrams in Figs. 2.4a and 2.4b indicates that in years 1996 and 1998 the Wind satellite was more often closer the Earth (blue points) than in 1999 (red points). In 1995 (left diagram in Fig. 2.4a) there is a more even mix of colors.

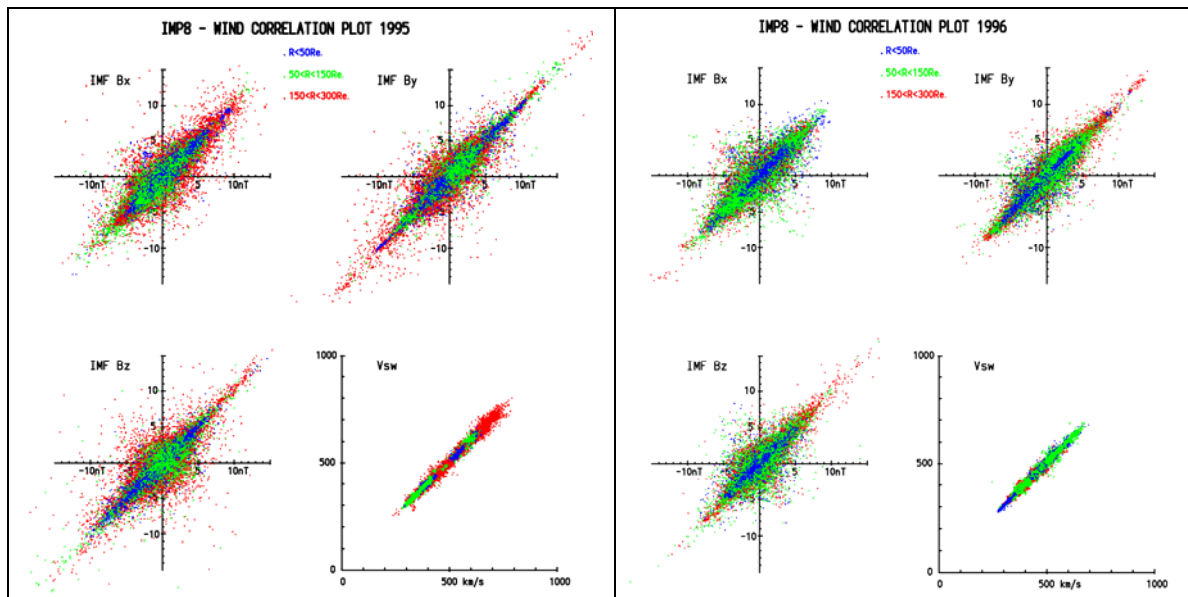


Figure 2.4a. Comparison of GSM components of the IMF and of solar wind velocities from IMP 8 and Wind observations. IMP 8 data from ~ 30 Re and Wind data from ~ 20 to ~ 250 Re all shifted to 12 Re.

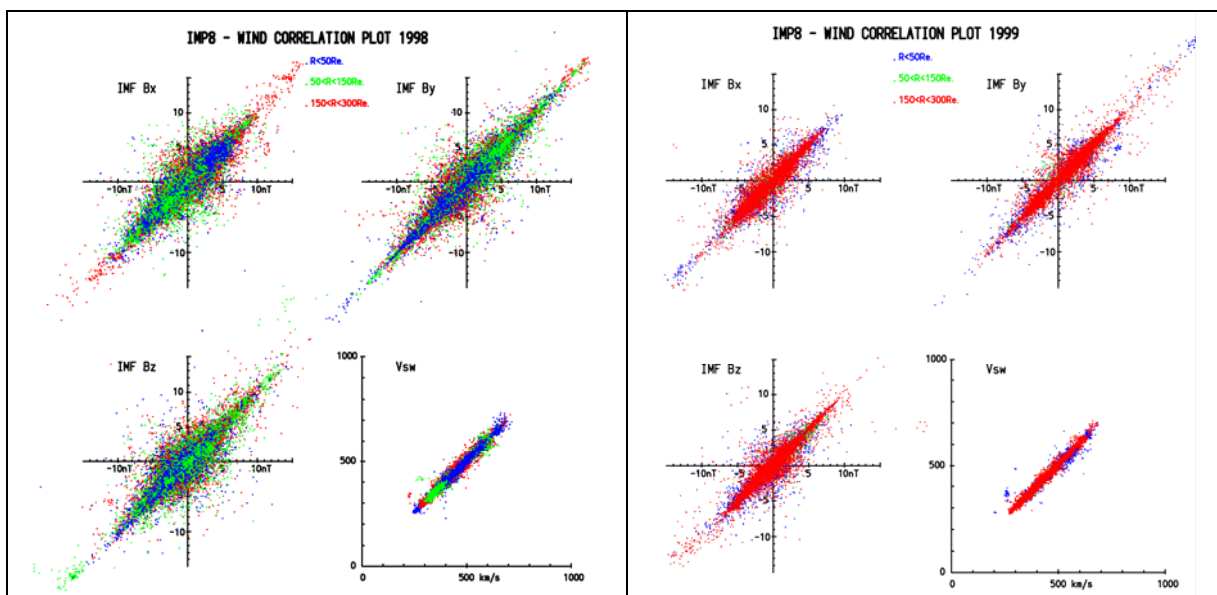


Figure 2.4b. Continuation of Fig. 2.4a. Comparison of GSM components of the IMF and of solar wind velocities from IMP 8 and Wind observations. IMP 8 data from geocentric distances of ~ 30 Re and Wind data from ~ 20 to ~ 250 Re are all shifted to 12 Re.

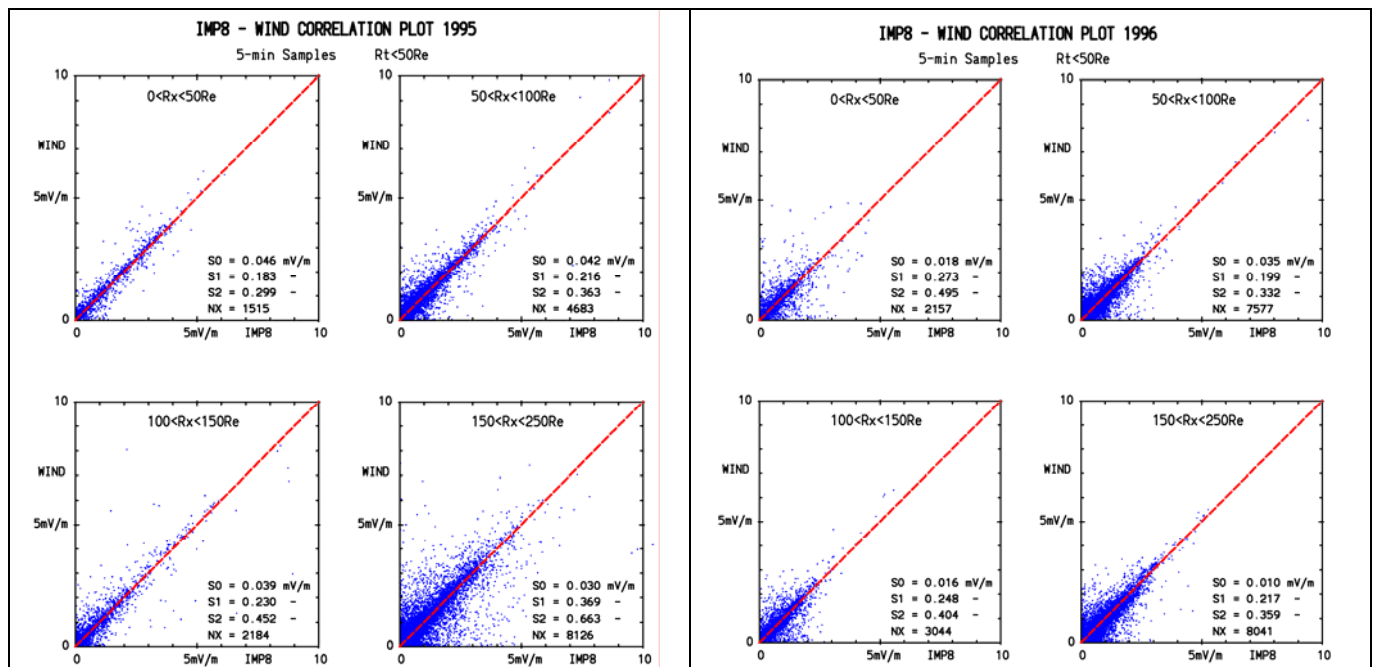
Throughout the years and through the different Wind distances the observed IMP 8 and Wind solar wind velocities agree quite well. Furthermore, the almost complete absence of outliers with much lower solar wind velocities observed from one satellite compared to those observed from the other satellite indicates that the data selection procedures has eliminated data from inside the Earth's bow shock.

For the magnetic data there is large scatter between the values observed at the two satellites. However, it is clear in all cases that the statistical averages of the field components are equal since the distributions appear to be quite symmetrical around the diagonal.

Another important observation emerges when comparing the diagrams from 1996 and 1998 with the diagram from 1999. It is clear that the scatter in the latter diagram (1999), where the Wind satellite is mostly in a halo orbit around the L1 liberation point (i.e. at ~ 240 Re) is not larger than the scatter seen in the former (1996/1998) diagrams where the Wind satellite is mostly positioned in Earth orbits at substantially smaller geocentric distances.

This observation substantiates the procedures used to calculate the delays and subsequently used to shift the observed data from the satellite position to the reference position at 12 Re. The IMP 8 satellite is always near the reference point so the delays, and hence the time shifts, are rather small (few minutes). For the Wind satellite, when near the L1 point, the delays, and hence the time shifts of the observations, from the satellite to the reference position, is on the order of 1 hour. For the 5-min samples displayed in Figs. 2.4a and 2.4b such a large difference in time shift would cause large scatter if the delay calculations were incorrect.

Like done above for the ACE-IMP 8 correlation analysis we have also compared the values of the merging electric field (MEF) as derived from using data from the IMP 8 and Wind satellites, respectively, shifted to the reference position (12 Re). In Fig. 2.5. the results are displayed in sets comprising 4 diagrams each. Within each set the 4 diagrams display data selections, where the Wind X_{GSE} coordinate is constrained to ranges between 0-50 Re, 50-100 Re, 100-150 Re and 150 - 250 Re, respectively. The transverse distance is limited to a maximum of 50 Re from the Sun-Earth line except for the summary plot in the bottom left field, where the transverse distance is limited to values less than 30 Re.



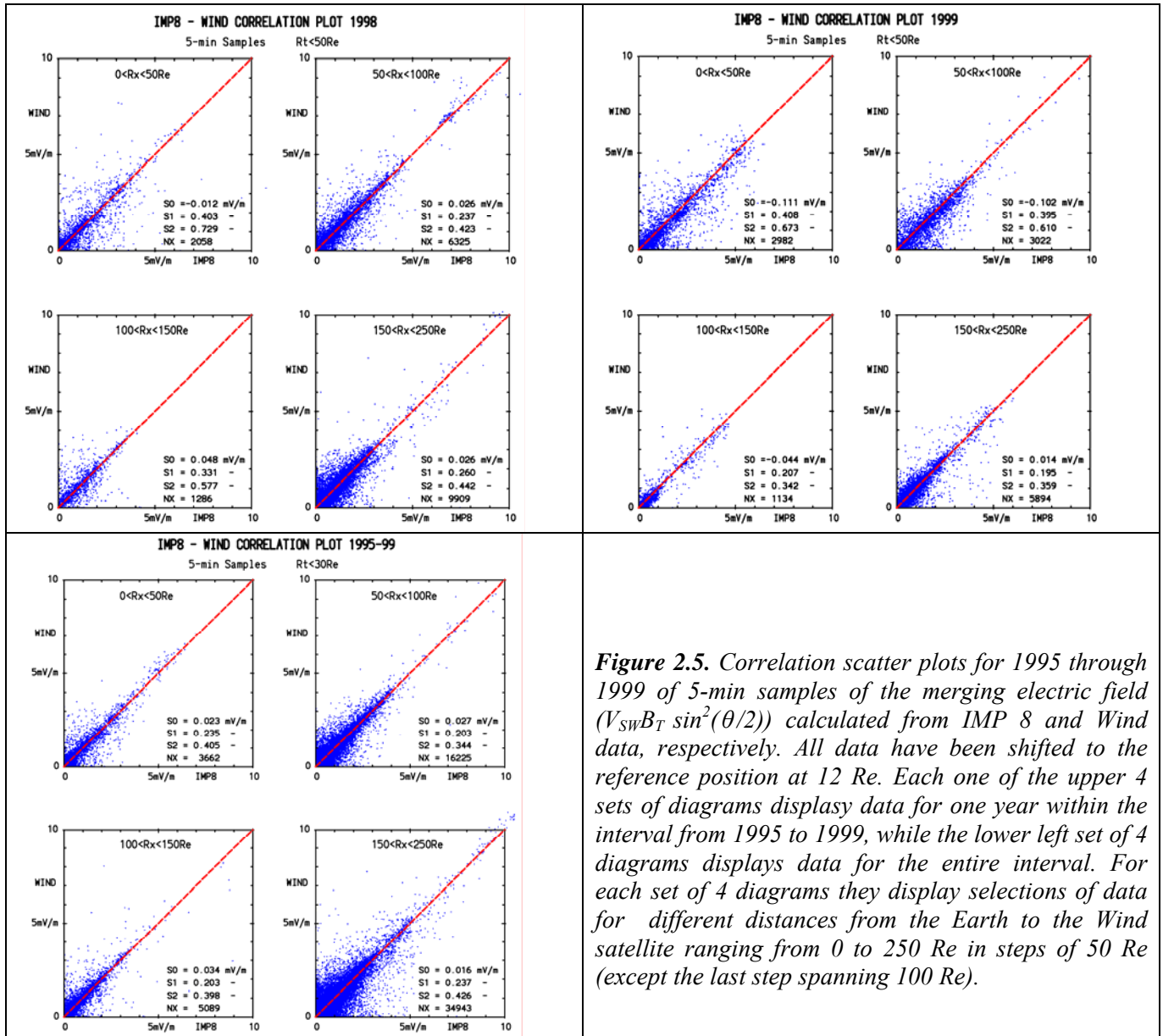


Figure 2.5. Correlation scatter plots for 1995 through 1999 of 5-min samples of the merging electric field ($V_{SW}B_T \sin^2(\theta/2)$) calculated from IMP 8 and Wind data, respectively. All data have been shifted to the reference position at 12 Re. Each one of the upper 4 sets of diagrams displays data for one year within the interval from 1995 to 1999, while the lower left set of 4 diagrams displays data for the entire interval. For each set of 4 diagrams they display selections of data for different distances from the Earth to the Wind satellite ranging from 0 to 250 Re in steps of 50 Re (except the last step spanning 100 Re).

The fit quality parameters depicted at the bottom left of in each of the summary set of diagrams in Fig. 2.5. are displayed in Table 1.

Table 2.1. Fit quality parameters for IMP8 - Wind MEF(12Re) correlation vs. Wind X_{GSE} distance from the Earth

Parameter	$0 < X_{GSE} < 50$	$50 < X_{GSE} < 100$	$100 < X_{GSE} < 150$	$150 < X_{GSE} < 250$	Unit
S_0	0.023	0.027	0.034	0.016	mV/m
S_1	0.235	0.203	0.203	0.237	mV/m
S_2	0.405	0.344	0.398	0.426	mV/m
N_x	3662	16225	5089	34943	samples

One may note from Table 2.1. that the statistical averages of the merging electric field (MEF) calculated from IMP 8 and Wind satellite data, respectively, are almost identical with average differences (S_0) of only around 0.02 mV/m contrasted to typical values on the order of 1 mV/m for the MEF levels.

One may further note that there is no great difference between the fit quality parameters calculated for the small distances ($0 < X_{GSE} < 50$ Re), where the Wind satellite is in the same near-Earth region as the IMP 8 satellite, and the much larger distances beyond 100 Re ($X_{GSE} > 100$ Re), where the Wind satellite is close to the L1 liberation point. This result indicates that the rather large scatter, as evident in either the average

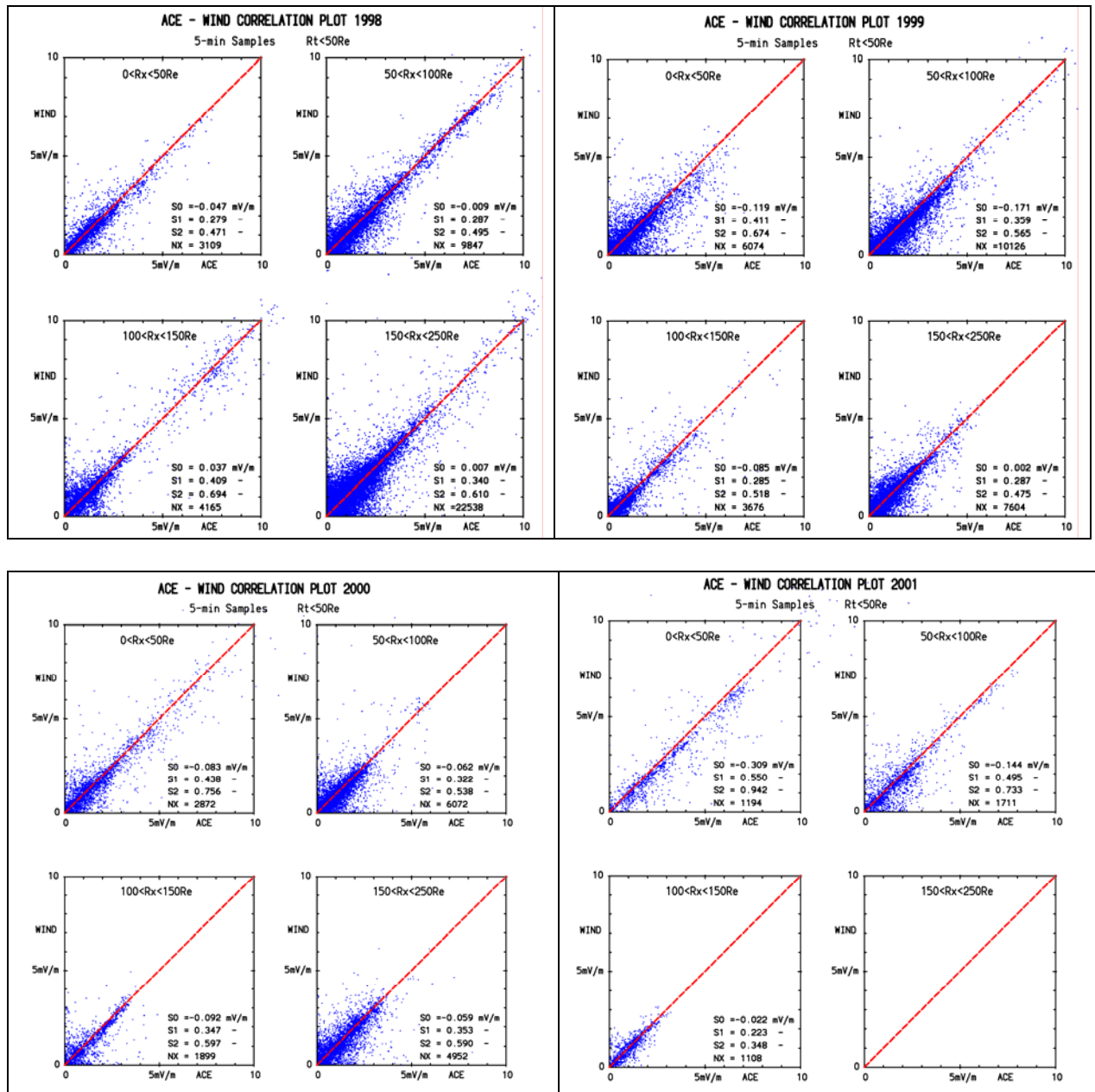
robust difference ($S1$) or in the RMS deviation ($S2$), is not caused just by uncertainty in the calculated time shift of the two data series.

The magnitudes of the fit quality parameters ($S0$, $S1$, $S2$) are less (i.e. better fit) for IMP 8 – Wind for all distances than the corresponding parameters in the correlation of IMP 8 and ACE and also – as shall be shown below – less (better) than the corresponding parameters for the Wind – ACE correlations.

2.7. Wind - ACE comparison

The Wind and ACE satellites have overlapping data since the start of the ACE mission in 1998 and up to present. Like explained above the ACE satellite has stayed permanently in halo orbits around the L1 liberation point at around 240 Re in front of the Earth while the Wind satellite has been moved around between highly eccentric Earth orbits and halo orbits around the L1 point.

Fig. 2.6. presents yearly comparisons of values of the merging electric field at 12 Re calculated from Wind and Ace data, respectively. The results are displayed in sets comprising 4 diagrams each. The 4 diagrams display data selections, where the Wind X_{GSE} coordinate is constrained to ranges between 0-50 Re, 50-100 Re, 100-150 Re and 150 - 250 Re, respectively. The transverse distance is limited to a maximum of 50 Re from the Sun-Earth line.



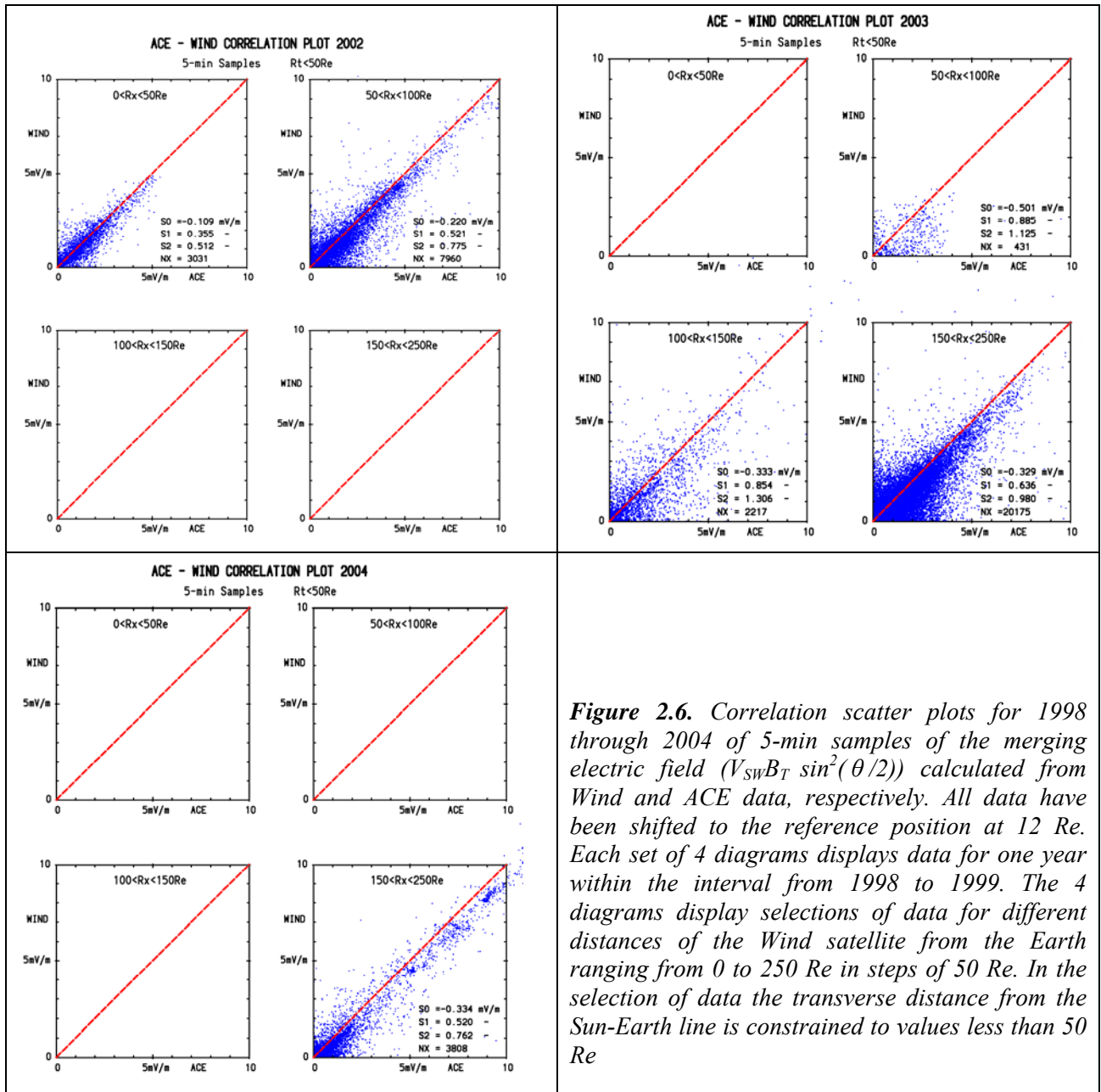


Figure 2.6. Correlation scatter plots for 1998 through 2004 of 5-min samples of the merging electric field ($V_{SW} B_T \sin^2(\theta/2)$) calculated from Wind and ACE data, respectively. All data have been shifted to the reference position at 12 Re. Each set of 4 diagrams displays data for one year within the interval from 1998 to 1999. The 4 diagrams display selections of data for different distances of the Wind satellite from the Earth ranging from 0 to 250 Re in steps of 50 Re. In the selection of data the transverse distance from the Sun-Earth line is constrained to values less than 50 Re

It is seen in these diagrams that there is no obvious difference between the level of scatter for cases where the Wind satellite orbits the Earth ($0 < X_{GSE} < 100$ Re) far away from ACE and cases ($150 < X_{GSE} < 250$ Re) where Wind is in the same region as ACE, that is, in halo orbits close to the L1 liberation point. It could be noted that the fit quality parameters (S0, S1, S2) are larger (worse fit) for the Wind-ACE correlation than calculated for the IMP 8 – Wind correlations (sec. 2.6.).

However, there is another worrying feature. It seems that a small shift in the levels of either Wind and Ace merging electric field is developing through the years since 2000. The ACE values of MEF are systematically getting lower than the MEF calculated from Wind data. Hence, in Fig. 2.6. too many of the points in the diagrams from year 2000 and following years are positioned below the diagonal. The development is illustrated in Table 2.2.

Table 2.2. Fit quality parameters for Wind - ACE merging electric field, MEF(12Re), correlation through years 1998 - 2004. Wind position is constrained to the range $150 < X_{GSE} < 250$ Re.

Parameter	1998	1999	2000	2003	2004	Unit
S0	0.007	0.002	-0.059	-0.329	-0.334	mV/m
S1	0.340	0.287	0.353	0.636	0.520	mV/m
S2	0.610	0.475	0.590	0.980	0.762	mV/m
Nx	22538	7604	4952	20175	3808	samples

Fig. 2.7. displays a direct comparison of the GSM components of the interplanetary magnetic field and of the solar wind velocities measured from the ACE and Wind satellites, respectively.

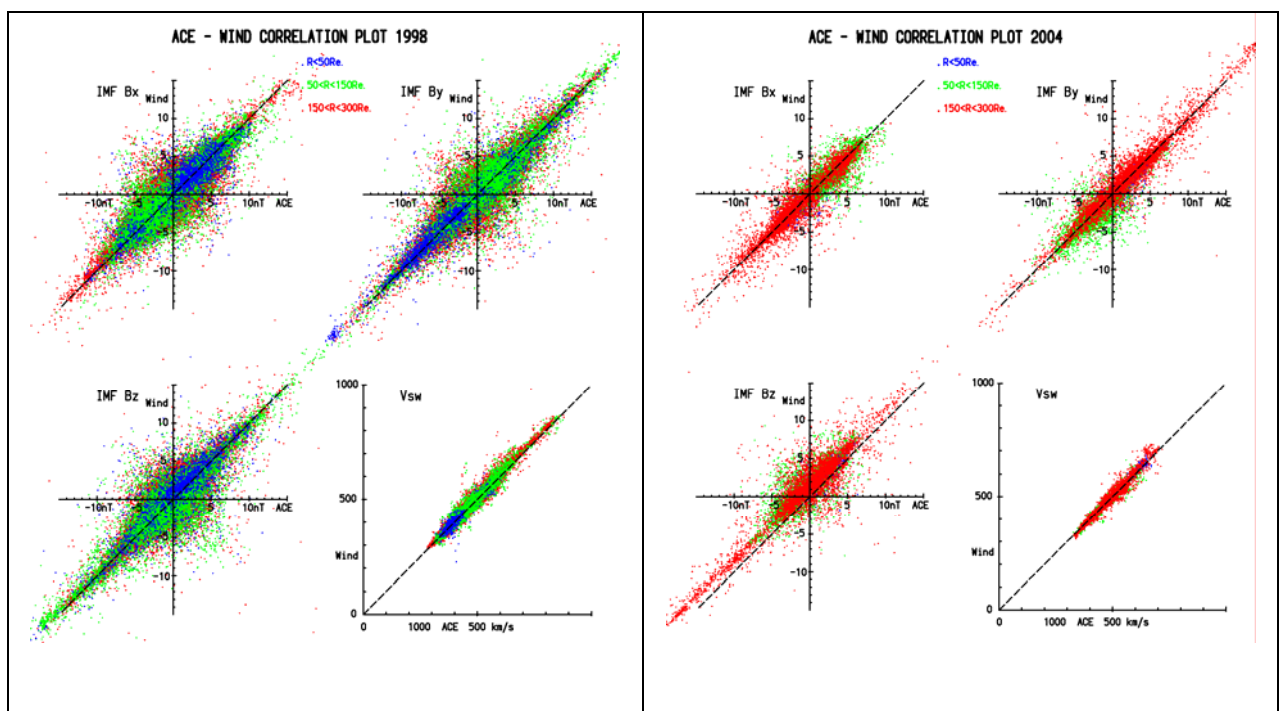


Figure 2.7. Comparison of GSM components of the IMF and of solar wind velocities from ACE and Wind observations. ACE data from ~ 240 Re and Wind data from ~ 20 to ~ 250 Re all shifted to 12 Re.

The two sets of data displayed in Fig. 2.7. are 5-min samples from years 1998 and 2004, respectively, of the observations from ACE at ~ 240 Re and from Wind moving in various orbits at geocentric distances varying between ~ 20 Re and ~ 250 Re. All data have been referred to 12 Re by the procedure outlined above. The comparison of ACE and Wind solar wind velocities displayed in the bottom right field of each of the two sets shows quite good agreement. The magnetic data, however, shows that the B_{zGSM} components have developed a difference. In 1998 the B_{zGSM} components, on the average, agree quite well whereas in 2004 the Wind B_{zGSM} values are systematically shifted 2-3 nT towards a more positive level compared to the ACE B_{zGSM} values. From calculations of long-term averages this discrepancy was found to be caused by drift in the Wind magnetometer data.

3. Processing of QL values for PC index calculations.

The geomagnetic variations with respect to the slowly (secularly) varying baselines depend on the actual combination of ionospheric electric fields and conductivities. The polar cap ionospheric electric fields relate mainly to the interplanetary merging electric field (MEF), but there are residual amounts which relate specifically to the solar wind velocities. The occurrences of auroral substorms may also affect the polar cap ionospheric electric fields. The ionization densities and thus the ionospheric conductivities mainly relate to the intensities of the solar UV and X-ray radiation in addition to general atmospheric properties. But the ionization densities are also affected by the precipitation of energetic particle radiation, which may occur during solar outbursts (e.g., proton events) and auroral substorms.

Since the PC index, by definition, shall relate to the merging electric field then we wish to remove from the polar geomagnetic data, which form the basis for the PC index, other types of variations such as:

1. Regular daily and seasonal variations at steady solar UV and X-ray fluxes.
2. Changes with varying solar UV and X-ray fluxes.
3. Variations other than those related to the MEF with changes in solar wind velocities.

The procedure to derive the varying “quiet level” (QL) for polar magnetic recordings for any specific epoch shall extract the field values from recordings made during quiet intervals at times where the conditions match as closely as possible the conditions at the actual epoch. That is, same local time and same season. But also same solar wind velocity, and same solar activity level. The solar and solar wind parameters have sporadic variations related to sudden solar activity changes, which are not reproduced at different times. But they have also more steady variations related to the solar rotation which causes different faces of the Sun to illuminate the Earth and different sectors of the solar wind to interact with the magnetosphere through the average 27.4 day solar rotation period. These variations are to some extent reproduced cyclically.

The present procedure follows the outline provided in *Troshichev et al.*, 2006. At the high latitudes in question the usual concept of defining a reference level based on quiet days selected on basis of the daily sum of Kp index values is not so useful. In the polar regions the geomagnetic field could have quite strong variations while the conditions at middle and low latitudes remained rather undisturbed giving low Kp values. Moreover, it could be difficult to find entire UT days with undisturbed conditions since the usually unsteady interplanetary magnetic field (IMF) affects in a most direct manner the magnetic field intensities observed at ground level within the polar caps.

However, even during highly disturbed periods there might be shorter intervals, for instance a few hours at a time, where quiet geomagnetic conditions prevail. If such periods are selected properly then the recorded geomagnetic field intensities from such intervals can be combined to form a useful reference magnetic level where the variations are imposed solely by the combined effects of the uneven solar illumination and the solar wind velocity-dependent convection. Deviations from this reference level are considered to arise from the combined effect of the IMF and solar wind velocity as expressed in the Merging Electric Field Em (MEF):

$$Em = MEF = V_{SW} B_T \sin^2(\theta/2) \quad (3.1)$$

where V_{SW} is the solar wind velocity, B_T is the transverse component of the IMF ($B_T = \sqrt{B_Y^2 + B_Z^2}$), while θ is the polar angle between the GSM Z-axis and the transverse IMF component B_T .

In order to accomplish proper QL calculation we have developed the following procedure:

1. All calculations are made in a local geographic coordinate system with X-component in geographic north direction, Y-component in geographic east and Z-component downward in the northern hemisphere. If the field components are provided in another format (e.g. H, D and Z) they are first transformed to the (X,Y,Z) system. The basic data are 1-min samples either in .WDC (World Data Center) or in .BIN (Intermagnet) format, which is now the standard format.
2. The basic geomagnetic field intensities are subtracted. For Thule the basic geomagnetic field components are estimated every year referring to 1 January (northern winter). This set forms the table spanning the years 1973 to 2007 shown as Table 3.1. below. The entries beyond 2005 are extrapolated values.

Table 3.1. Reference basic geomagnetic field intensities for Thule 1973-2007.

Year	Declination	Inclination	H-comp	X-comp	Y-comp	Z-comp	F-total
1973.0	282.250	86.018	3936	835	-3846	56543	56680
1974.0	282.550	86.024	3934	855	-3840	56596	56733
1975.0	282.917	86.030	3931	879	-3832	56638	56774
1976.0	283.333	86.034	3929	906	-3823	56664	56800
1977.0	283.800	86.036	3928	937	-3815	56681	56817
1978.0	284.333	86.038	3926	972	-3804	56690	56826
1979.0	284.833	86.037	3927	1005	-3796	56691	56827
1980.0	285.267	86.033	3930	1035	-3791	56676	56812
1981.0	285.667	86.032	3930	1061	-3784	56655	56791
1982.0	286.033	86.034	3927	1085	-3774	56640	56776
1983.0	286.350	86.035	3925	1105	-3766	56622	56758
1984.0	286.667	86.038	3919	1124	-3754	56582	56718
1985.0	286.983	86.046	3909	1142	-3739	56555	56690
1986.0	287.300	86.054	3899	1159	-3723	56520	56654
1987.0	287.700	86.062	3888	1182	-3704	56486	56620
1988.0	288.067	86.071	3878	1203	-3687	56465	56598
1989.0	288.450	86.073	3875	1226	-3676	56447	56580
1990.0	289.050	86.084	3863	1261	-3651	56430	56562
1991.0	289.417	86.089	3856	1282	-3637	56400	56532
1992.0	289.917	86.090	3855	1313	-3624	56395	56527
1993.0	290.467	86.089	3853	1347	-3610	56362	56494
1994.0	291.083	86.093	3848	1384	-3590	56350	56481
1995.0	291.850	86.090	3850	1433	-3573	56335	56466
1996.0	292.567	86.097	3842	1474	-3548	56315	56446
1997.0	293.433	86.090	3848	1530	-3531	56304	56435
1998.0	294.333	86.088	3850	1586	-3508	56300	56431
1999.0	295.333	86.077	3862	1652	-3491	56310	56442
2000.0	296.333	86.060	3878	1720	-3476	56310	56443
2001.0	297.333	86.048	3890	1786	-3456	56310	56444
2002.0	298.417	86.035	3903	1857	-3433	56315	56450
2003.0	299.483	86.016	3922	1930	-3414	56320	56456
2004.0	300.483	86.001	3938	1998	-3394	56336	56473
2005.0	301.467	85.986	3953	2063	-3372	56333	56472
2006.0	302.500	85.990	3950	2122	-3331	56350	56488
2007.0	303.500	85.990	3950	2180	-3294	56350	56488

Now, for every day of the year the actual basic values are derived by interpolation between the values defined at 1 January in the present year and those from 1 January in the next year.

3. With these reduced intensities the actual magnetic field components are examined to define intervals of particularly small variability. For each UT hour the mean values (X_M, Y_M, Z_M) of the field components (X, Y, Z) are first calculated and the differences between the recorded values and the hourly mean values are derived:

$$x = X - X_M \quad y = Y - Y_M \quad z = Z - Z_M \quad (1\text{-min samples}) \quad (3.2)$$

Two variance parameters are calculated. One is the maximum time derivative of the 1-min samples of horizontal field vector \mathbf{H} through the hour, i.e.:

$$dHt = \max \{ \sqrt{((x(t) - x(t-1))^2 + (y(t) - y(t-1))^2)} \} \quad (1\text{-hour samples}) \quad (3.3)$$

The other parameter is the average variance in \mathbf{H} through the hour, i.e.:

$$dHv = \text{avr} \{ \sqrt{x(t)^2 + y(t)^2} \} \quad (1\text{-hour samples}) \quad (3.4)$$

These parameters are listed in a file along with the hourly means of the field components. An example of these values for the first day of the year 2004 is shown in Table 3.2.

Table 3.2. Example hourly averages of Thule magnetic field components and variances.

Year	Md	Dg	Hr	X _M	Y _M	Z _M	dHt	dHv
2004	1	1	0	1	-14	15	6.4	11.5
2004	1	1	1	6	-51	5	9.5	19.6
2004	1	1	2	33	-60	28	10.8	16.3
2004	1	1	3	44	-32	42	7.1	8.0
2004	1	1	4	46	-17	34	6.4	15.3
2004	1	1	5	73	23	30	9.8	21.8
2004	1	1	6	83	39	32	7.6	16.1
2004	1	1	7	62	39	35	5.8	10.9
2004	1	1	8	47	61	33	7.2	22.6
2004	1	1	9	11	92	25	8.1	7.5
2004	1	1	10	16	80	7	11.0	22.9
2004	1	1	11	-11	51	2	12.4	25.5
2004	1	1	12	-34	101	8	11.0	32.5
2004	1	1	13	-90	97	13	10.0	46.3
2004	1	1	14	-42	48	2	17.0	40.9
2004	1	1	15	-9	-8	-1	5.1	9.5
2004	1	1	16	-42	14	1	15.1	30.2
2004	1	1	17	-78	21	1	11.7	22.4
2004	1	1	18	-94	-6	-2	9.1	15.0
2004	1	1	19	-84	-20	-3	12.0	22.8
2004	1	1	20	-51	-26	-10	11.4	22.7
2004	1	1	21	-100	-50	26	15.3	13.8
2004	1	1	22	-64	-26	35	9.2	37.1
2004	1	1	23	-5	-12	7	6.1	10.2

Since the total variation over a quiet day is typically sinusoidal-like with an amplitude on the order of 50 - 100 nT then the "quiet" maximum time derivative, dHt , would be less than 1 nT (in 1 min) and the "quiet" hourly variance, dHv , would be less than 10 nT. Actual values beyond these are indicative of magnetic disturbances.

4. From hourly values like those shown in Table 3.2 we compose the quiet day level by making a weighted average of data for each UT hour through an appropriate interval. The weight function is related to the "normalized" variances as shown below:

$$WF = \exp\{- (dHt/DTL)^{WP} - (dHv/DVL)^{WP}\} \quad (3.5)$$

where the normalized variances are raised to the power WP. The power is typically WP=2 and the normalization constants are typically $DTL=10$ nT and $DVL=20$ nT while WP is typically 4.

5. In order to enhance the systematic variations and suppress excursions related to singular events the QL values are smoothed both with respect to UT hour of the day and with respect to day of the year. The smoothing is done by averaging a series of consecutive hours around the selected UT hour and a series of days around the selected day using a Gaussian weight function:

$$WG = \exp\{ - (H - H0)^2/XHR^2 - (D-D0)^2/XDD^2 \} \quad (3.6)$$

where H is the variable UT hour, $H0$ is the selected UT hour and XHR is the width of the Gaussian weight function for the time-of-day. Correspondingly, D is the variable day number, $D0$ is the selected day and XDD is the width of the Gaussian weight function for day of the year. The summations involved in the averaging are extended to around twice the width. Provisions are made for summation beyond the 24 hours a day by imposing cyclic extensions. Around New Year data from the preceding or the following year are included as needed. Typical values are $XHR=4$ hours and $XDD=30$ days.

6. For the smoothing over days it should be noted that the QDC level depends on solar UV as well as solar wind intensities. Both parameters vary due to time-varying processes at the Sun as well solar rotation. The solar rotation causes different active regions at the Sun to face the Earth and also causes the sector structure in the solar wind to sweep cyclically past the Earth. Highest weight should be given to intervals where the Earth is illuminated by the same face of the Sun and also is located in the same solar wind sector as on the selected day. Thus, we finally impose a squared cosine function using the double solar rotation angle as argument. This function has a broad maximum at times where the same face of the Sun is directed towards the Earth and a broad minimum when the opposite face is turned towards the Earth half a solar rotation period ($SRP \sim 27.4$ days) later.

$$WH = \cos^2(\pi*(D - D0)/SRP) \quad (3.7)$$

8. The final weight function is simply the product of the three functions defined by Eqs. 3.5, 3.6, and 3.7. The weighted averaging is conducted over an interval of +/- 40 days with respect to the actual day. This interval comprises with maximum weight the central interval of a quarter of the solar cycle to either side of the present day and with lesser weight the corresponding intervals centred one solar cycle before and after the actual day. Minimum weight is given to the intervals half a solar cycle to either side of the day in question where the opposite side of the Sun is facing the Earth. The calculations are automated and provide reliable QL values for the years in question in just a single computer run.

The QL values are calculated and stored as sets of hourly values through each day of the year. A segment of such hourly QL data referring to the 1st of January and July 2000, respectively, is displayed in Table 3.3. The baseline values of the X and Y components are shown as the values listed at hour 24 for each day such that the absolute QL values can also be derived from the table by adding for each hour the baseline value to the relative QL value listed for each of the two components. One may note the daily variations in QLX and QLY displayed within each section and the seasonal variations seen in the differences in amplitudes between the two sections.

Table 3.3. QL hourly reference values for Thule for 1 January and 1 July 2000.

THULE QLWTTY DATA. YEAR = 2000 DTL=10 DVL=20 WP=2 XH0=6						THULE QLWTTY DATA. YEAR = 2000 DTL=10 DVL=20 WP=2 XH0=6					
YEAR	MD	DG	HR	QLX	QLY	YEAR	MD	DG	HR	QLX	QLY
2000	1	1	0	-10	-11	2000	7	1	0	-9	-26
2000	1	1	1	-6	-10	2000	7	1	1	1	-29
2000	1	1	2	-2	-9	2000	7	1	2	12	-28
2000	1	1	3	1	-6	2000	7	1	3	23	-25
2000	1	1	4	4	-3	2000	7	1	4	32	-19
2000	1	1	5	6	0	2000	7	1	5	40	-11
2000	1	1	6	6	4	2000	7	1	6	46	-1
2000	1	1	7	6	8	2000	7	1	7	50	10
2000	1	1	8	4	12	2000	7	1	8	51	21
2000	1	1	9	2	15	2000	7	1	9	49	32
2000	1	1	10	-1	17	2000	7	1	10	45	43
2000	1	1	11	-5	18	2000	7	1	11	37	52
2000	1	1	12	-9	19	2000	7	1	12	28	59
2000	1	1	13	-13	18	2000	7	1	13	16	63
2000	1	1	14	-17	16	2000	7	1	14	4	63
2000	1	1	15	-21	14	2000	7	1	15	-9	60
2000	1	1	16	-23	10	2000	7	1	16	-20	54
2000	1	1	17	-25	7	2000	7	1	17	-29	45
2000	1	1	18	-25	3	2000	7	1	18	-35	34
2000	1	1	19	-25	-1	2000	7	1	19	-38	21
2000	1	1	20	-23	-4	2000	7	1	20	-37	9
2000	1	1	21	-21	-7	2000	7	1	21	-34	-3
2000	1	1	22	-17	-10	2000	7	1	22	-27	-13
2000	1	1	23	-14	-11	2000	7	1	23	-19	-21
2000	1	1	24	1720	-3476	2000	7	1	24	1753	-3466

The relations between the recorded data and the calculated QL values are displayed in diagrams, which present the original raw Thule data (corrected for the basic level varying with the secular changes) and the QL levels derived from the above outlined calculations. Examples of such diagrams are shown in Figs. 3.1. and 3.2.

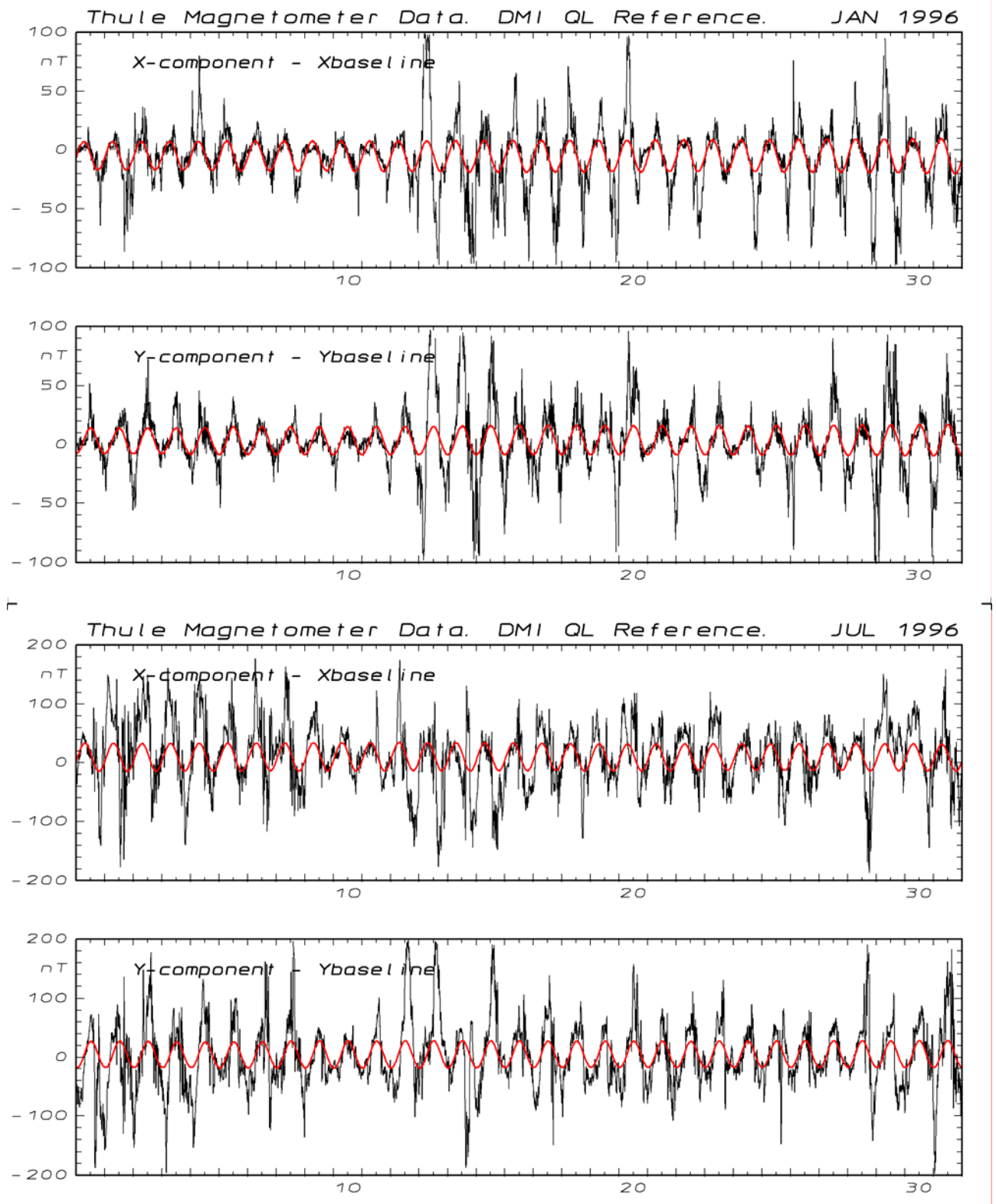


Figure 3.1. Thule raw magnetometer data corrected for the secularly varying level (black line) and the QL values (red line) calculated from the minimum variance method. Data for January (minimum QL variation) and July (maximum QL variation) are presented. Note the different amplitude scales for January and July. This year, 1996, is a solar minimum year.

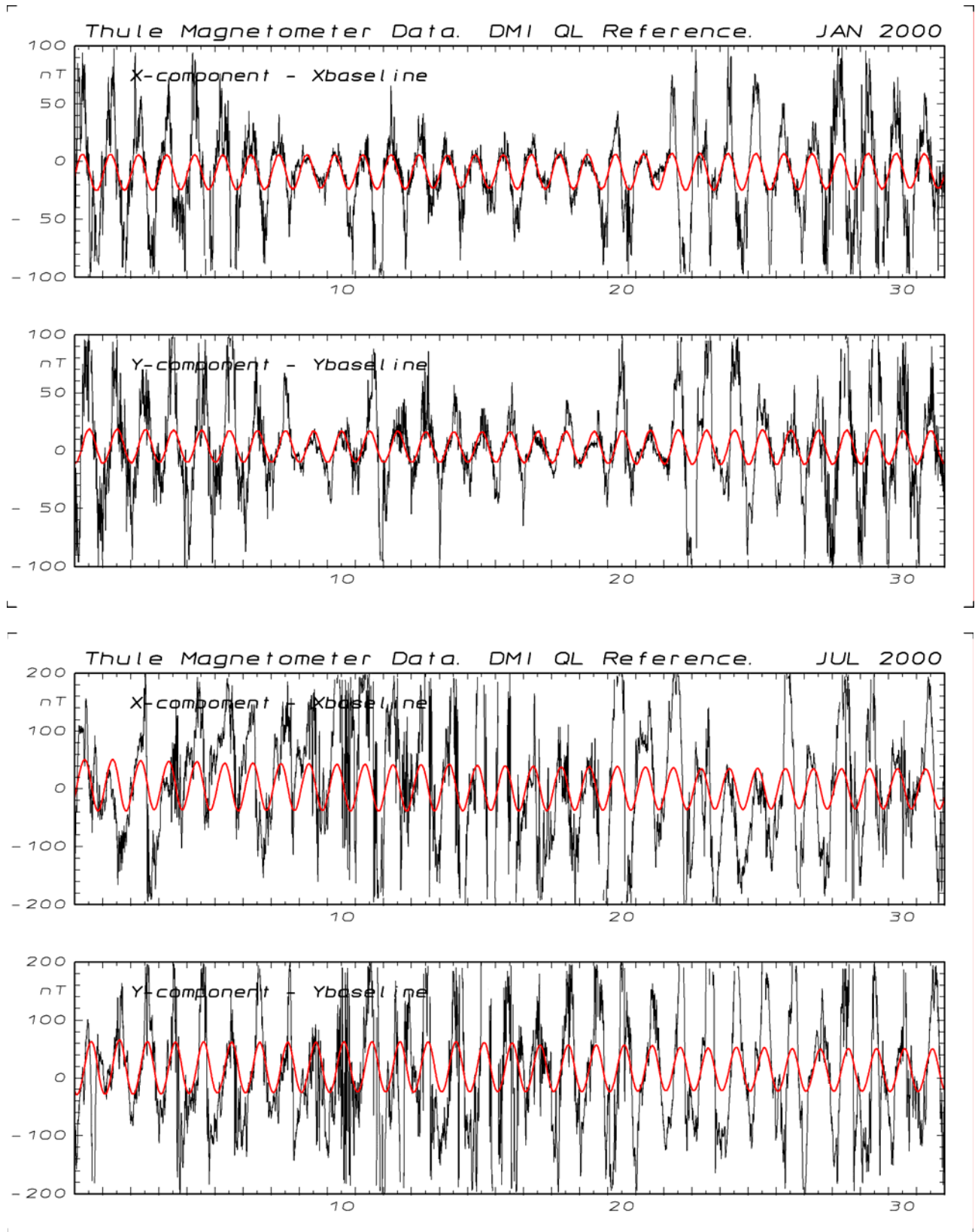


Figure 3.2. Thule raw magnetometer data corrected for the secularly varying level (black line) and the QL values (red line) calculated from the minimum variance method. Data for January (minimum QL variation) and July (maximum QL variation) are presented. Note again the different scales for January and July. This year, 2000, is a solar maximum year.

The systematic variations in the QL values related to time-of-day, season, and phase in the solar cycle are displayed in Figs. 3.3. and 3.4. Figure 3.3. displays examples of the results obtained from using the above outlined procedure for selected years from 1975 through 1987, i.e., an 11-year solar activity cycle. Fig. 3.4. displays another example of a series of QL values for the Thule magnetic X- and Y-components for years 1993-2005, i.e., the most recent solar cycle. The diagrams in Figure 3.3. and 3.4. present along the vertical axes a scale for QL values spanning from -80 nT to + 120 nT referring to the deviation from the basic levels derived by interpolation of yearly reference values (cf. Table 3.1). The diagram is divided along the horizontal axis in 12 monthly fields (JAN, FEB, etc.). Within each field there is a scale from 00 to 24 hours UT. Each monthly field represents QL values provided as UT hourly values through one day at the middle of each month (the 15th). In order to display a clear view of the principal features the QL values are further smoothed over corresponding intervals through 3 years.

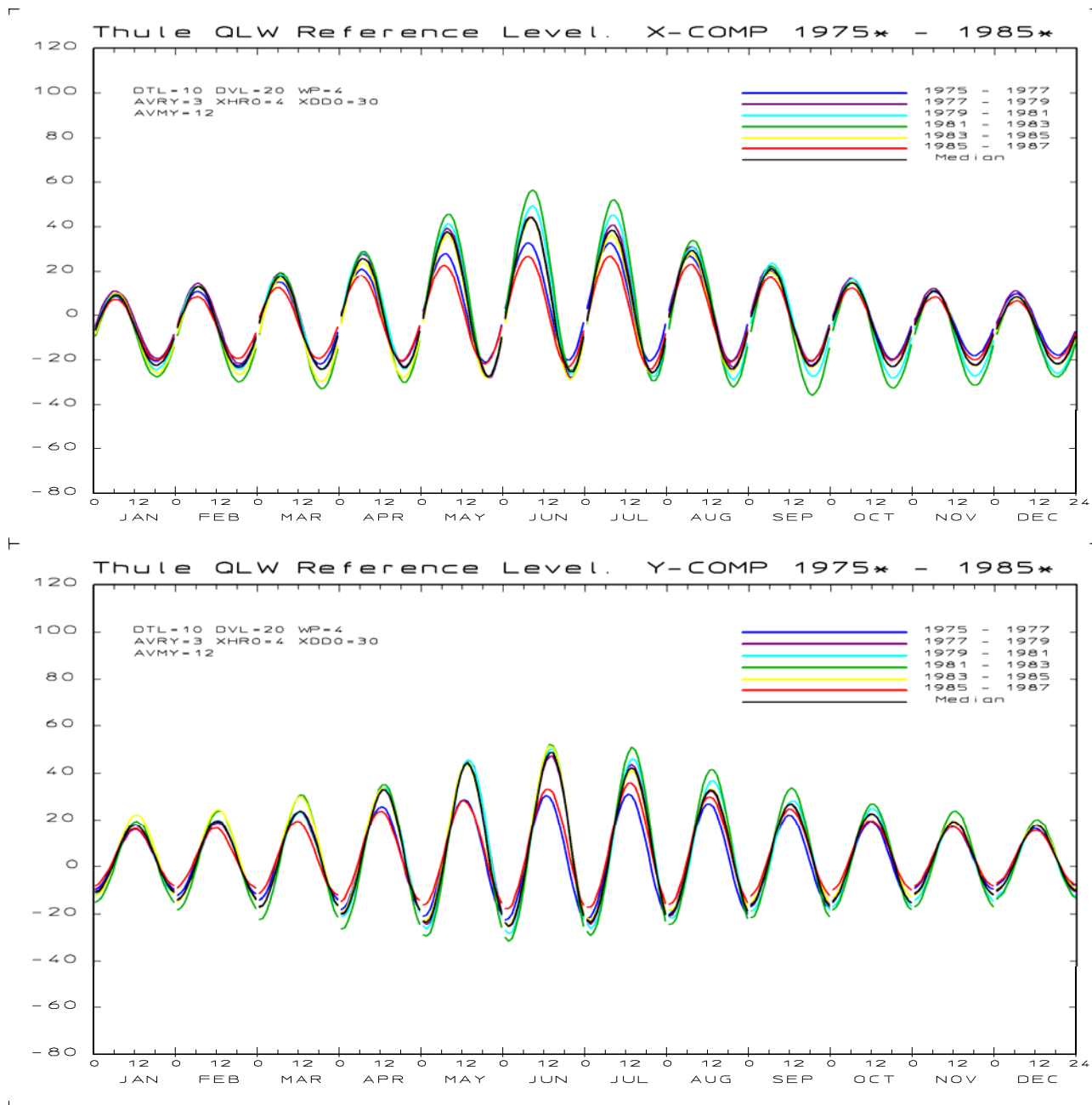


Figure 3.3. Display of QL values derived for the Thule X (northward) and Y (eastward) magnetic components for selected years through the time interval from 1975 through 1987. The median values are shown for illustration only.

In the diagram at the top of Fig. 3.3 the X-component data from 12 years ($AVMY=12$) are presented. The corresponding data set for the Y-component is shown in the diagram at the bottom of Fig. 3.3. Each differently coloured set of curves represent QL averages through 3 years ($AVRY=3$). In the selection of undisturbed intervals the variance normalization parameters are $DTL=10$ nT and $DVL=20$ nT and the power used in the variance weight function is $WP=2$. For the 2-D smoothing the Gaussian widths in the weight factors used in the appropriate summation are $XHR=4$ hours and $XDD0=30$ days, respectively. For the solar rotations a period of 27.4 days has been used. The daily and seasonal variations are seen distinctly in the diagrams. Furthermore, it is clear from both diagrams that the QL levels display systematic variations with the solar cycle. The amplitudes of the daily and seasonal variations are larger during solar maximum periods (e.g. around 1979-1982) than during years of minimum solar activity (e.g. around 1975-1977 and again 1985-1987).

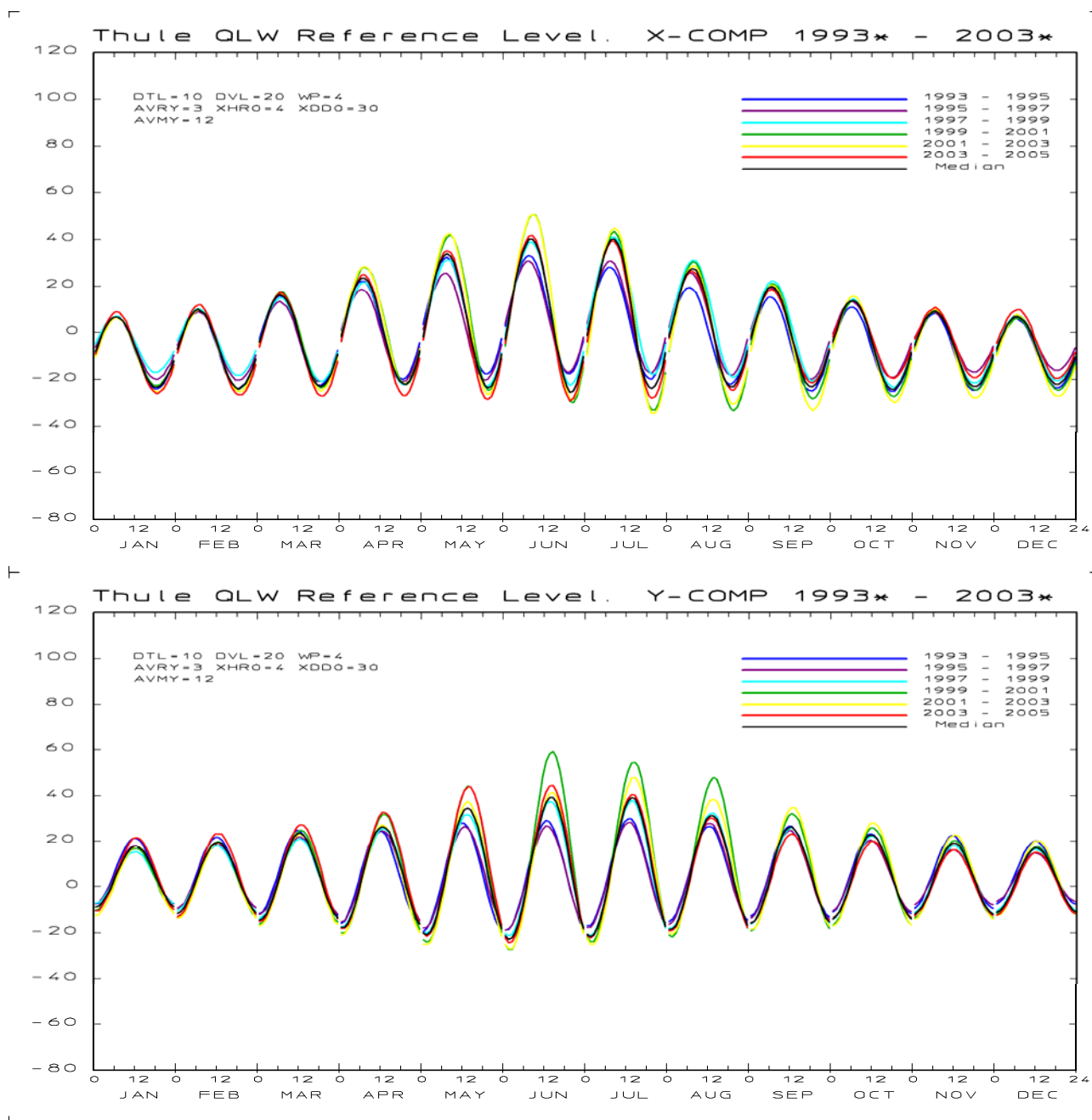


Figure 3.4. Display of QL values derived for the Thule X (northward) and Y (eastward) magnetic components for selected years through the time interval from 1993 through 2005. The median values are shown for illustration only.

Figure 3.4. displays the same systematic variations with time-of-day and season as those seen in Fig. 3.3. Furthermore, the variations with solar activity, which were evident in Fig. 3.3, are very similar to those seen in Fig. 3.4. In Fig. 3.4. the solar maximum extends from around 1999 to 2003. During these years the amplitudes in the daily and seasonal variations are particularly large. Solar minimum years are 1993 to 1997 and again around 2005. During these years the amplitudes in the QL variations are relatively small.

The curves drawn in black colour in the diagrams of Figs. 3.3. and 3.4. represent median values of the 6 QL data sets presented in different colours in the diagram. The median QL curves defined this way span 12 years - a full solar cycle - and change very little for different epochs. The median QL data are used for check of consistency but they are not used for further purposes.

The goal has been to derive QL levels with systematic and reproducible variations through time-of-day, season, solar rotation phase, solar wind sector structure, and solar activity cycle, and to minimize variations caused by random fluctuations or by singular events like strong geomagnetic storms or substorms. The various parameters used in the selection and smoothing processes have been found by "trial and error". It was the experience from processing these data that less emphasis on selecting undisturbed intervals (less weight to small variances) or less smoothing (less Gaussian width in UT time-of-day or month-of-year) would produce singular variations that could be spotted in one specific data set only and, therefore, would not be representative for the regular steady quiet variations.

These QL data sets derived for every day of the past years during the interval from 1975 to 2005, and their future continuation, shall be used to provide the reference QL values for calculations of the final PC-North index. Since the standard processing needs a span of 3 months (~3 solar rotation periods) with the day in question positioned at the middle of the interval, a slightly modified procedure shall be used to derive QL values for real-time PC index calculations. With this procedure we derive for each day a QL data set from hours of minimum variance selected through the preceding 30 days. Outlier data are removed and from the remaining QL data a reference QL is formed as the running average over the preceding 30 daily QL data sets. The on-line QL values are validated with respect to past QL calculations from data sets derived during solar activity conditions (e.g., F10.7 cm flux) like the actual conditions.

4. Optimum angle calculations

4.1. Definition of optimum direction angle.

Searching for a proxy based on polar magnetic disturbances to represent the solar wind "Merging Electric Field" ($Em = MEF = V_{SW} B_T \sin^2(\theta/2)$), we may increase the correlation between the horizontal disturbance vector ΔF (corrected for the quiet daily variations) and the MEF by projecting ΔF to a specific direction ("optimum direction"). This direction is not entirely fixed in space but varies slowly with local time and season. The horizontal magnetic vector is resolved in a (rotating) X-component (northward in a geographical coordinate system) and a Y-component (eastward). The vertical Z-component is downward in the northern polar cap. For the horizontal components we first subtract from the raw data the base values and then subtract QL values, i.e.:

$$\Delta X = (X_{RAW} - X_0) - X_{QL} \quad (4.1a)$$

$$\Delta Y = (Y_{RAW} - Y_0) - Y_{QL} \quad (4.1b)$$

here, X_0 is the base value for the X-component defined yearly (every 1 January) and now adjusted to the actual day-of-year. X_{QL} is the reference QL level provided as a table of hourly values for each day of the year and now adjusted to the proper day and time-of-day. The Y-component is handled correspondingly.

The projection of the disturbance vector ΔF to the optimum direction is given through:

$$\Delta F_{PROJ} = \Delta X \cdot \cos(U_{PROJ}) + \Delta Y \cdot \sin(U_{PROJ}) \quad (4.2)$$

where U_{PROJ} is the angle between the X-component axis and the optimum direction. This angle varies with local time, $LThr$ (LT time in hours), according to:

$$U_{PROJ} = U_0 + LThr \cdot 15^\circ \quad (4.3)$$

In order to explain the projection angles the diagram in Fig. 4.1 displays the northern polar region in geographical latitude (latitude circles every 5° from 75° to the pole) and local time (LT). For Thule the geographic coordinates are $\theta = 77.47N$, $\lambda = 290.77^\circ E$. The varying position of Thule through a day has been marked in the diagram by a latitude circle with tics every LT hour. The actual position of Thule at the time 04:37 UT has been marked. At this time the sum of longitude and UT hour angle is:

$$Longitude + UThr \cdot 15^\circ = 290.77^\circ + 4.61 \cdot 15^\circ = 360^\circ$$

Hence Thule is at this time positioned at local midnight and $U_{PROJ} = U_0$. In the figure the optimum direction (OD) is marked by a bold green vector. The projection angle, U_{PROJ} , from the X-axis (North direction) is counted clockwise in the diagram since the Z-axis is downward. Using instead the complement angle $V_{PROJ} = U_{PROJ} - 270^\circ$, and UT time instead of LT, then the projection of ΔF defined in Eq. 4.2. through the projection of components ΔX and ΔY is now given by:

$$\Delta F_{PROJ} = \Delta X \cdot \sin(V_{PROJ}) - \Delta Y \cdot \cos(V_{PROJ}) \quad (4.4)$$

where V_{PROJ} is defined as a function of $UThr$ (UT time in hours) through:

$$V_{PROJ} = Longitude + UThr \cdot 15^\circ + \text{optimum direction angle (ODA)} \quad (4.5)$$

Thus the optimum direction angle is now the angle between the negative Y-axis and the optimum direction (OD). As seen in Fig. 4.1. this angle is also the angle between the midnight-noon direction (here geographical North) and the transpolar equivalent current direction (CD), which by definition is perpendicular to the (optimum) direction for the

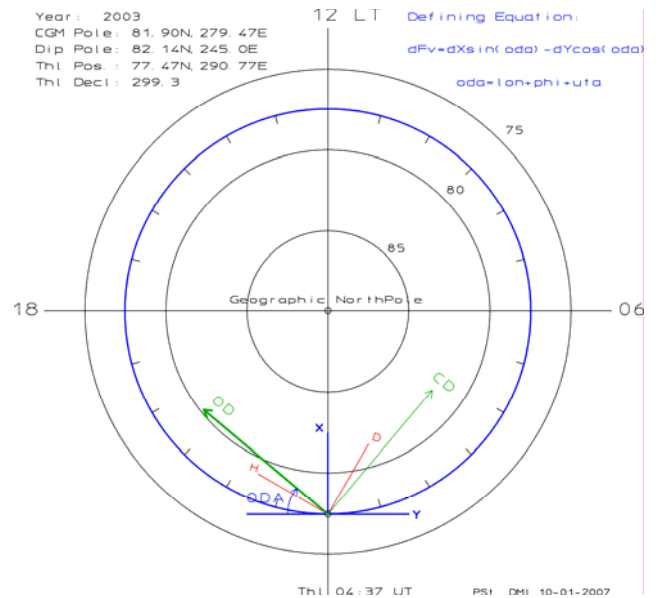


Figure 4.1. Transpolar current direction (CD), optimum direction (OD), and magnetic component directions X and Y for Thule observatory at 04:37 UT in a geographical coordinate system. H and D directions are shown for illustration only.

related magnetic disturbance vector.

The optimum direction angle ($V_0=ODA$) shall be calculated from analyses to find the maximum correlation between the geomagnetic variations measured in the polar cap and solar wind merging electric field values derived from interplanetary spacecraft data. The direction varies with location, season and local time.

In the diagram in Fig. 4.1 the magnetic North direction (H) and magnetic East (D) are indicated by dashed red lines. In the present formulation of the optimum direction angle these directions, as well as the magnetic declination angle, Decl, are not used.

4.2. Earlier definition of optimum angle by Vennerstrøm et al.

The above definition of optimum angle and projection of components is meant to be equivalent to the definition given, for instance, in Vennerstrøm et al. (1994). Disregarding the QL variations they resolve the field into **H** and **D** disturbance components, hence:

$$\Delta H = H_{RAW} \cdot \cos(\Delta Decl) - H_0 \quad (4.6a)$$

$$\Delta D = H_{RAW} \cdot \sin(\Delta Decl) \quad (4.6b)$$

$$\Delta Decl = Decl_{RAW} - Decl_0 \quad (4.6c)$$

where H_{RAW} is the recorded absolute field magnitude while H_0 is the base value of the horizontal field magnitude (defined every 1 Jan) adjusted to actual day-of-year. Similarly, $Decl_{RAW}$ is the recorded declination while $Decl_0$ is the base value (1 Jan) adjusted to the actual day-of-year.

For Thule the projection to the optimum direction is defined in Vennerstrøm et al. (1994) through the equation:

$$\Delta F_{PROJ} = \Delta H \cdot \sin(V_{PROJ}) - \Delta D \cdot \cos(V_{PROJ}) \quad (4.7)$$

where the projection angle now includes the magnetic declination angle, Decl :

$$V_{PROJ} = Longitude - Decl + UThr \cdot 15^\circ + opt.dir.angle (ODA) \quad (4.8)$$

The diagram in Fig. 4.2, corresponding to the diagram in Fig. 4.1, attempts to illustrate the angles graphically. Here, in a geographical latitude – local time system, a circle illustrating the daily path of Thule in local time has been plotted. The position of Thule has been marked at the time 00:34 UT since at this time:

$$Longitude - Decl + UThr \cdot 15^\circ = 290.77^\circ - 299.30^\circ + 8.53^\circ = 0 \quad (4.9)$$

Thus, at 00:34 UT time the magnetic North direction (**H**) is parallel to the LT midnight-noon direction (toward the Sun). According to Eq. 4.7 the projection angle, V_{PROJ} , equals the angle between the negative **D** direction and the optimum direction while according to Eqs. 4.8 and 4.9 the projection angle at this UT time equals the optimum direction angle (*ODA*).

The optimum angle defined by Eqs. 4.7 and 4.8 and depicted in Fig. 4.2 is also here equal to the angle between the midnight-noon meridian and the equivalent current direction. The X- (North) and Y- (East) directions are marked in Fig. 4.2. but not used here.

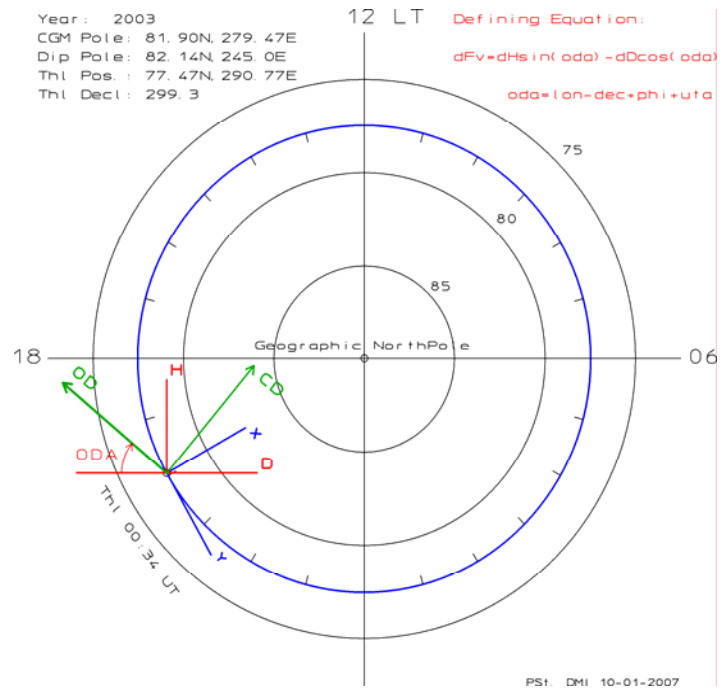


Figure 4.2. Transpolar current direction (CD), optimum direction (OD), and directions of magnetic components H and D for Thule observatory at 00:34 UT in a geographical coordinate system.

It should be noted, that the optimum direction angle in this definition based on the field components H and D in a local geomagnetic coordinate system has the same physical interpretation as the optimum angle defined from the disturbance field resolved in X and Y components in a local geographical coordinate system. Also in this case the optimum direction angle is equal to the angle between the equivalent current direction (CD) and the midnight-noon direction, albeit defined at a different UT time.

4.3. Unified procedure for calculation of optimum direction.

The scaling parameters have been derived over a span of 29 years using primarily IMP-8 satellite data (1975-1999). For the recent years (2000-2003) ACE data are used. The availability of IMP 8 satellite data is illustrated in Fig. 2.1. The satellite must provide valid solar wind (SW) velocity and interplanetary magnetic field (IMF) data collected outside the Earth's magnetosphere and bow shock.

In order to correlate the satellite data with polar ground-based magnetic data it is important to adjust the relative timing of samples. The satellite data are first shifted to a reference position at 12 Re in front of the Earth by imposing a time shift equal the difference in the X coordinates of this position and the actual satellite position in a Geocentric Solar-Ecliptic (GSE) or Solar-Magnetospheric (GSM) coordinate system divided by the solar wind velocity V_x . For IMP 8 this time shift is usually a few minutes only.

Next the satellite data are referred to the Polar Regions by imposing a shift corresponding to an anticipated delay of 20 min between the time of SW and IMF parameters at 12 Re and the time of the resulting effects on the polar ionospheric convection as observed from Thule. This delay is an average value based on statistical studies (see section 7.1.).

For this study both IMP 8 and Thule magnetic data are initially provided as 1-min samples. Now, "sorted" 15-min samples are formed from the 1-min data by omitting the maximum and minimum values (removal of singular spikes) and averaging the remaining 1-min values within each 15-min interval. These 15-min samples are the basis for correlation of Thule magnetic disturbance, Fv , and Imp 8 merging electric field, Em .

For each small sequence of years (typically 5) of the available data interval (1975-2003) the correlation is examined. First the average MEF values, Em_a , are calculated for each specific UT hour through each specific month of the few years of data.

For these years and for each month and each UT hour of the day and with steps of 10^0 in the optimum direction angle through all possible directions the correlation between Thule magnetic disturbances and the solar wind MEF is calculated. The disturbance vector ΔF defined by Eqs. 4.1a and 4.1b is projected to the optimum direction according to Eqs. 4.4 and 4.5. The average, Fv_a , of the projected disturbance vector, Fv , through all possible samples of the specific month for the specific UT hour is calculated.

Now, for each UT hour of the month the correlation coefficient can be calculated as function of optimum direction angle in steps of 10^0 through the interval from 0^0 to 360^0 .

$$R = \frac{\sum((Fv-Fv_a)(Em-Em_a))}{\sqrt{(\sum(Fv-Fv_a)^2 \sum(Em-Em_a)^2)}} \quad (4.10)$$

where the summation is extended over all available 15-min samples through the data interval.

Among the calculated values of the correlation coefficient for all steps in optimum direction angle the maximum value is found. A least squares fit is used to form a parabola to represent the variation in correlation coefficient as a function of optimum angle based on this maximum value along with the preceding 2 and the following 2 values of the correlation coefficient. The parabolic function is then used to determine the precise value of the optimum direction angle for the given month and UT hour. The value of the maximum correlation coefficient is also determined with this least squares parabola function.

When based on data from a single month the hourly values of the optimum direction angle (ODA) will show strong fluctuations which will not be reproduced if the corresponding calculations are made for another epoch. In order to make the values more generally representative some averaging and smoothing is necessary. In the first step the average value of 5 years of ODA was formed. These values are then exposed to Gaussian smoothing over month and UT hour by averaging using the weight function:

$$WG = \exp\left\{ -\frac{(H - H0)^2}{XHR^2} - \frac{(M - M0)^2}{XMD^2} \right\} \quad (4.11)$$

where H is the variable UT hour, $H0$ is the selected UT hour and XHR is the half-width of the Gaussian weight function for the time-of-day. Correspondingly, M is the variable month, $M0$ is the selected month and XMD is the half-width of the Gaussian weight function for month-of-the-year. The summations involved in the averaging are extended to 3 times the width of the Gaussian. Provisions are, of course, made for summation beyond the 24 hours of a day and 12 months of a year. Typical values in this case are $XHR=3$ hours and $XMD=1.5$ month.

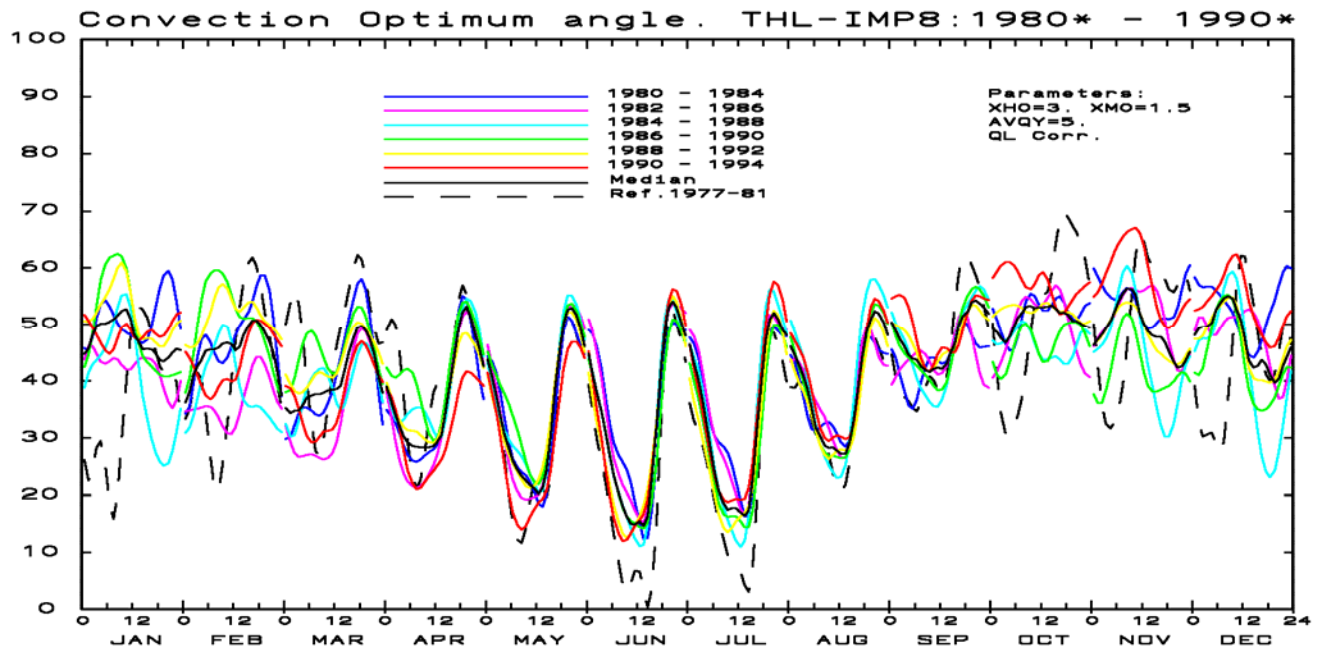


Figure 4.3. Calculation of optimum direction angle (ODA) vs UT hour and month with QL correction of Thule data. Each colour-coded trace (consisting of 12 separate monthly curves vs. UT time) represents average values through epochs of 5 consecutive years. The black curves depict median values of the 6 colour-coded traces. The dashed black curves represent the corresponding optimum direction angles used in Vennerström et al., 1994.

The optimum direction angle values are now calculated over 6 epochs shifted by 2 years at a time. The results (data sets of an optimum direction angle for each UT hour of the day and each month of the year) are displayed in Fig. 4.3. There is a colour-coded trace for each epoch. Since each epoch is 5 years in extent and the shift only 2 years then there are some overlapping of epochs.

It is seen in Fig. 4.3. that during the summer months (May-August) there is quite good agreement between data from the different epochs while during the winter months there are strong disagreements. A closer inspection of each set indicates that there is a phase shift between summer and winter season in the daily variation of the optimum direction angle. This phase shift occurs at different times in the different epochs most likely depending on the phase of the years within the 11-year solar cycle.

The agreement in the optimum direction angles derived during summer months and the differences appearing during winter months in the different epochs is also observed when comparing the results obtained here to the optimum direction angle values derived by Vennerström et al., 1994, on basis of data from the epoch 1977-1981. These values are displayed in Fig. 4.3 by the black dashed trace.

In order to extract regular variations and reduce singular fluctuations the median values are calculated from the 6 colour-coded traces displayed in Fig. 4.3. The median values in this case represent averaging over 15 years. They are shown by the black trace in Fig. 4.3.

Finally, the available median traces from data sets like that displayed in Fig. 4.3 are displayed and combined into a "grand median" trace for the optimum direction angle as displayed in Fig. 4.4. Now, the differences between values of the individual data sets and the "grand median" are generally less than 5° except for a few odd data points. Again, the black dashed trace represents values from Vennerström et al., 1994. As noted earlier, there is fair agreement during summer months while during the winter months the large excursions in the optimum direction angles from Vennerström et al. are not reproduced in the median values calculated here. The difference could be as large as 30° .

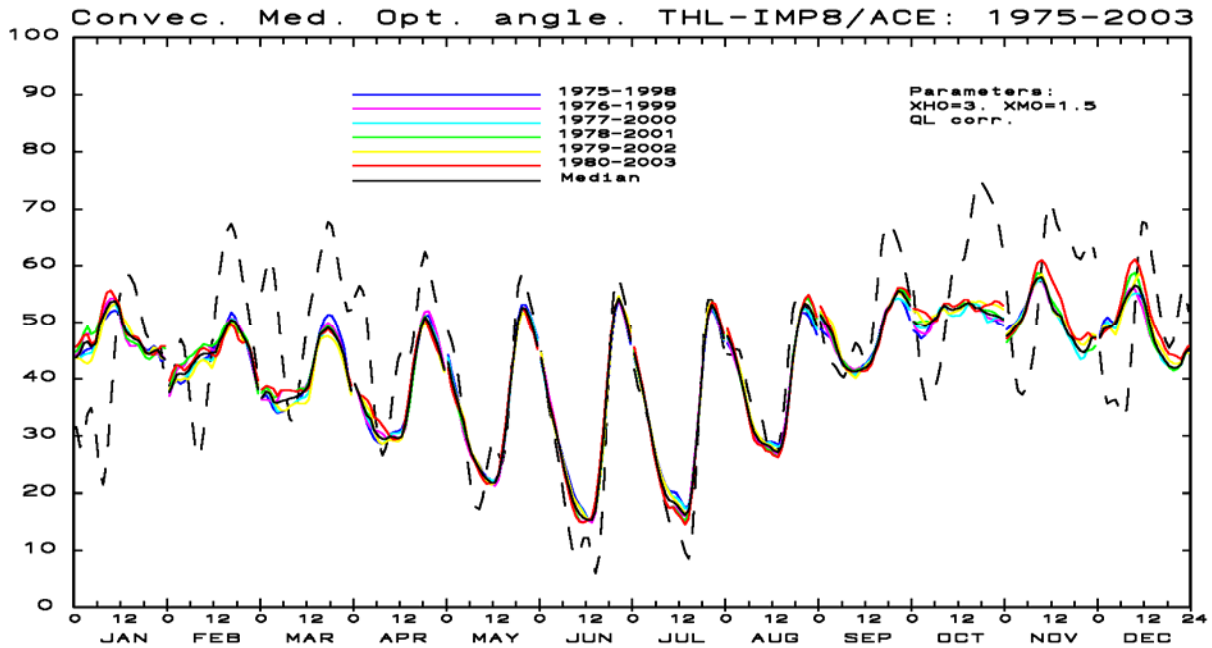


Figure 4.4. Sets of calculated median optimum direction angle (ODA) vs UT hour and month. QL correction of data. Each colour-coded trace (consisting of 12 separate monthly curves vs. UT time) represents average values through epochs of 15 consecutive years. The black curves depict grand median values of the 6 colour-coded traces. The dashed black curves represent the corresponding optimum direction angles used in Vennerström et al., 1994.

The resulting "grand median" optimum direction angle values (the black traces in Fig.4.4) represents data averaged over a total epoch of 29 years from 1975 to 2003. The main satellite data source is IMP 8 corresponding to the data availability displayed in Fig. 2.1. For the recent years 2000 to 2003 ACE data have been used. The grand median values are considered the best possible set to represent the optimum direction angle through all phases of the solar activity cycle and with a degree of averaging and smoothing such that singular (random) fluctuations are reduced to a level significantly below the systematic repetitive variations. The grand median (1975-2003) values shall be used as reference optimum direction angles in calculations of PC-North index values. The values are listed in Table 4.1.

Table 4.1. Grand median opt. dir. angle. Thule-IMP8/ACE data interval: 1975 - 2003 QL corr.

HR	JAN	FEB	MAR	APR	MAY	JUN	JUL	AUG	SEP	OCT	NOV	DEC
0	43.9	37.7	36.7	39.1	42.9	43.6	44.5	47.7	51.3	50.1	47.7	47.4
1	44.6	39.3	37.8	37.2	39.8	40.2	41.7	46.2	50.2	49.7	48.3	48.9
2	46.3	40.9	37.5	35.3	36.8	36.2	38.3	44.1	49.3	49.6	49.2	49.3
3	46.7	41.0	36.0	33.6	34.7	33.0	34.9	41.2	47.9	49.5	49.8	49.4
4	46.1	41.3	35.8	33.0	32.2	30.2	31.6	38.4	45.7	49.8	50.8	49.9
5	46.7	41.7	36.2	31.0	29.3	27.2	28.0	35.5	43.7	50.4	52.6	51.3
6	49.8	42.9	36.3	29.8	27.0	24.0	24.7	32.5	42.3	50.9	55.1	53.2
7	51.0	43.7	36.6	29.5	25.5	21.0	21.8	30.5	41.8	52.3	56.8	54.7
8	52.7	44.2	36.8	29.5	24.1	18.8	19.8	29.1	41.3	53.0	57.7	55.7
9	53.5	44.5	36.9	29.8	23.0	17.4	18.8	28.7	41.2	52.3	58.1	56.6
10	53.8	44.5	37.3	29.9	22.4	16.3	18.5	28.5	41.3	52.2	56.7	56.3
11	52.8	44.7	38.1	29.5	21.8	15.6	18.0	28.1	41.8	52.3	54.4	54.8
12	49.8	44.8	38.9	29.9	21.8	15.4	17.0	27.5	42.2	52.5	52.4	52.5
13	48.4	46.7	41.8	32.2	23.1	15.4	16.3	27.1	43.0	53.2	51.6	49.8
14	47.6	47.9	45.3	36.2	26.5	17.0	17.0	28.4	44.7	53.4	51.0	46.7
15	47.0	49.7	47.9	41.3	31.5	22.1	21.3	31.5	46.7	53.3	49.2	45.1
16	46.8	50.5	48.7	46.1	38.2	30.4	28.5	37.2	49.6	52.7	47.8	44.2
17	45.9	50.2	49.2	49.5	45.2	39.4	37.6	43.7	52.0	52.6	47.3	43.2
18	44.8	49.0	48.8	51.0	50.1	47.3	46.3	48.8	53.1	52.0	45.9	42.3
19	44.7	47.8	47.8	50.0	52.6	52.6	51.3	51.8	54.4	51.5	44.9	41.9
20	45.1	46.5	46.8	48.4	52.5	54.3	53.2	53.3	55.5	51.3	44.7	42.0
21	45.3	44.9	44.5	46.4	50.8	52.8	52.1	52.9	55.3	51.3	45.5	42.6
22	44.0	41.3	40.8	44.2	48.5	50.0	49.8	51.4	54.4	51.0	47.3	44.5
23	43.5	38.3	37.9	41.6	45.8	46.8	47.2	49.5	53.0	50.7	47.5	45.3

4.4. Alternate procedure for calculation of optimum direction.

In order to investigate the effect of including QL correction in the processing of ground magnetic data we have made calculations of the optimum direction angle using exactly the same procedure as that described above in sections 4.1 and 4.3 except for the subtraction of QL level shown in Eqs. 4.1a and 4.1b. The results are displayed in Fig. 4.5 and 4.6. The grand median values are shown in Table 4.2.

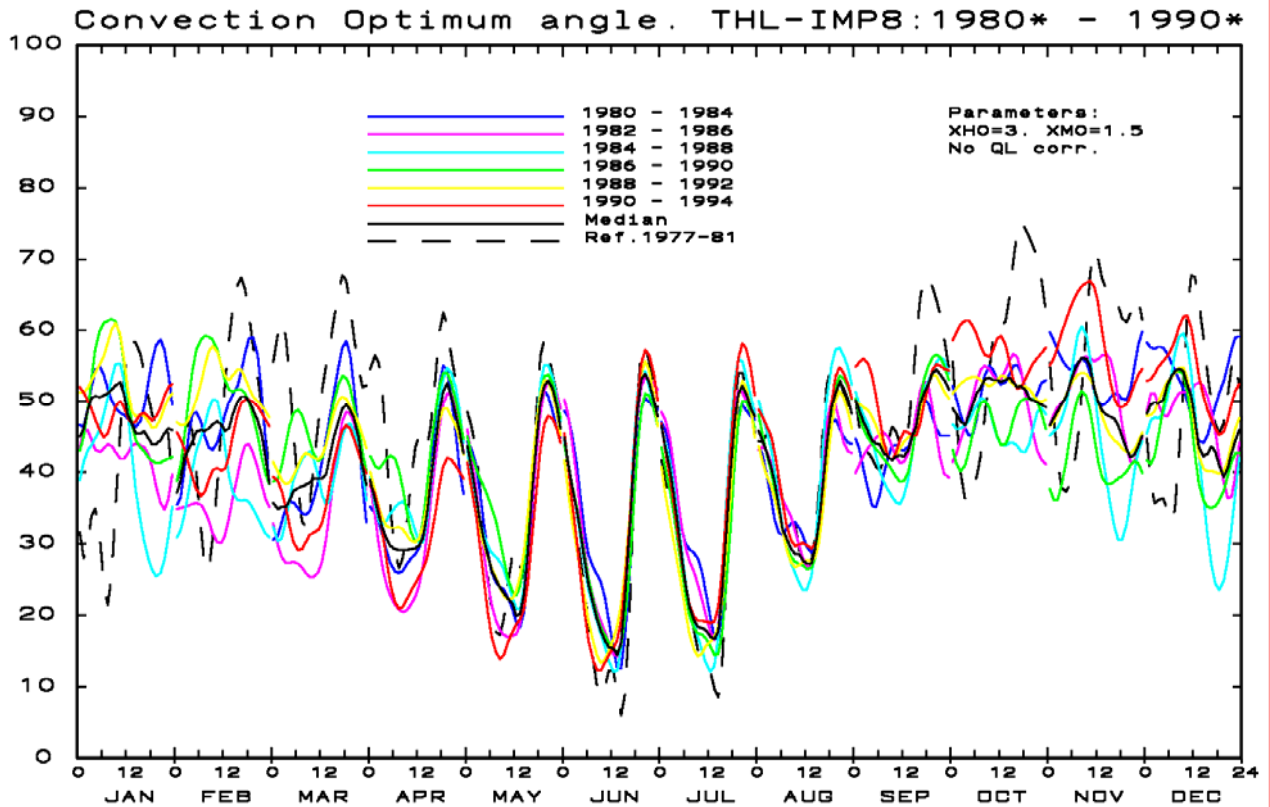


Figure 4.5. Calculation of optimum direction angle (ODA) vs UT hour and month without QL correction of Thule data. Each colour-coded trace (consisting of 12 separate monthly curves vs. UT time) represents average values through epochs of 5 consecutive years. The black curves depict median values of the 6 colour-coded traces. The dashed black curves display the corresponding optimum direction angles used in Vennerström et al., 1994.

Like noted for Fig. 4.3. it is seen in Fig. 4.5. that during the summer months (May-August) there is quite good agreement between data from the different epochs while during the winter months there are strong disagreements since it appears, again, that there is a phase shift between summer and winter season in the daily variation of the optimum direction angle. This phase shift occurs at different times in the different epochs.

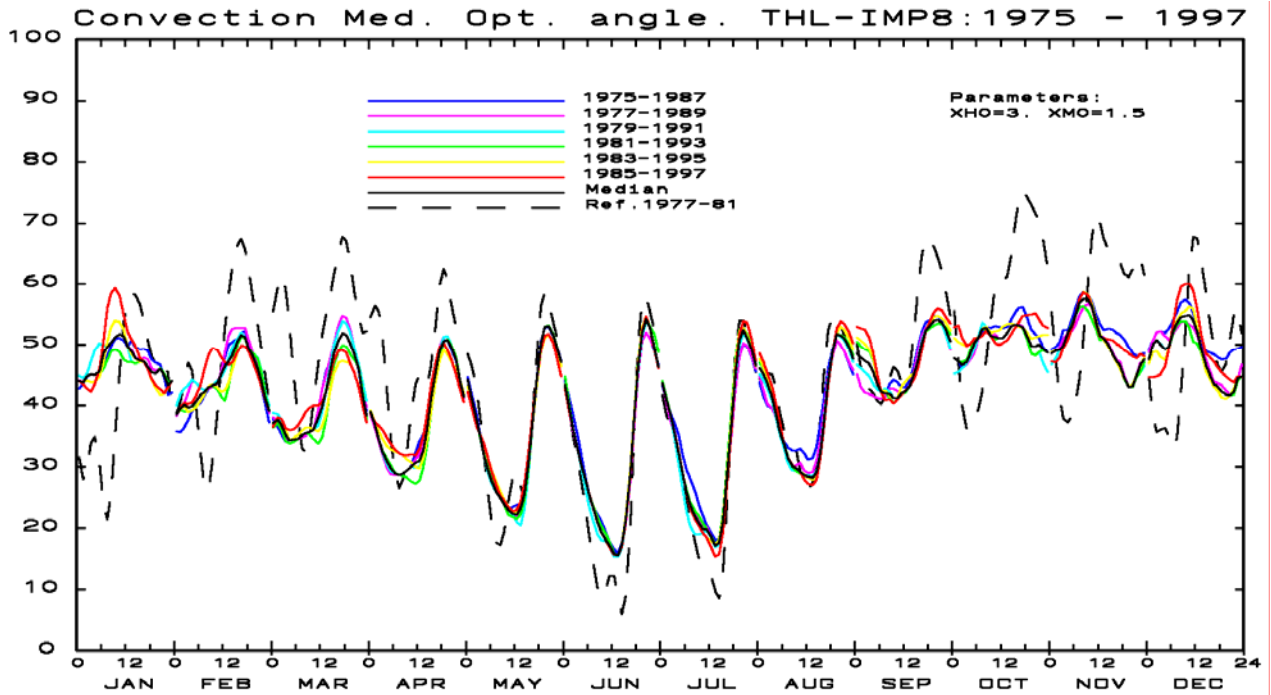


Figure 4.6. Sets of calculated median optimum direction angle (ODA) vs UT hour and month without QL correction of data. Each colour-coded trace (consisting of 12 separate monthly curves vs. UT time) represents average values through epochs of 15 consecutive years. The black curves depict grand median values of the 6 colour-coded traces. The dashed black curves display the corresponding optimum direction angles used in Vennerstrøm et al., 1994.

Table 4.2. Grand median optimum direction angle. Thule-IMP8 data interval: 1975-1999. No QL corr.

HR	JAN	FEB	MAR	APR	MAY	JUN	JUL	AUG	SEP	OCT	NOV	DEC
0	44.0	38.6	37.2	39.0	44.3	43.4	43.8	46.1	48.6	47.8	48.6	47.6
1	43.8	39.5	37.8	36.8	41.3	39.9	41.1	45.2	47.9	47.3	49.0	50.0
2	44.8	40.2	36.8	34.4	37.9	36.4	38.3	43.5	47.4	46.8	49.2	50.8
3	45.2	39.7	35.3	32.4	35.0	33.0	35.4	41.4	46.8	47.2	49.9	50.0
4	45.0	39.9	34.4	31.0	31.8	30.3	32.3	38.6	45.5	48.8	52.0	49.3
5	45.5	40.8	34.5	29.8	29.5	28.1	28.9	35.7	43.7	50.3	53.3	49.8
6	48.5	41.8	34.6	29.0	27.5	25.5	25.9	33.8	42.3	51.3	55.0	52.3
7	49.7	42.3	35.2	28.7	25.8	23.0	23.6	31.6	42.0	52.7	57.0	53.7
8	50.4	43.0	35.6	28.9	24.9	20.9	22.0	30.1	41.9	52.8	57.6	54.6
9	51.3	43.3	35.7	29.5	23.8	19.3	20.8	29.8	41.3	51.5	57.5	54.8
10	51.8	43.6	36.2	30.0	23.0	18.1	20.0	29.2	41.3	51.3	56.3	54.9
11	51.5	45.0	38.0	30.7	22.4	17.2	19.8	28.8	42.0	51.2	53.9	54.1
12	49.8	46.4	39.8	31.0	22.3	15.8	18.5	28.5	42.3	51.2	51.6	52.3
13	48.9	47.3	42.4	32.7	23.2	15.6	17.1	28.2	43.3	52.0	51.0	49.3
14	47.8	48.5	45.5	36.3	25.7	17.3	17.7	29.1	45.2	53.2	50.0	46.7
15	47.3	50.5	48.7	41.3	30.5	21.4	21.3	32.3	47.2	53.4	48.7	45.2
16	47.3	51.8	50.7	45.6	36.9	29.0	28.6	37.9	50.2	53.3	47.3	43.6
17	46.4	51.3	51.9	49.0	44.7	38.5	37.5	44.1	52.4	52.9	46.6	43.1
18	45.5	49.3	51.7	50.7	50.3	46.5	45.3	49.1	53.3	51.7	44.8	42.4
19	45.3	48.2	50.3	50.8	53.0	51.9	50.8	51.8	54.0	49.8	43.0	41.8
20	46.0	46.1	48.7	49.6	53.2	54.3	52.4	51.6	54.2	49.8	43.2	41.8
21	45.0	43.9	46.0	47.7	51.6	52.9	51.2	51.0	53.7	50.0	45.0	42.3
22	43.4	41.2	41.8	44.2	49.5	49.3	49.2	49.6	52.6	49.3	46.8	44.5
23	44.0	39.1	38.5	41.5	47.1	46.4	46.7	47.7	50.6	48.7	47.6	44.8

Comparison of the values derived with (Figs. 4.4-4.5 and Table 4.1) and without (Figs. 4.6-4.7 and Table 4.2) QL correction of the raw data shows only small differences, mostly less than 1.0° . The differences between either of these values and the values derived by Vennerstrøm et al., 1994, are small during local summer but (again) quite large during winter months.

5. Calculation of Slope and intercept.

5.1. New, unified procedure

Recalling, that we are searching for a proxy based on polar magnetic disturbances to represent the solar wind "Merging Electric Field" ($Em = MEF = V_{SW} B_T \sin^2(\theta/2)$), we increase the correlation between the horizontal disturbance vector ΔF corrected for the quiet daily variations and the MEF by projecting ΔF to a specific direction ("optimum direction"), which varies slowly with local time and season.

The horizontal magnetic vector, like explained in section 4.1., is resolved in an X-component (northward in a geographical coordinate system) and a Y-component (eastward). The base line values are subtracted from the raw data and the QDC values are subtracted as defined in Eqs. 4.1a and 4.1b (i.e., $\Delta X = (X_{RAW} - X_0) - X_{QL}$, $\Delta Y = (Y_{RAW} - Y_0) - Y_{QL}$).

The projection of the disturbance vector ΔF to the optimum direction is defined by Eq. 4.4. ($\Delta F_{PROJ} = \Delta X \cdot \sin(V_{PROJ}) - \Delta Y \cdot \cos(V_{PROJ})$), where the projection angle, V_{PROJ} , is defined as a function of $UThr$ (UT time in hours) through Eq. 4.5. ($V_{PROJ} = Longitude + UThr \cdot 15^\circ + optimum\ direction\ angle$)

A further increase in the correlation between Em and ΔF is obtained by displacing the baseline for the projected magnetic disturbance by an amount, ΔF_b . With this correction of the projected polar magnetic disturbance we assume proportionality between this quantity and the solar wind merging electric field, i.e.:

$$\Delta F_{PROJ} - \Delta F_b = S \cdot Em \quad (5.1)$$

where S is the "Slope" while ΔF_b is the "Intercept" parameter named from a visualized graphical display of ΔF_{PROJ} against Em .

Hence the task is now to calculate the slope and intercept parameters to give the highest possible correlation between the interplanetary merging electric field and the transformed polar magnetic disturbance. The former parameter can, for instance, be based on observations of solar wind velocity, V_{SW} , and interplanetary magnetic field, IMF B_Y and B_Z , from the IMP 8 satellite orbiting at a distance of around 32 Earth radii. Like mentioned in the former section on calculations of the optimum direction for the projection of the magnetic disturbance vector, Thule magnetic recordings and IMP 8 data are available for the 25 years from 1975 to 1999. In addition to IMP 8 data we use data from the ACE satellite for the recent years 2000-2003. Hence, using this combination the correlations can be extended over 29 years, that is, more than two (almost three) 11-year solar activity cycles.

When using regression analysis to derive the slope and intercept parameters we face two conceptual questions. The major part of cases have rather small intensities of solar wind and geomagnetic variations, and the random fluctuations are as large as the total values. Hence in simple regression analyses they tend to dominate but may not provide a proper set of coefficients to represent the larger (and geophysically more important) amplitudes. Furthermore, the cases with very large amplitudes are also problematic since the level of geomagnetic variations may not track the extreme interplanetary disturbances. Consequently we require that the regression parameters should give an optimum "flat" response for the resulting PC index as a function of increasing MEF. In a least squares fit to estimate the regression line of ΔF_{PROJ} on Em we would minimize the deviations in the magnetic variations from the regression line. Thus:

$$S = (\Sigma(Fv \cdot Em) - \Sigma(Fv) \cdot Ema) / (\Sigma(Fv^2) - \Sigma(Fv) \cdot Fva) \quad (5.2)$$

where, using the notation from the preceding section, Fva is the average disturbance value over the ensemble of samples. Correspondingly, Ema is the total average value.

The intercept parameter is now derived from Eqs. 5.1-5.4 through:

$$\Delta F_b = Fva - S \cdot Ema \quad (5.3)$$

A final point to consider is the occurrences of large negative values of the projected magnetic disturbances. Such conditions are usually associated with large positive values of the IMF B_Z component which profoundly change the configuration of ionospheric convection and current systems in the polar cap. Moreover, the proportionality between the non-negative merging electric field and the polar magnetic variations is no longer present. Hence the large negative values of the projected magnetic disturbance should be disregarded

when looking for the best possible association between the merging electric field and the polar magnetic variations. We have in the calculations imposed a limit corresponding to a PC index value of -1.0 for the projected disturbance. This limit corresponds to a range of one standard deviation from zero; hence there is still ample room for statistical fluctuations of the actual PC index around zero or small amplitudes.

With this procedure we have calculated sets of hourly values of the slope, S , and the intercept parameter, ΔF_I for each month of the year. In order to minimize singular fluctuations caused, for instance, by solar flare activity and associated geomagnetic storms we have used a combination of averaging and smoothing like that described in the previous section on optimum direction. In the first step we have calculated averages of samples for each specific hour and month summed over several consecutive years. In this section we use, consistently, summation over 5 years (i.e. around half a solar cycle). In the next step we use 2-D Gaussian smoothing over time-of-day and month-of-year. Here we use a weight function with half-width of 2 hours in time and 1 month in season, respectively, and extend the summation involved in the smoothing process over 3 times the Gaussian width. An example of the results is displayed in Fig. 5.1. for the slope and in Fig. 5.2. for the intercept.

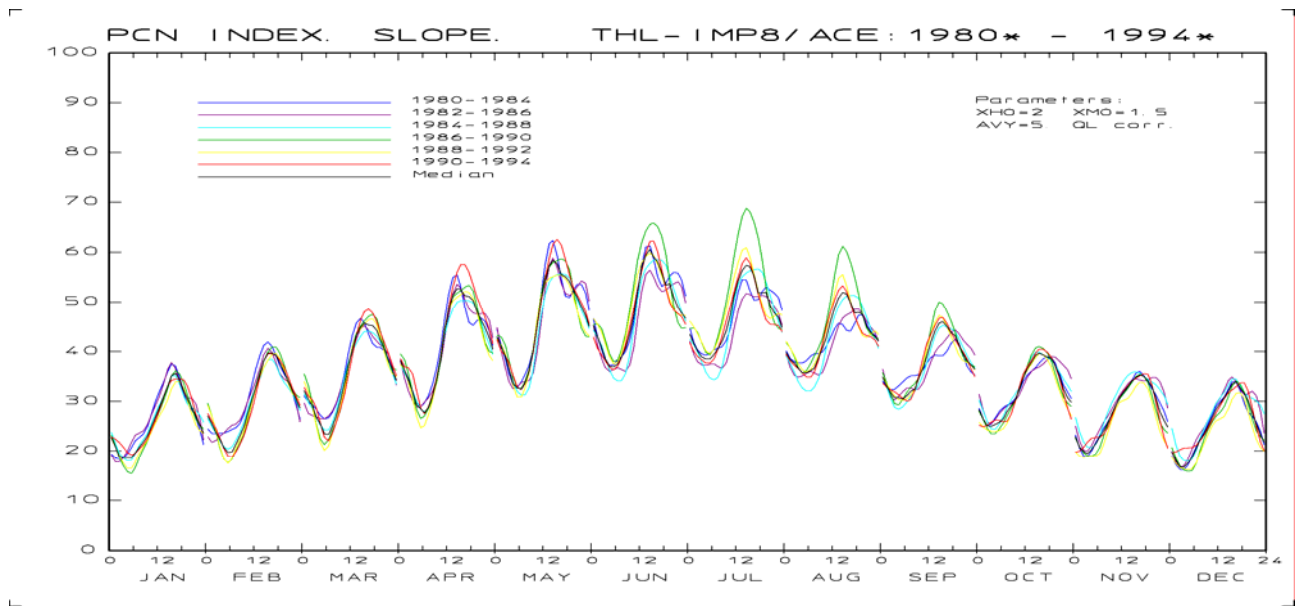


Figure 5.1. Calculation of slope for ΔF_{PROJ} against Em . Averaging over 5 years. 2-D Gaussian smoothing use half-widths of 2 hours for time-of-day and 1 month for season, respectively. QL correction of data.

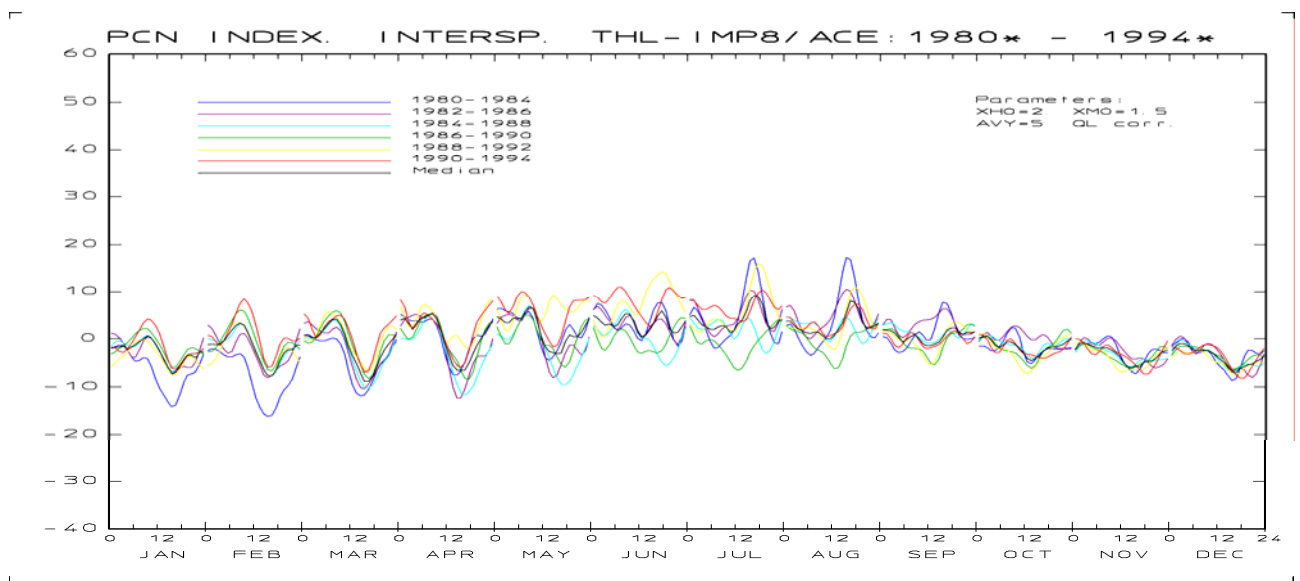


Figure 5.2. Calculation of intercept for ΔF_{PROJ} against Em . Averaging over 5 years. 2-D Gaussian smoothing use half-widths of 2 hours for time-of-day and 1 month for season, respectively. QL correction of data.

The data for each epoch of 5 consecutive years have been plotted in a specific colour. At the left in the top of the diagram is a definition of the use of colours. Each colour-coded trace consists of separate curves for the variation with UT time-of-day for the 12 months of the year. The black trace depicts the median values.

There is a considerable overlap between the displayed data sets since the epoch is 5 years for each trace and the data interval is shifted by only 2 years from one trace to the next. However, since the displayed data spans 15 years, the variations among traces still illustrate differences over the 11-year solar cycle. The median values shown in the black trace represent the systematic time-of-day and month-of-year variations.

In a further step to extract the systematic variations and minimize fluctuations the median curves from data sets like those displayed in Figs.5.1. and 5.2. have been combined to define the "grand median" over the total span of available data, that is, Thule and IMP 8 or ACE data from 1975 through 2003. This is illustrated in the diagrams in Figs. 5.3. and 5.4.

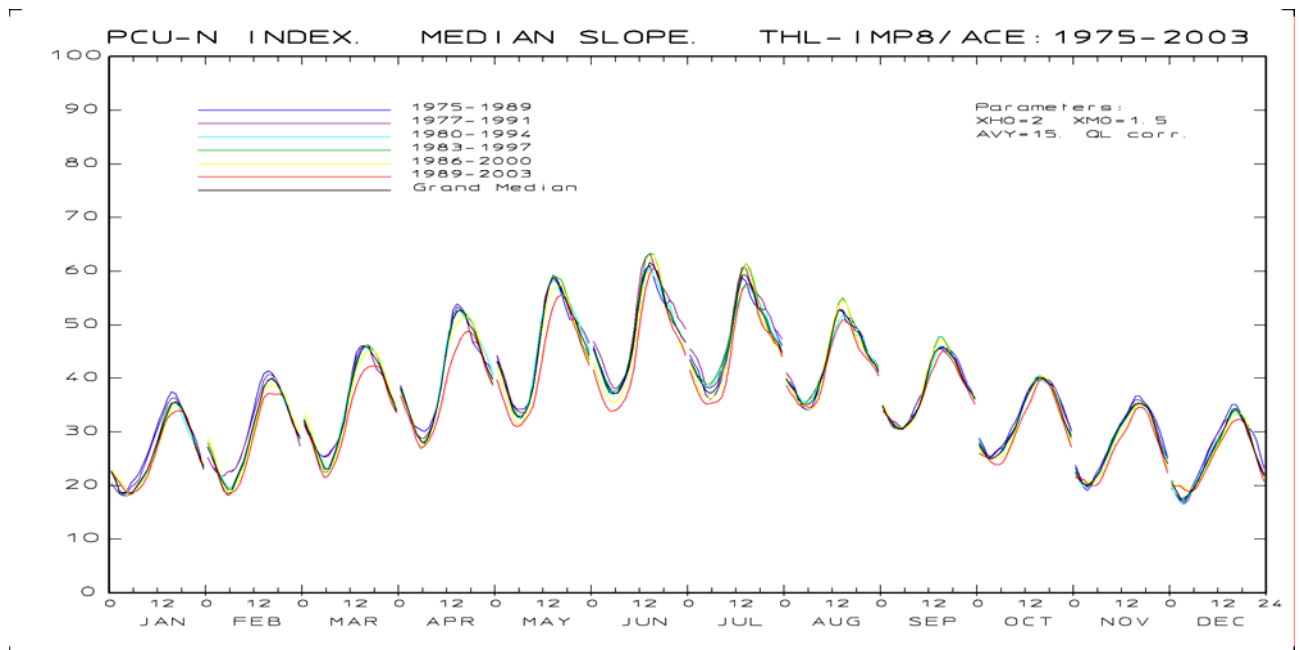


Figure 5.3. Grand median slope over 29 years for ΔF_{PROJ} against Em . Raw data corrected for QL

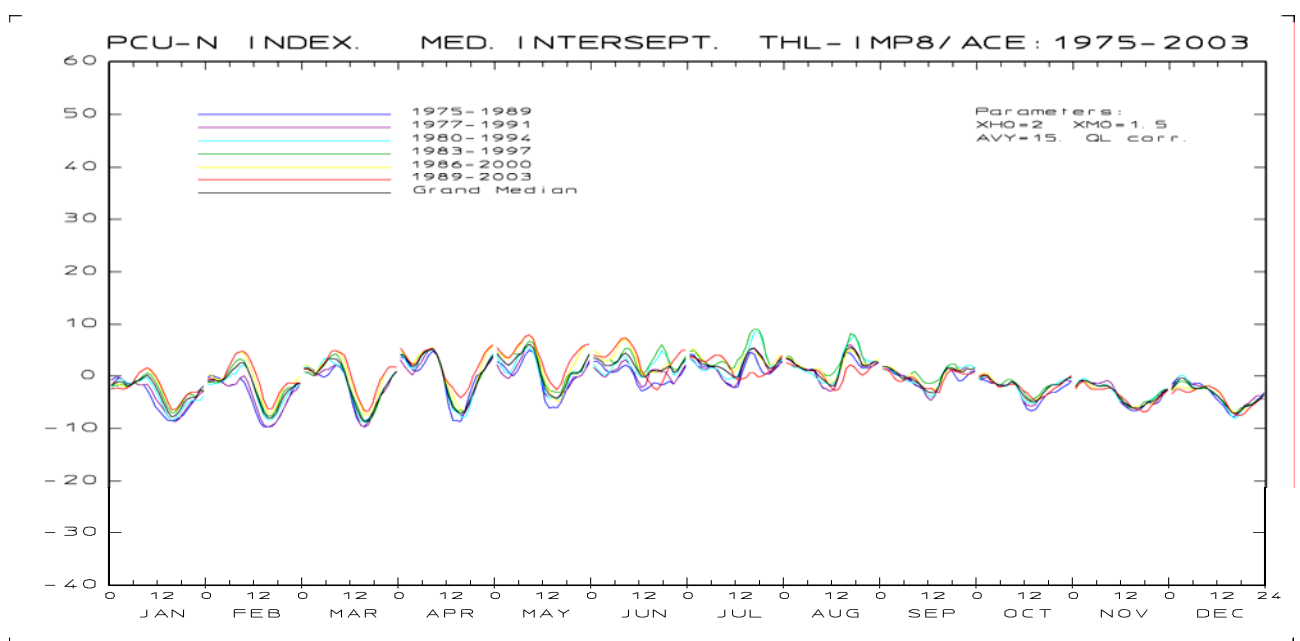


Figure 5.4. Grand median over 29 years of intercept parameter for ΔF_{PROJ} against Em . QL corr.

Each colour-coded trace in Figs. 5.3. and 5.4. represent data for an epoch of 15 years. There is a shift of 3 years from one trace to the next. Thus, the traces in Figs. 5.3 and 5.4 represent data over 29 years, that is, almost three 11-year solar activity cycles. The main satellite data source is IMP 8 corresponding to the data availability displayed in Fig. 2.1. For the recent years 2000 to 2003 ACE data have been used. It is now seen clearly that the singular fluctuations have been reduced to a level significantly below the systematic, repetitive variations with time-of-day and month-of-year. The grand median (1975-2003) values shown in the black traces in Figs. 5.3. and 5.4. shall be used in calculations of PC-North index values. The values are listed in Tables 5.1. and 5.2.

Table 5.1. *PCN-U grand median slope. Thule-IMP8/ACE data: 1975 - 2003 (QL corr.)*

HR	JAN	FEB	MAR	APR	MAY	JUN	JUL	AUG	SEP	OCT	NOV	DEC
0	22.6	27.2	32.0	38.2	43.2	45.5	43.5	39.9	34.9	28.0	22.5	20.3
1	21.0	25.5	30.2	36.1	41.3	43.3	41.8	38.7	33.2	26.4	21.1	19.2
2	19.1	23.5	28.5	34.0	38.8	41.1	40.3	37.7	32.0	25.3	20.4	17.5
3	18.5	21.8	26.9	31.8	36.5	39.0	39.2	36.3	31.0	25.0	20.0	17.3
4	18.8	20.5	25.1	29.7	34.0	37.5	37.7	35.2	30.7	25.4	20.5	18.1
5	18.6	19.4	23.3	28.4	32.9	37.1	37.2	35.1	30.6	25.9	21.5	19.1
6	19.5	19.4	23.0	28.0	32.8	37.3	37.7	35.4	31.4	26.9	22.7	20.4
7	20.6	21.1	24.7	29.1	33.7	38.6	38.8	36.2	32.0	28.1	24.1	21.7
8	21.8	22.9	26.9	31.3	35.3	40.3	41.0	38.2	33.3	29.3	26.0	23.3
9	23.0	24.6	29.4	34.4	38.4	42.9	43.6	40.7	34.8	30.7	27.9	24.9
10	24.9	27.1	32.2	38.3	42.9	47.0	46.9	43.1	37.1	33.0	29.5	26.5
11	27.0	30.0	36.5	42.9	48.7	52.2	51.5	46.6	40.1	34.8	31.0	27.9
12	29.3	33.0	40.0	47.6	54.1	57.3	56.0	50.4	43.0	36.8	32.0	29.1
13	31.8	35.7	43.0	51.1	57.4	60.0	59.2	52.8	45.0	38.2	33.2	30.7
14	33.8	38.3	44.9	52.6	58.8	61.6	59.2	52.7	45.7	39.3	34.5	32.3
15	35.3	39.6	45.9	52.7	58.1	61.0	57.8	51.7	45.8	40.1	35.1	33.8
16	35.6	39.9	45.8	51.9	56.5	59.5	56.1	50.5	45.3	40.0	35.3	34.3
17	34.8	39.3	44.5	50.2	55.1	56.8	53.2	49.1	44.5	39.4	35.2	33.3
18	33.8	38.1	43.3	49.2	53.1	53.5	52.2	48.5	43.3	38.6	34.5	31.9
19	32.0	36.4	42.2	47.4	51.6	52.6	51.2	47.0	41.5	37.0	32.9	30.5
20	29.9	34.2	40.0	45.3	50.1	50.6	48.8	44.8	39.7	34.8	30.4	27.9
21	27.4	32.2	37.8	42.8	47.8	49.1	47.3	43.5	38.3	32.4	27.6	25.4
22	25.3	30.1	36.2	41.0	46.3	47.8	46.5	42.7	37.5	30.6	25.5	23.3
23	23.5	28.8	34.0	39.8	44.3	46.7	44.8	41.5	36.3	29.3	24.1	21.9

Table 5.2. *PCN-U grand median intercept. Thule-IMP8/ACE data: 1975 - 2003 (QL corr.)*

HR	JAN	FEB	MAR	APR	MAY	JUN	JUL	AUG	SEP	OCT	NOV	DEC
0	-1.8	-0.8	1.5	4.2	4.3	3.5	3.9	3.5	1.8	-0.3	-2.0	-2.6
1	-1.3	-0.6	1.5	3.8	3.3	3.3	3.8	3.2	1.8	0.1	-0.9	-1.3
2	-1.0	-0.8	0.8	2.8	2.5	2.8	3.2	2.3	1.4	0.2	-0.8	-0.4
3	-1.0	-0.9	0.5	1.8	2.0	2.0	2.3	1.9	0.9	-0.6	-0.9	-0.4
4	-1.9	-0.6	1.4	2.2	2.9	2.0	2.2	1.5	0.2	-1.3	-1.3	-1.0
5	-1.5	0.2	2.3	3.8	3.8	2.3	1.9	1.2	-0.6	-1.8	-1.7	-2.1
6	-1.0	1.1	3.3	4.5	4.4	2.8	1.9	1.1	-0.3	-1.9	-1.9	-2.3
7	-0.8	1.6	3.3	4.9	5.4	3.9	1.9	1.3	-0.4	-1.7	-1.7	-2.3
8	-0.2	2.5	3.3	5.2	6.1	4.4	1.5	0.2	-0.9	-1.0	-1.8	-2.0
9	0.2	2.6	2.5	4.2	5.4	3.7	1.0	-0.5	-1.4	-1.4	-2.3	-2.4
10	-0.5	1.4	0.8	2.1	3.3	2.3	0.4	-1.1	-2.3	-2.5	-3.0	-3.1
11	-1.8	-0.6	-1.6	-1.0	0.1	1.0	-0.2	-1.8	-2.9	-3.7	-4.1	-3.5
12	-3.3	-3.0	-4.0	-3.8	-2.3	0.0	-0.3	-1.8	-3.2	-4.4	-4.9	-4.3
13	-5.1	-5.2	-6.0	-5.9	-3.4	-0.2	2.1	0.1	-3.2	-4.8	-5.4	-5.1
14	-6.8	-6.9	-7.9	-6.7	-3.9	0.9	4.0	3.5	-1.8	-4.9	-6.0	-6.1
15	-7.7	-7.9	-8.6	-7.1	-4.3	1.0	5.1	5.1	0.4	-4.3	-6.1	-6.9
16	-7.5	-7.9	-8.3	-6.6	-3.5	0.9	5.4	5.6	1.6	-3.2	-6.0	-7.2
17	-6.5	-6.9	-7.1	-5.0	-1.9	1.0	4.3	4.9	1.5	-2.3	-5.6	-6.6
18	-5.2	-5.3	-5.3	-3.0	0.3	1.5	3.4	3.7	1.3	-1.7	-4.9	-5.9
19	-4.3	-3.7	-3.7	-1.2	0.7	2.0	2.2	2.1	1.0	-1.7	-4.9	-5.6
20	-4.1	-2.8	-2.2	0.5	0.6	0.7	1.4	2.0	0.8	-1.5	-4.5	-5.4
21	-4.1	-2.2	-1.0	1.5	1.0	1.0	1.8	2.3	1.5	-1.0	-3.8	-4.8
22	-2.8	-1.5	0.1	3.0	2.8	2.3	2.8	2.8	1.2	-0.4	-2.9	-4.3
23	-2.7	-1.3	0.9	4.0	4.1	3.3	3.5	2.7	1.5	-0.2	-2.4	-3.5

5.2. Comparison with former procedures.

The calculations outlined in section 5.1 differs in two important ways from the procedures used by Vennerstrøm et al., 1994. Firstly, the polar magnetic variations used in the calculations of the "unified" procedures outlined in section 5.1. have been corrected for the varying "Quiet Level" (QL) here derived from minimum variance analysis. In Vennerstrøm et al., 1994, the data are used without this correction. The main consequence of this difference in QL handling appears through the related changes in the so-called intercept parameter (see sec.5.1).

If the variations with the 11-year solar activity cycle were not present then, in principle, all the QL-variations in the projected magnetic variations should come on top of the resulting intercept parameter, that is:

$$\Delta F_b(\text{no QL correction}) = \Delta F_b(\text{with QL correction}) - \text{QL}(\text{projected}) \quad (5.6)$$

However, the varying solar activity introduces changes in the QL data. Hence, if a solar cycle-independent intercept parameter is used for the calculation of the PC index then the correspondence in Eq. 5.6 will no longer be valid, and the PC index values calculated from using the two different procedures will not be the same.

A second major difference between the calculations used in Vennerstrøm et al., 1994, and those outlined in section 5.1, is the lengths of the epochs with available satellite and ground data. The data basis used by Vennerstrøm et al., 1994, extend through the 4 years 1977-1980 which represent part of the rise from solar minimum in 1976/77 to solar maximum in 1981/82. The data basis used here extends through the 29 years from 1975 to 2003, that is, over more than two 11-year solar cycles. More precisely the 29 years comprise 3 solar maximum intervals and 2½ solar minimum intervals.

Other (smaller) differences between the two calculation procedures include the averaging and smoothing procedures used.

In order to illustrate the changes introduced by the QL corrections and also to illustrate other differences between the Vennerstrøm et al. procedures and those used in the new calculations we have repeated all calculations using identical data and procedures except for the QL corrections. The results are displayed in Figs.5.5-5.8 equivalent to Figs.5.1-5.4 (which were using QL corr.) and in Tables 5.3. and 5.4. equivalent to Tables 5.1. and 5.2.

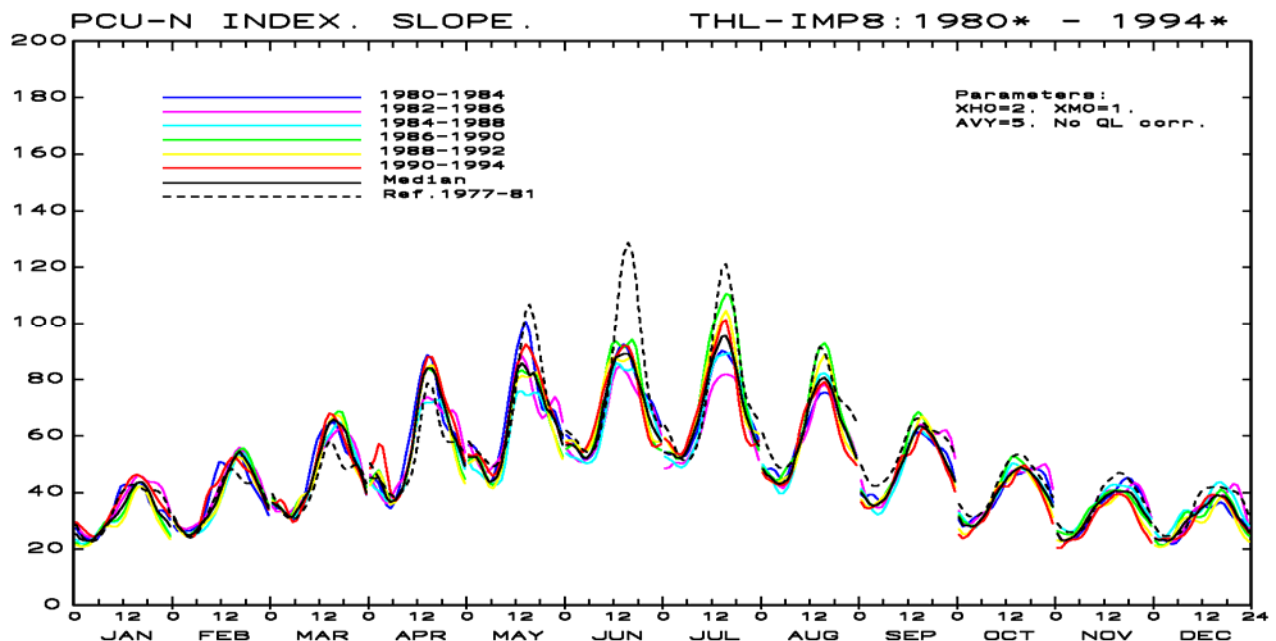


Figure 5.5. Calculation of slope for ΔF_{PROJ} against E_m without QL correction of Thule data. Averaging over 5 years. 2-D Gaussian smoothing use half-widths of 2 hours for time-of-day and 1 month for season, respectively.

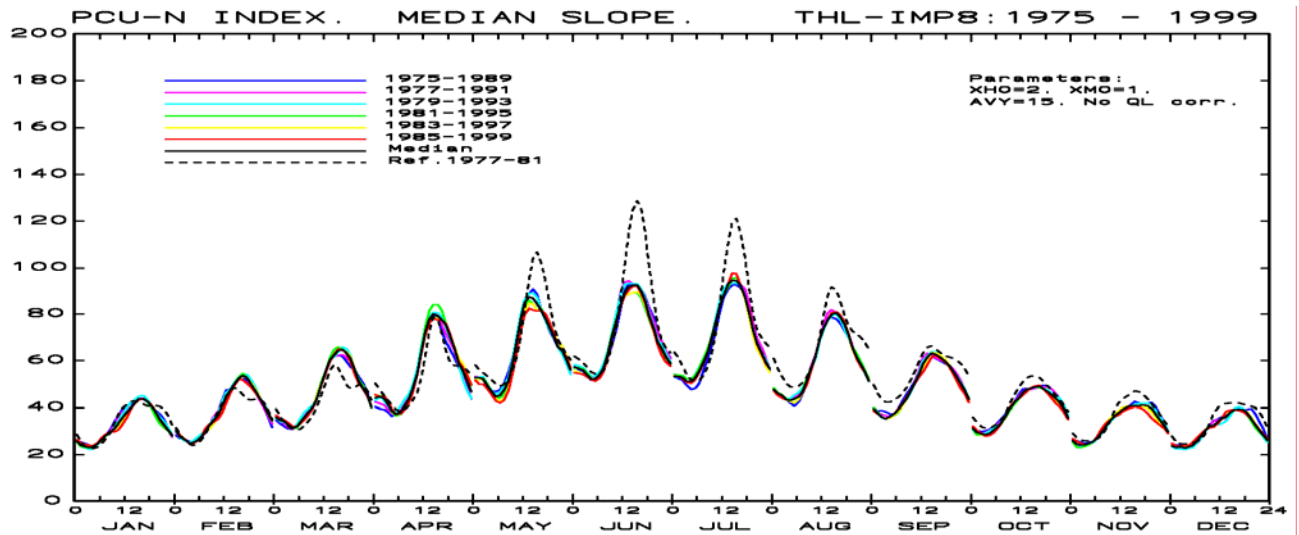


Figure 5.6. Plot of median values of slope. Each colour-coded trace represents the median over 15 years like depicted in Fig.5.5. Black trace is "grand median" slope over 25 years. Dashed curve from Vennerstrøm et al.

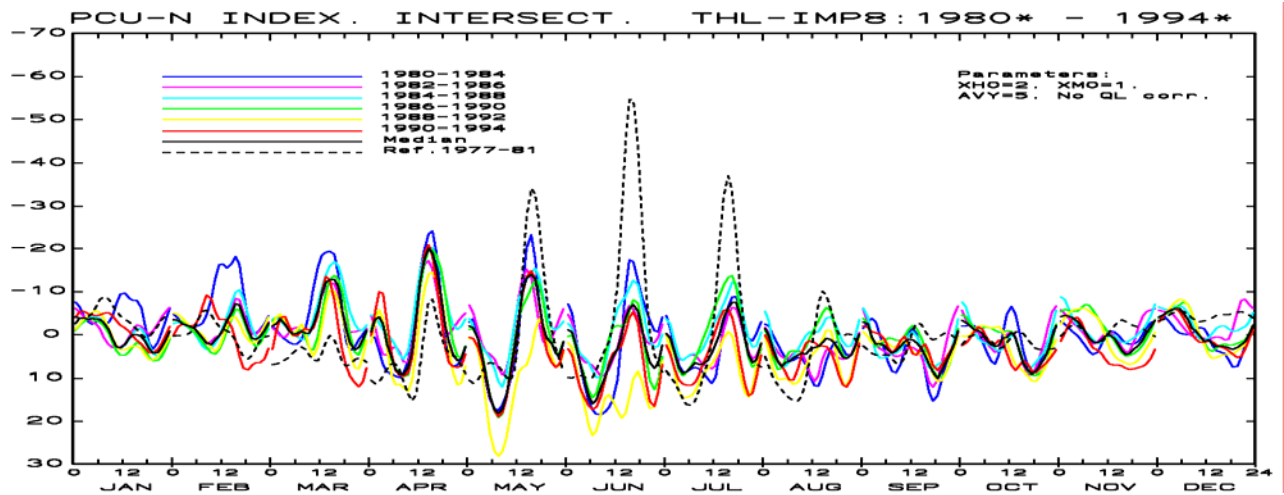


Figure 5.7. Calculation of intercept for ΔF_{PROJ} against E_m without QL correction of data. Averaging over 5 years. 2-D Gaussian smoothing use half-widths of 2 hours for time-of-day and 1 month for season, respectively.

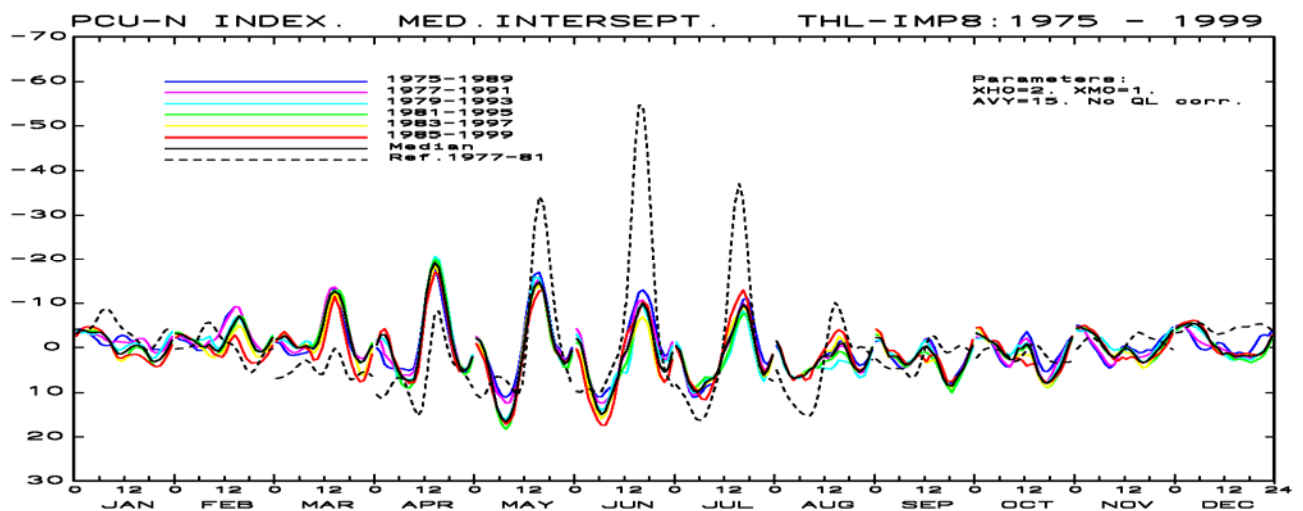


Figure 5.8. Plot of median values of intercept. Each colour-coded trace represents the median over 15 years like depicted in Fig.5.7. Black trace is "grand median" slope over 25 years. Dashed curve from Vennerstrøm.

Comparing Figs. 5.5-5.6 with Figs. 5.1-5.2 shows no large differences in the slope parameter. Comparing Figs. 5.7-5.8 with the corresponding Figs. 5.3-5.4 shows marked shifts in the intercept parameter. This is, predominantly, where the QL correction shows its effect. In Figs. 5.5-5.8 the corresponding values for slope and intercept as derived by Vennerstrøm et al., 1994, have been included. It is seen, particularly in Figs. 5.5 and 5.7, that the larger amplitudes of singular fluctuations are associated with the smaller extent of the data intervals considered in the individual cases.

Table 5.3. *PCN-U grand median slope. Thule-IMP8 data: 1975 - 1999 (No QL corr.)*

HR	JAN	FEB	MAR	APR	MAY	JUN	JUL	AUG	SEP	OCT	NOV	DEC
0	25.7	30.5	36.0	44.2	52.7	57.1	53.3	47.7	39.5	31.3	26.1	23.8
1	24.1	27.5	34.7	44.5	52.8	56.5	53.2	46.1	37.8	29.5	24.5	23.2
2	23.5	26.5	34.3	43.9	52.2	55.9	52.7	45.0	36.2	28.9	24.2	23.5
3	23.3	25.3	32.9	41.3	49.5	53.9	51.3	43.3	35.3	28.6	24.3	23.0
4	23.5	25.1	31.5	38.7	46.6	52.2	51.2	43.1	36.3	29.2	24.8	23.4
5	24.7	26.0	32.0	37.2	44.6	52.1	52.6	43.6	37.4	30.5	25.7	24.1
6	26.4	27.8	34.1	38.3	45.2	54.0	55.5	44.6	39.2	32.1	27.3	25.8
7	28.2	29.9	36.2	40.9	47.3	57.2	59.0	47.2	41.3	34.3	29.3	28.1
8	29.8	32.7	38.7	43.5	51.4	62.8	63.6	51.5	44.1	37.0	31.8	30.5
9	31.1	34.7	40.6	47.8	59.2	70.3	70.1	56.5	47.3	39.9	34.6	32.3
10	33.2	37.1	44.3	54.5	68.1	77.4	76.7	62.4	50.5	42.5	36.3	32.5
11	35.7	40.9	50.0	63.8	77.4	83.5	83.0	69.1	54.0	44.0	37.8	34.1
12	38.1	44.3	55.8	72.3	84.8	88.8	88.0	74.1	58.5	46.3	39.1	35.7
13	39.9	47.2	60.6	77.9	87.3	91.5	93.1	77.4	61.7	47.7	40.2	36.3
14	41.9	50.4	62.3	79.9	86.6	92.1	94.3	79.8	63.1	48.1	40.8	37.9
15	43.6	52.6	64.4	79.1	84.3	92.3	94.3	80.5	62.8	48.8	40.8	39.2
16	43.7	53.7	64.7	77.3	81.6	89.8	92.4	78.6	61.7	49.0	40.9	39.2
17	42.5	52.7	63.3	75.4	77.5	85.8	87.3	75.8	60.0	48.0	41.1	39.2
18	40.7	50.2	60.7	70.7	73.8	79.3	80.6	71.5	58.3	46.8	40.9	38.2
19	38.4	47.1	56.1	65.3	70.4	73.5	73.3	65.8	56.0	45.3	39.7	35.4
20	35.2	44.2	51.2	59.0	65.9	67.8	67.3	61.2	53.4	43.8	37.5	32.6
21	32.7	41.2	48.0	55.8	64.0	65.2	63.1	58.4	50.5	42.0	35.1	30.4
22	30.5	38.2	45.5	51.9	60.3	61.9	59.5	55.2	47.3	39.4	32.6	28.5
23	28.1	34.7	40.2	46.7	56.0	58.8	56.5	51.4	43.5	35.8	29.8	26.3

Table 5.4. *PCN-U grand median intercept. Thule-IMP8 data: 1975 - 1999 (No QL corr.)*

HR	JAN	FEB	MAR	APR	MAY	JUN	JUL	AUG	SEP	OCT	NOV	DEC
0	-3.2	-3.1	-1.8	-0.6	-2.0	-2.0	-0.3	-1.4	-2.3	-3.2	-4.3	-4.3
1	-3.9	-3.0	-2.0	-2.8	-1.5	-1.0	0.9	0.8	-2.2	-2.8	-4.6	-4.9
2	-3.8	-2.5	-2.7	-2.9	1.2	2.7	5.1	3.8	-0.2	-2.3	-4.2	-5.2
3	-3.4	-2.0	-1.8	-1.4	4.8	7.1	8.1	6.1	2.1	-1.5	-3.8	-5.4
4	-3.3	-1.7	-0.6	2.2	9.3	10.8	9.6	7.0	2.0	-1.1	-3.1	-5.4
5	-3.5	-0.9	0.1	5.0	13.4	13.6	10.0	6.8	2.0	-0.4	-2.3	-5.2
6	-3.5	-0.2	-0.1	6.4	15.8	14.9	9.3	6.6	3.2	0.9	-0.9	-4.4
7	-2.7	-0.1	-0.5	7.2	16.6	14.3	7.8	6.1	4.0	2.1	0.4	-3.1
8	-1.3	-0.7	0.1	7.6	15.7	11.3	7.3	5.0	3.6	2.8	1.6	-1.5
9	0.3	0.4	0.2	7.3	13.2	9.1	7.0	4.4	2.5	2.6	2.3	-0.5
10	1.5	0.9	-1.0	3.3	8.2	6.6	5.1	3.1	1.3	0.3	1.5	0.2
11	1.4	-0.2	-4.7	-4.3	1.8	2.2	1.8	2.1	0.1	0.3	0.6	1.5
12	0.8	-1.9	-8.9	-11.9	-4.8	0.6	-0.5	2.0	-0.3	-0.8	0.3	1.2
13	0.0	-3.8	-12.0	-17.4	-10.6	-2.1	-2.2	2.0	0.8	0.3	0.6	1.5
14	-0.5	-5.8	-12.6	-19.2	-13.7	-5.7	-4.6	0.8	1.9	3.2	1.9	2.1
15	-0.4	-7.1	-12.0	-17.9	-14.8	-8.6	-8.1	-0.7	4.1	6.1	2.9	2.0
16	0.1	-6.1	-9.4	-13.5	-12.9	-10.0	-9.6	-1.0	6.9	7.8	3.5	1.9
17	1.5	-3.8	-5.2	-7.6	-8.7	-8.1	-8.7	1.0	8.5	8.1	3.0	1.9
18	3.0	-1.2	-1.1	-2.2	-3.5	-4.3	-5.1	3.6	8.8	7.3	2.1	2.0
19	3.3	0.6	2.1	1.6	0.3	0.3	0.3	4.9	7.3	6.1	1.0	1.9
20	2.6	0.9	3.4	4.3	2.0	4.0	4.3	5.5	5.9	4.6	0.2	1.5
21	1.7	0.9	3.0	5.2	3.6	5.5	6.1	4.7	4.5	2.3	-1.2	0.9
22	0.2	-0.6	1.3	4.5	3.2	4.8	4.9	2.8	1.7	-0.4	-2.6	-0.7
23	-1.6	-2.2	-0.4	2.1	0.6	1.1	1.8	-0.1	-0.4	-2.3	-3.9	-2.6

6. Calculation of Polar Cap index

For the Polar Cap (PC) index to become a proxy for the merging electric field we define index values from equivalence with Em in Eq. 5.1. ($\Delta F_{PROJ} - \Delta F_I = S \cdot Em$), i.e.:

$$PC = (\Delta F_{PROJ} - \Delta F_I) / S \quad (6.1)$$

where S , the "Slope", and ΔF_I , the "Intercept" parameter, named from a visualized graphical display of ΔF_{PROJ} against Em , were found from regression analysis of polar observatory and interplanetary satellite data and now provided in tabular form (Tables 5.1 and 5.2)

From above outlined steps to link the polar magnetic variations to the interplanetary magnetic field, the horizontal magnetic vector is first resolved in an X-component (northward in a geographical coordinate system) and a Y-component (eastward). From the raw data the base values are subtracted and the QL values (defined from minimum variance analyses) are subtracted, i.e.:

$$\Delta X = (X_{RAW} - X_0) - X_{QL} \quad (6.2a)$$

$$\Delta Y = (Y_{RAW} - Y_0) - Y_{QL} \quad (6.2b)$$

here, X_0 is the base value for the X-component defined yearly (every 1 January) and now adjusted to the actual day-of-year. X_{QL} is the reference QL level provided as a table of hourly values each day of the year and now adjusted to the proper time-of-day. The Y-component is handled correspondingly.

The projection of the disturbance vector ΔF to the optimum direction is calculated from:

$$\Delta F_{PROJ} = \Delta X \cdot \sin(V_{PROJ}) - \Delta Y \cdot \cos(V_{PROJ}) \quad (6.3)$$

where V_{PROJ} is derived as a function of $UThr$ (UT time in hours) through:

$$V_{PROJ} = Longitude + UThr \cdot 15^\circ + ODA \quad (6.4)$$

Here, values of the *optimum direction angle*, ODA , were calculated to provide the optimum correlation between ΔF and the merging electric field, Em . ODA values are provided in tabular form (Table 4.2.) as hourly values at mid-month and must be interpolated.

Summarising, the parameters needed to derive PCN index values from Thule observatory data are:

1. "Quiet Level" for X and Y components.
2. Optimum Direction angle (angle between sun direction and transpolar equivalent current).
3. Slope and Intercept.

6.1. Quiet Level (QL) parameters.

In this presentation the QL parameters are derived for the X- and Y- components of the geomagnetic recordings. The QL values for Thule Observatory are calculated from the recorded data as weighted average values like the examples shown in Figs. 3.1. or 3.2. for the X-component (top) and Y-component (bottom). Here we present these QL data for one year in Fig. 6.1. Each diagram is divided along the horizontal axis into 12 separate fields for each month of the year. Within each field there is a time scale spanning 00 – 24 hours UT. Tables of hourly values of the QL for the X- and Y-components have been calculated for each day of the year. Parabolic interpolation using the actual hour and the preceding and following hourly values is used to derive QL values with finer resolution. The diagrams display 5-min samples (in UT-time) of QL for the X-component (top) and Y-component (bottom) calculated for each day of each month of the year in question (here year 2000).

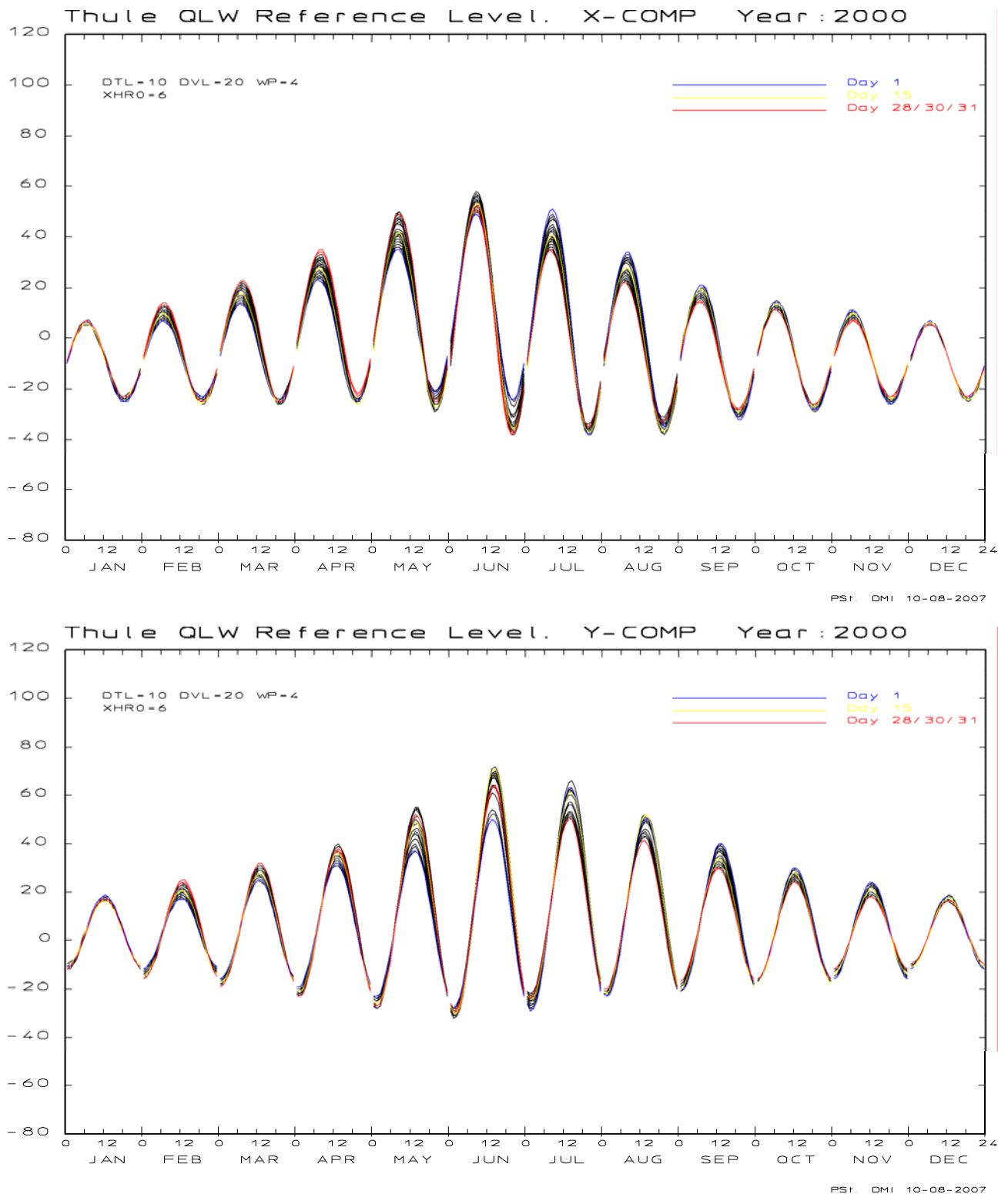


Figure 6.1. Diagrams to present 5-min samples of QL values for each day of each month of the year.

The yellow traces in the diagrams in Fig. 6.1 present the mid-month values. These traces are just smooth versions (5-min samples) of the hourly value traces shown in Fig. 1 for the month and year in question. The blue and the red traces display the values on the first and the last day of the month, respectively. Hence the red trace in one month is very like the blue trace in the following month since they represent data from successive days. The traces for the remaining days in the month are drawn with black line.

In addition to presenting the general variations in the QL values with time of day and season (month of year) the diagrams in Fig. 6.1. also provide impressions of the variability in the QL values through any month.

The QL values like the examples displayed in Figs. 3.1-3.4, the grand median optimum direction angle values displayed in Figs. 4.4. and listed in Table 4.1., the slope grand median values displayed in Fig. 5.3. and listed in Table 5.1., and the grand median intercept values displayed in Fig. 5.4. and listed in Table 5.2. are considered "consolidated" parameters to be used for calculation of unified PCN index values at DMI based on Thule magnetic data and using Eqs. 6.1, 6.2a, 6.2b, 6.3 and 6.4.

The parameters are generally defined in tables of hourly values referring to the middle of the month and these values must be interpolated to match the samples of magnetic data used to calculate PC index values of the desired resolution, for instance, 1-min or 5-min PC index values.

6.4. Examples of PC index calculations.

Examples of the results of such calculations of the PC index are displayed in Figs. 6.5-6.7 for the first half of 1999. Each diagram is divided along the vertical axis into 16 fields spanning one day (00-24 hours) each. Within each field we have in green line plotted the PCN values calculated earlier at DMI (PCN-DMI(old)) and in blue line the PCN values calculated by the unified procedure (PCNU-DMI) using Thule magnetic data which are continuously available. Both indices are plotted on a scale of 5 unit/division (i.e., a total field width of 10 units).

Further in magenta line is plotted the merging electric field E_m^* (referred to polar cap) on a scale of 5 [mV/m]/div (i.e., a total field width of 10 mV/m) in order to enable a direct comparison with the PC index values. One should note that the satellite data (here IMP 8 data) are not continuously available.

For all data types the diagrams in Figs. 6.5. - 6.8. display 5-min average values.

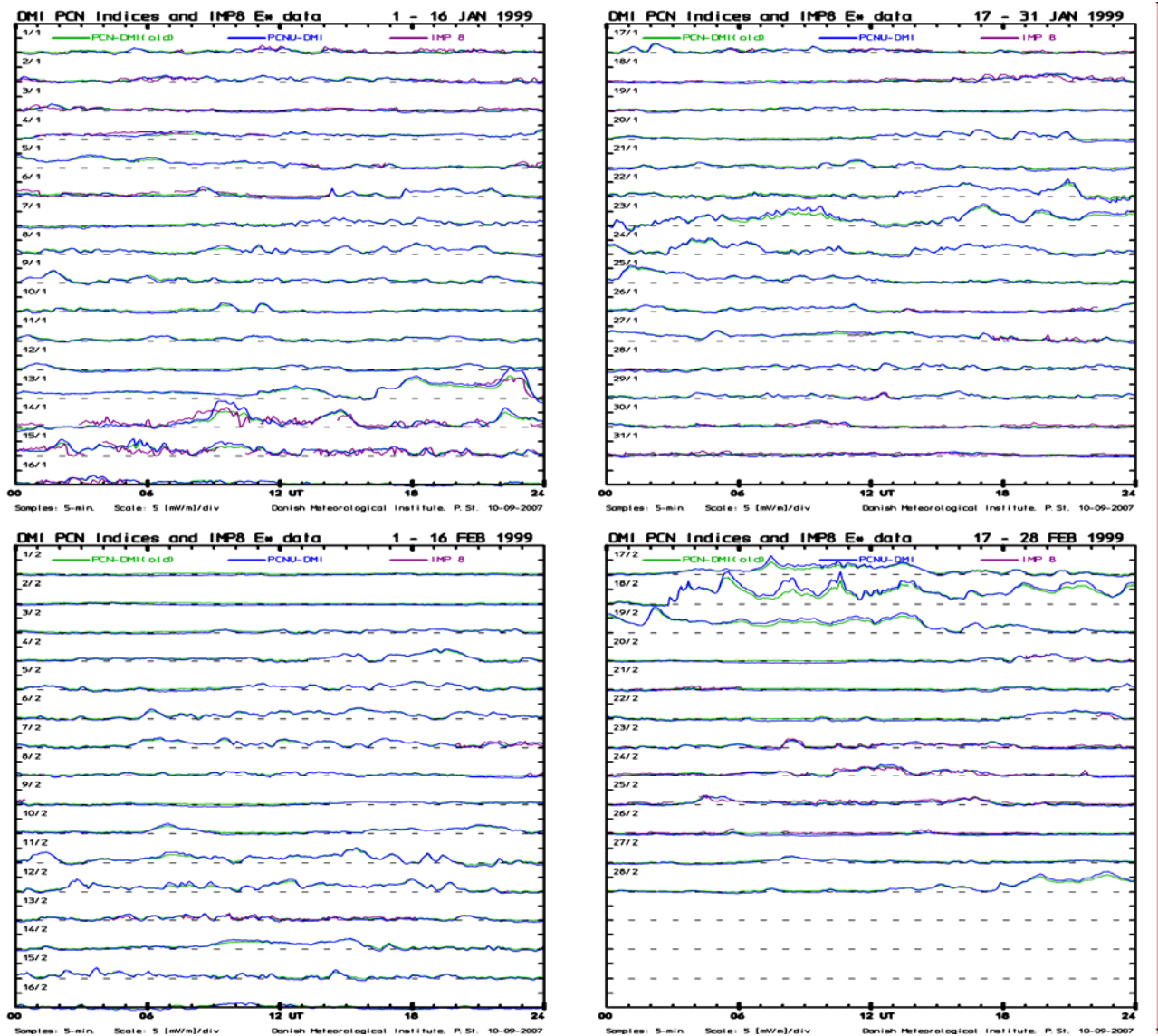


Figure 6.5. PCN-DMI(old) and PCNU-DMI indices, and IMP8 merging electric field. 1.1-28.2.1999.

In Fig. 6.5 the two sets of PCN index values are present all the time. The PCNU-DMI (blue line) index values were drawn on top of and will hide the PCN-DMI(old) (green line) values when the two sets have equal values. The merging electric field data (magenta line) are plotted only when IMP 8 supplies valid data and the satellite is upstream the bow shock. Hence the data coverage is rather intermittent. The data interval represents a typical winter season during moderate solar activity. One may note that for small to moderate levels the two PCN index series show minor differences only. For the large values the PCNU values are markedly larger than the PCN-DMI(old) values. There is quite good agreement between the PCNU values and the corresponding merging electric field values.

Further PCN and Em^* (IMP 8) example calculations are presented in Fig. 6.6. for a typical equinox interval (1.3 - 30.4 1999) and again for moderate solar activity.

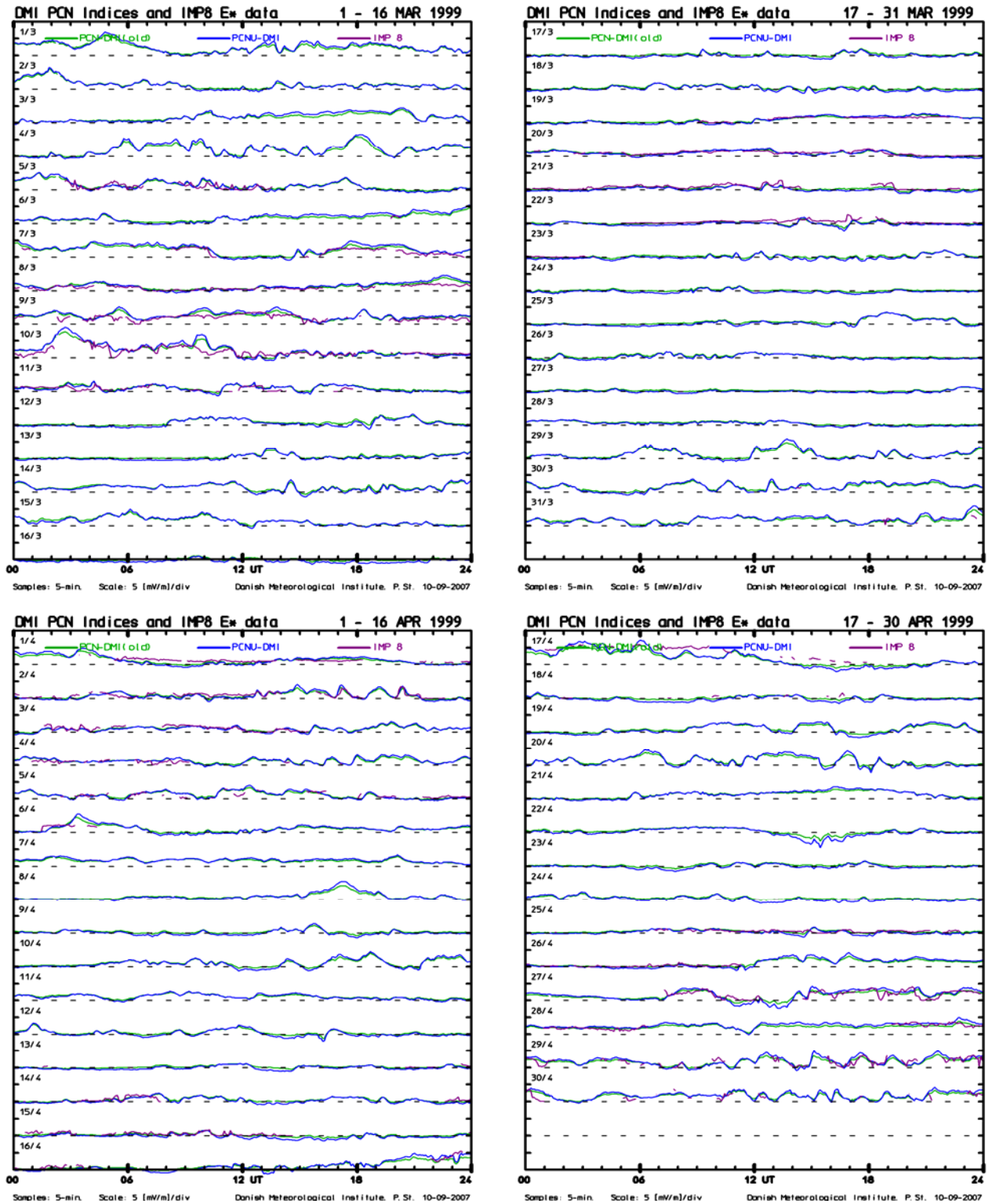


Figure 6.6. PCN-DMI(old) and PCNU-DMI indices, and IMP8 merging electric field. 1.3-30.4.1999.

Again, at small and moderate levels the two sets of PCN index values, PCN-DMI(old) and PCNU-DMI show only small differences whereas for enhanced levels the PCNU values exceed the PCN-DMI(old) values. Both index series agree well with the (moderate) merging electric field values presented in the diagram. The data coverage by the IMP 8 satellite, unfortunately, is rather sparse. Like in the data for the winter season displayed in Fig. 6.5. only a few cases of negative PCN index values are seen in the display in Fig. 6.6 for an equinox interval. For the negative excursions the PCNU values reach much larger amplitudes than the PCN-DMI(old) index values.

The PCN - Em* (IMP 8) example presentation is continued in the series of data for a summer interval (1.5 - 30.6 1999) shown in Fig. 6.7. Again, the solar activity is moderately high.

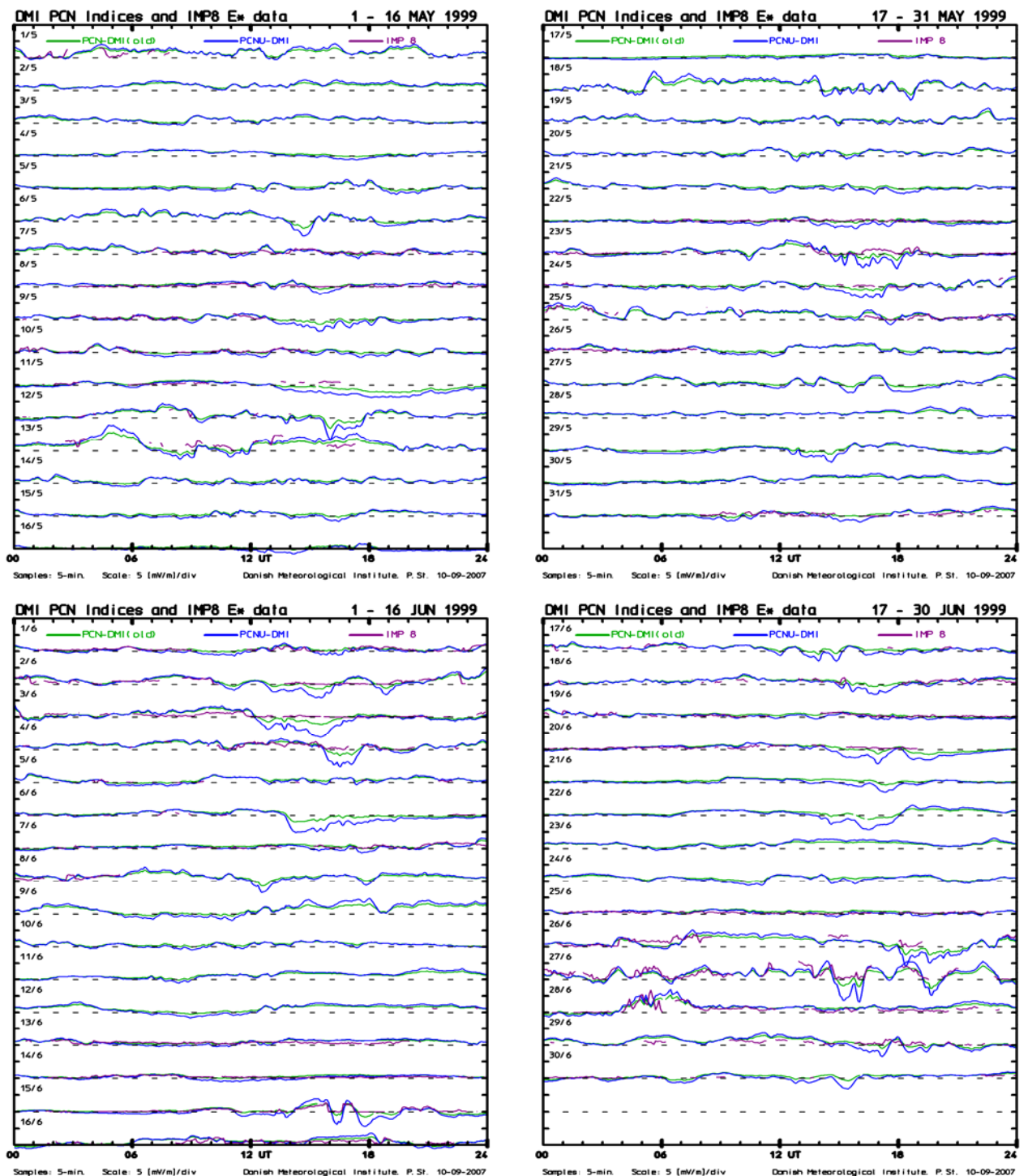


Figure 6.7. PCN-DMI(old) and PCNU-DMI indices, and IMP 8 merging electric field. 1.5-30.6 1999.

For the summer interval presented in Fig. 6.7, one may note the frequent occurrence of negative PC index values, which is a usual feature for this season. Further, one may note the close agreement between PCN-DMI(old) and PCNU-DMI index values, when they are low to moderate and positive. The differences are more substantial when the two PC indices take negative values. For these cases the PCNU-DMI index values are usually more negative (numerically larger) than the PCN-DMI(old) index values. This is an effect related to the different procedures for calculation of index values (the QL correction issue).

For comparison we further include in Fig. 6.8 an example of PCN - PCNU - E_m^* comparison where the merging electric field is now calculated from ACE satellite data measured at the L1 position. The satellite position is at around 240 Re in front of the Earth causing a delay of around 1.0 - 1.5 hr between the merging electric field measured at the satellite and the related effect at the Earth. This could be contrasted to the IMP 8 orbit at around 30-35 Re distance and the corresponding delay from the satellite to the polar cap ionosphere of just around 15-25 min.

On that basis one would expect larger disagreements in the timing of PCN index values and related time-shifted E_m^* values for ACE as compared to IMP 8 cases. An inspection of the traces in Fig. 6.8 and many similar diagrams confirms the greater spread in the relative timing of PCN variations versus ACE E_m^* changes.

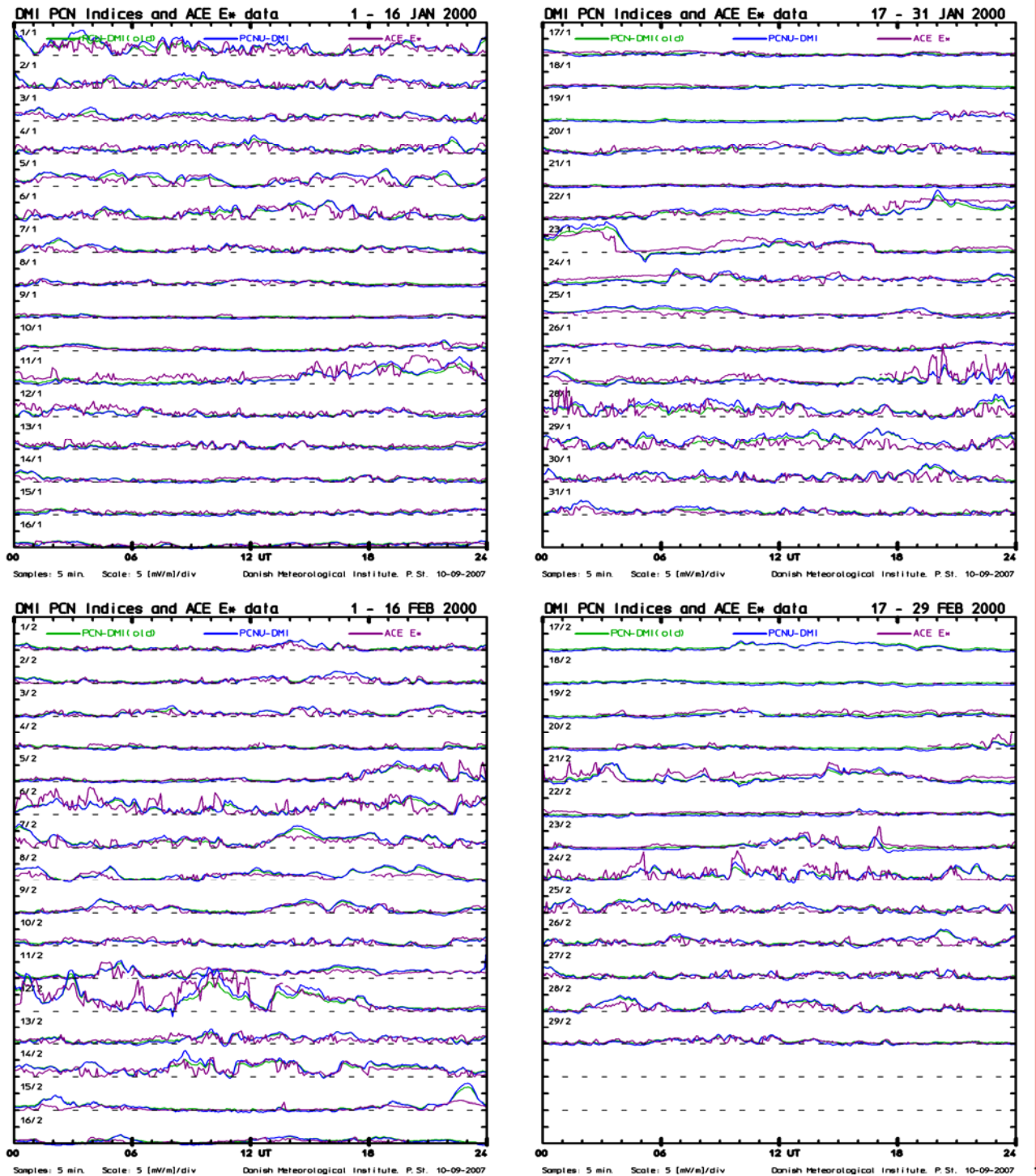


Figure 6.8. PCN-DMI(old) and PCNU-DMI indices, and shifted ACE merging electric field. 1.1-29.2 2000.

7. Quality of PCN index values.

The quality of the PCN index values derived by the different calculation procedures are examined in order to evaluate the following quality issues:

1. Correct calculation of delay from satellite observations to related polar cap effects.
2. Close overall correlation with satellite observations of “Merging Electric field” (MEF).
3. Agreement between amplitude spectra for PCN and MEF (except negative values of PCN).
3. Close agreement between UT variations of PCN and MEF through seasons and years.
4. Close agreement between yearly averages of PCN index values and MEF.

7.1. Control of delay from satellite to polar cap

In the calculations of parameters for deriving the polar cap index from ground magnetic observations we have imposed a delay from satellite observations of the merging electric field, *MEF*, (i.e. observations of solar wind velocity and interplanetary magnetic field) to related polar cap magnetic variations (i.e. ionospheric currents). The delay is composed of two contributions. One is the progression of solar wind effects with the solar wind velocity from the satellite position to a reference position located 12 Re in front of the Earth. The reference position is supposed to represent a location just outside the magnetosheath, i.e., just upstream the bow shock. The other is a fixed amount of 20 min to deal with the propagation of *MEF* effects through the magnetosheath, into the magnetosphere and along the field lines to reach the polar ionosphere and, furthermore, the reaction time for the transpolar Hall currents (i.e., the polar ionospheric convection) to adjust to a changing drive.

In order to evaluate the validity of the fixed 20 min delay we have compared PCN values with relevant MEF values in series of correlation scatter plots where the delay is given different values. We have conducted this analysis for each year from 1975 to 2003 using IMP 8 data to derive MEF values during 1975-1999 and ACE data during 1998-2003.

The correlation scatter plots in Fig. 7.1. presents the results for the year 1998. Each diagram has a horizontal scale for the *MEF* derived from IMP 8 measurements of solar wind velocity and interplanetary magnetic field. The values calculated at the satellite position have first been shifted with solar wind speed to the 12 Re reference position and then delayed by amounts of 10, 15, 20 or 25 min with respect to the PCN index values representing polar cap magnetic variations. The vertical axis has a scale for the calculated PCN index. The diagonal dashed line drawn in red would indicate complete agreement between *MEF* and PCN. Based on 5-min samples the individual points are scattered around this line in the diagram.

Recalling that the large negative values of the PCN index represent reverse convection, which is not related in any simple way to the *MEF* values, we have in the statistics discarded points with PCN values less than -0.2. They represent intervals of indeterminate Em-PCN relations. In the lower part of each diagram the number of 5-min samples of PCN above and below -0.2, respectively, are noted.

For points with PCN above the limit of -0.2 we have calculated the mean difference between the PCN and the MEF values (the vertical distance from the point to the diagonal). The average difference is denoted S0 in the diagram. Correspondingly, the average numerical (robust) difference is denoted S1 and the average root-mean-square (RMS) difference is denoted S2. These parameters are also listed in the lower part of each diagram. For best quality these three parameters should be at minimum.

Comparing the listed values of S0, S1 and S2 for the 4 cases shows that a delay of 20 min gives the best result (i.e. lowest scatter). The differences in scatter parameters, however, are not large since the relatively small variations in the delay are important only for cases with large variations in the interplanetary or polar cap parameters on the same time scale as the step in delay times (i.e. few minutes). Furthermore, there is an inherent variation in the actual delay times with varying solar wind and magnetospheric conditions (e.g., at compressed versus inflated magnetosphere).

Fig. 7.2. presents the corresponding case for 1999 using here ACE data to calculate MEF instead of using IMP 8. The result with respect to optimum delay is the same, hence the optimum value is again 20 min.

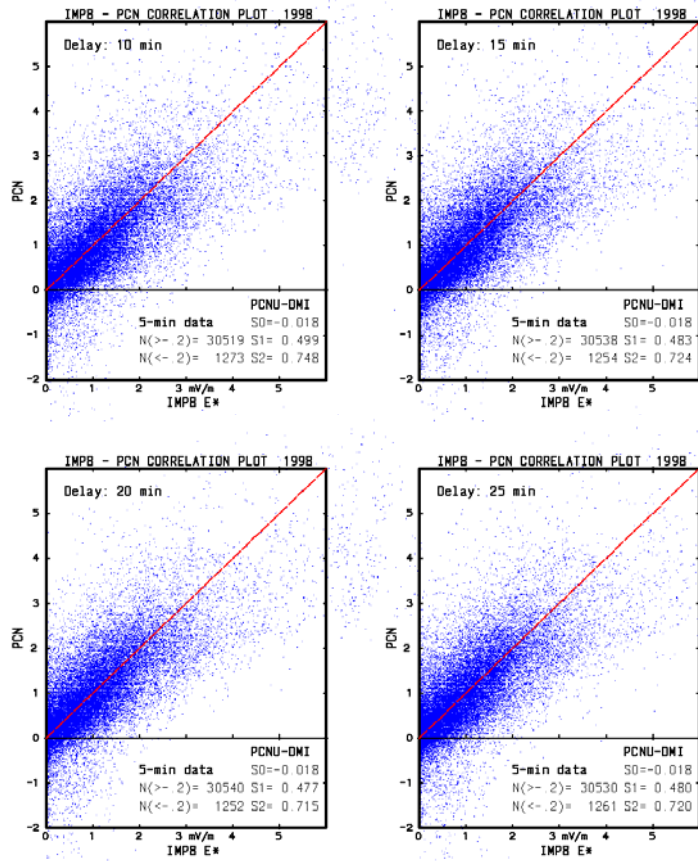


Figure 7.1. Scatter plots of 5-min samples of PCN values versus IMP 8 merging electric field.

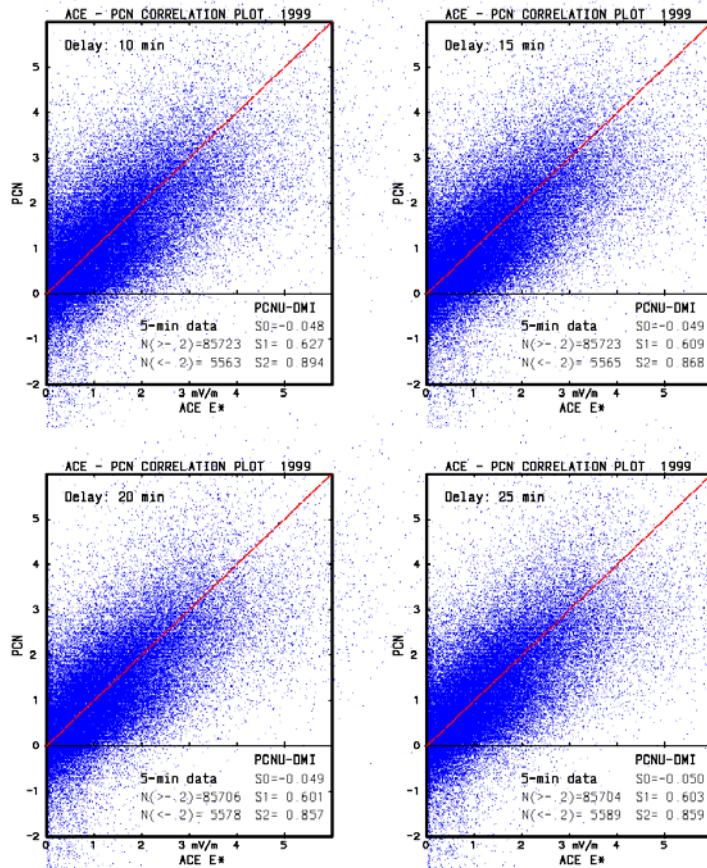


Figure 7.2. Scatter plots of 5-min samples of PCN values versus ACE merging electric field.

7.2. Overall correlation with merging electric field.

In order to evaluate the quality of the PCN index derived from the different sources we have compared PCN values with relevant values of the Merging Electric Field (MEF) using correlation scatter plots like those in Figs. 7.1. and 7.2. Fig. 7.3 presents the results for the years 1999-2003. The merging electric field values used in the correlation plots are based on using ACE data. The PCN values in the left series of diagrams are calculated using the earlier DMI procedure without QL correction of the polar magnetic field observations. The PCN values displayed in the right series of diagram are calculated with the new unified procedure using QL correction of the magnetic data.

The diagrams display 5-min samples in all cases. In order to distinguish between positive PCN values assumed to be related to the merging electric field and negative PCN values not related in a simple way to the MEF we have again defined a limit of -0.2 for the index values. The number of points above and below this limit is noted at the bottom of each diagram. Furthermore, the average deviation, S0, the average numerical (robust) deviation, S1, and the RMS deviation, S2, have been calculated. The results are also noted at the bottom of each diagram. For best result the scatter parameters should all be small and the number of negative PC values should not be too high.

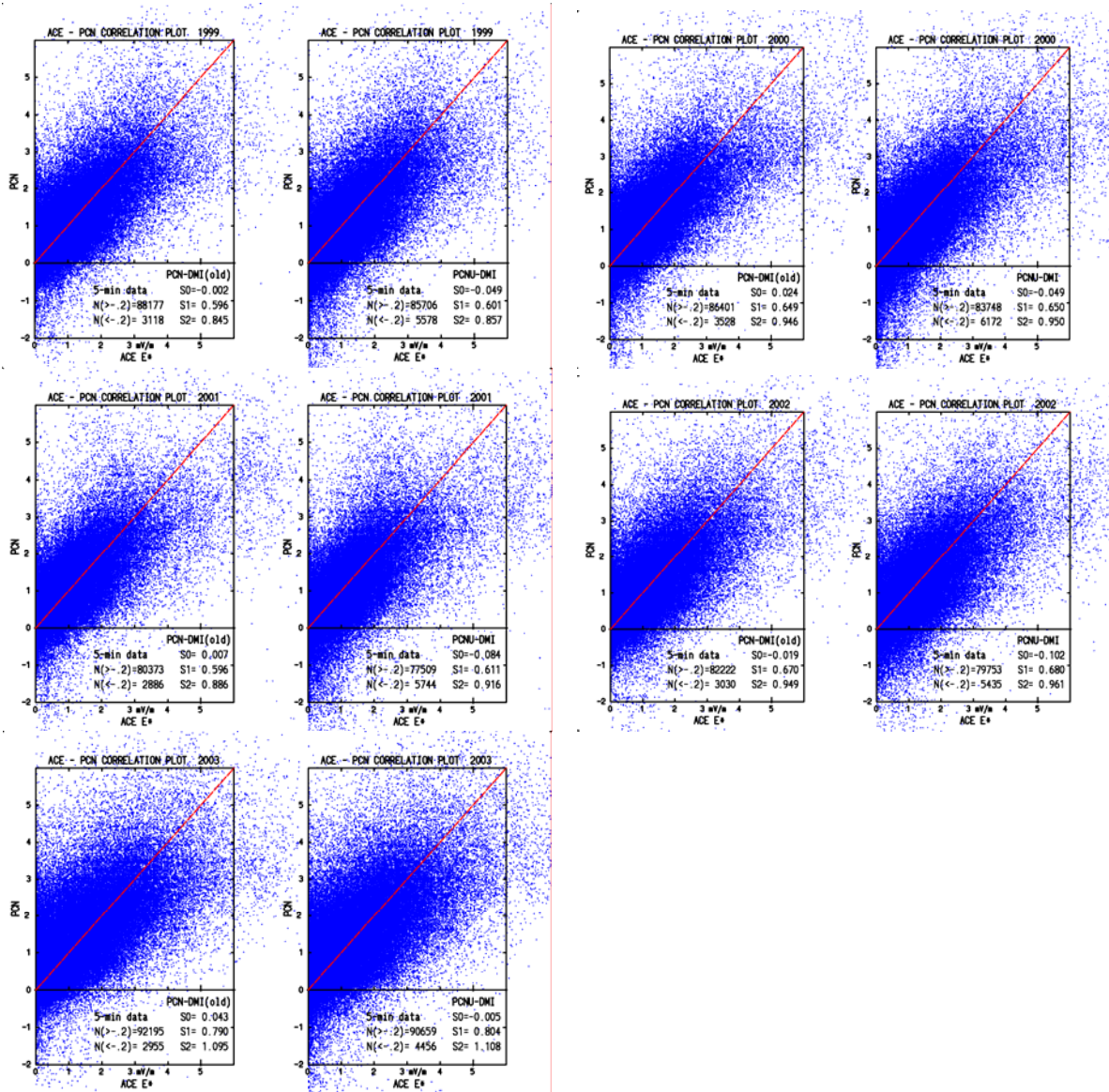


Figure 7.3. Scatter plots of 5-min samples of PCN values versus ACE merging electric field.

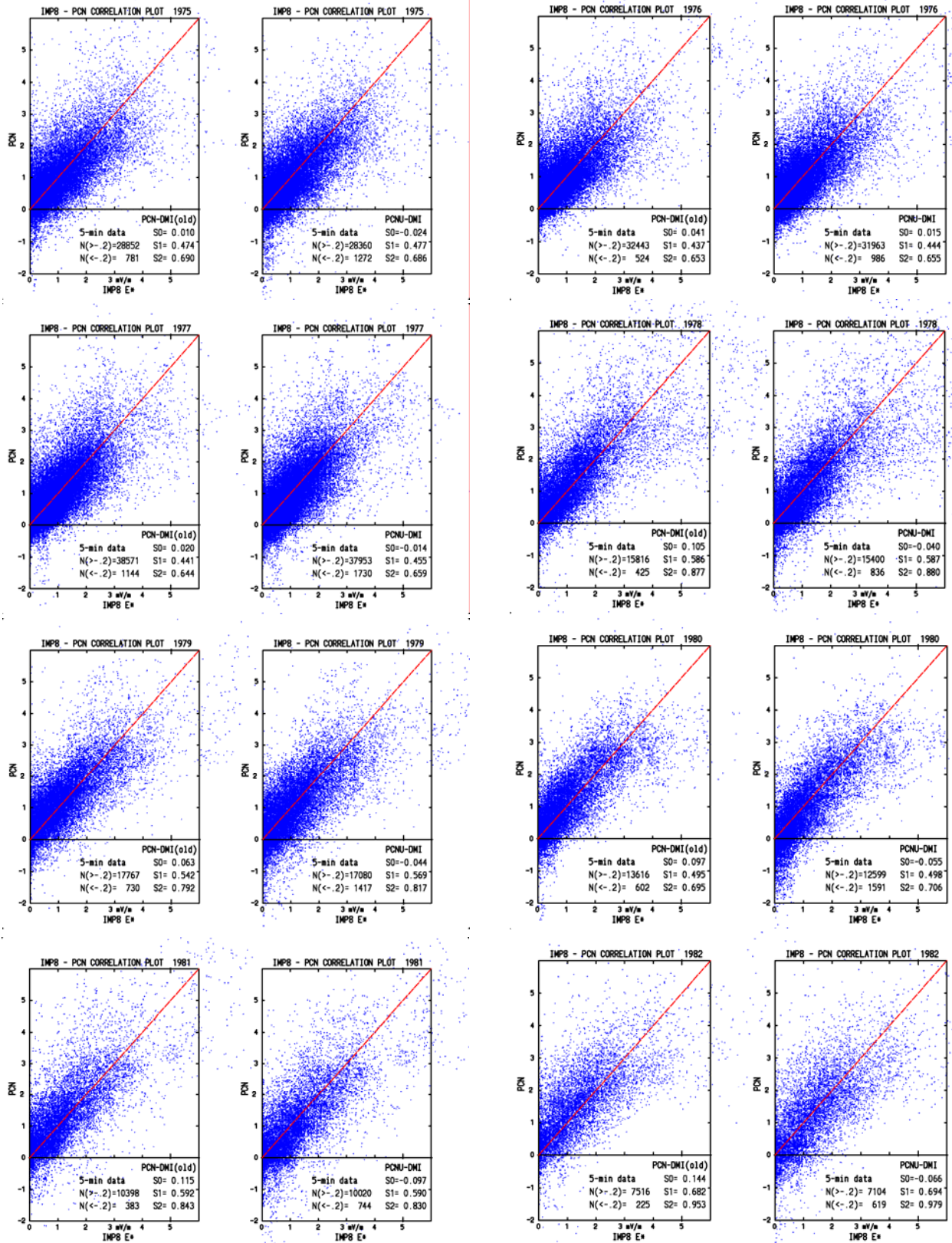


Figure 7.4. Scatter plots of 5-min samples of PCN values versus IMP8 merging electric field 1975-82

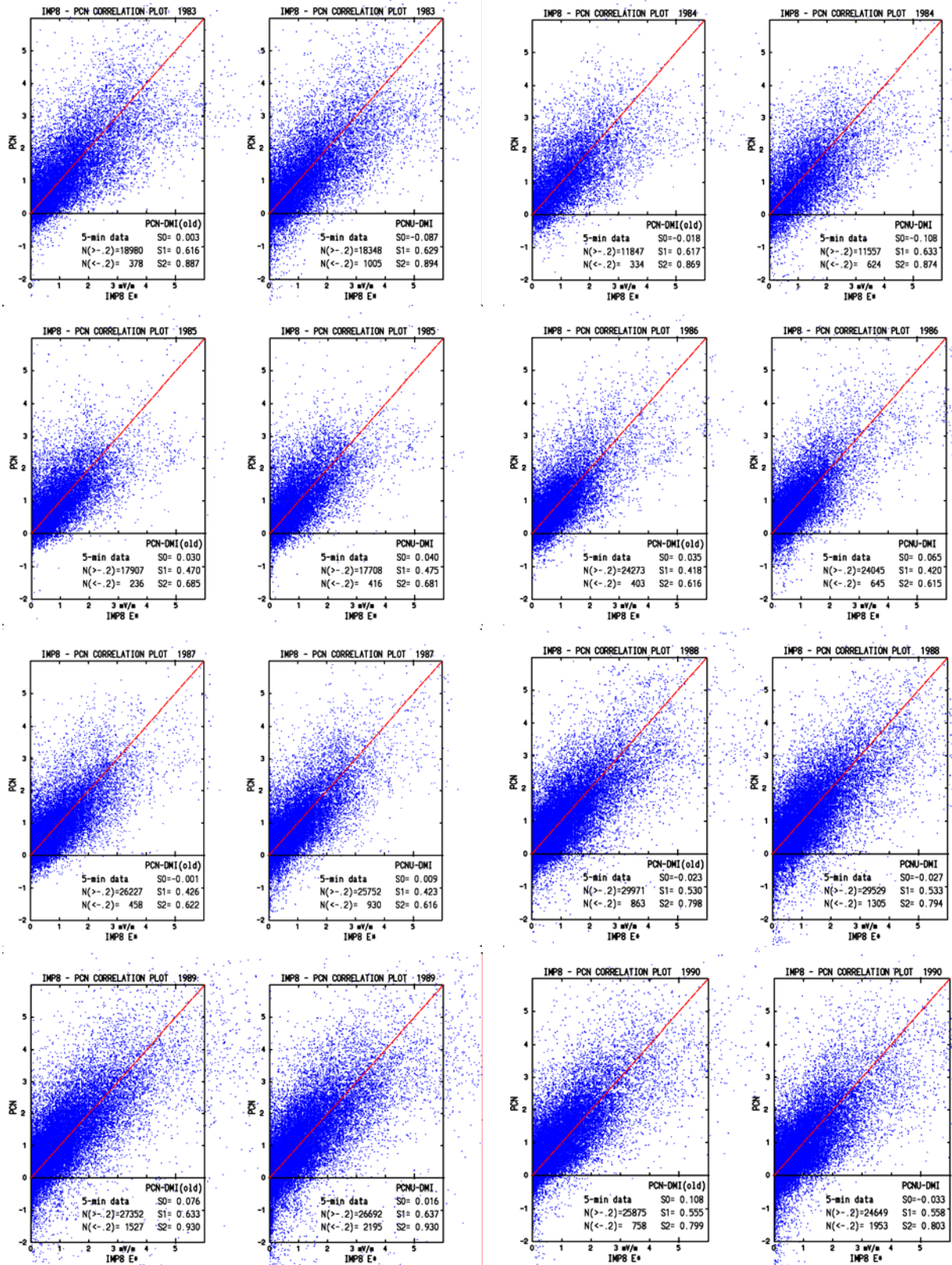


Figure 7.5. Scatter plots of 5-min samples of PCN values versus IMP8 merging electric field 1983-90

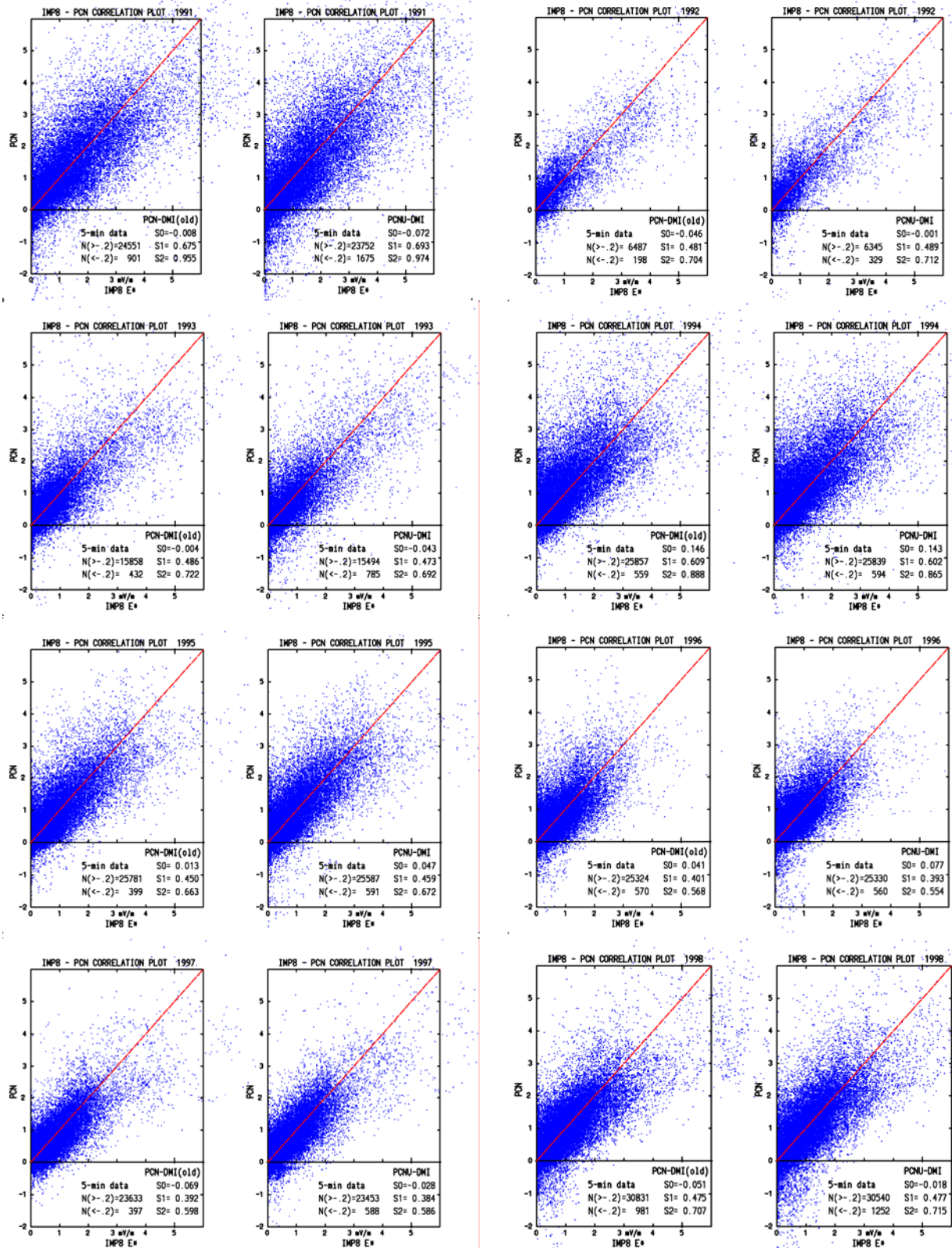


Figure 7.6. Scatter plots of 5-min samples of PCN values versus IMP8 merging electric field 1991-98

From the series of plots displayed in Figs. 7.3-7.6 we may note several features. The values of the scatter parameters (S_0 , S_1 , S_2) for PCN-DMI(old) and PCNU-DMI are very close in all corresponding cases (i.e. same year). In some cases one set provides the best (smallest) scatter parameters. In other cases the other set leads.

There are large differences in the number of data points in the different years. In normal (leap) years the total number of 5-min intervals is 105,120 (105,408). During the IMP 8 epoch (1975-1998) the amount of available data is very sparse in some years, down to a low of only 6700 samples in 1992, and up to 40,000 samples in 1977 corresponding to valid satellite data during 1/3 of total time. During the ACE epoch (1999-2003) the amount of available data is more than 80,000 samples reaching a high of 95,000 samples in 2003 corresponding to valid satellite data during 90% of total time.

The amount of samples of large negative values of the PC index (<-0.2) is around 3% for the PCN-DMI(old) index and around 5% for the PCNU-DMI index. Recalling that the large negative values of the PCN index represent reverse convection, which is not related in any simple way to the MEF values, we have in the statistics discarded points with PCN values less than -0.2 . They represent intervals of indeterminate Em-PCN relations.

The cases of reverse convection are usually related to large intensity positive (northward) IMF Bz values (NBZ conditions). Such events are usually accompanied by strong field-aligned current (FAC) systems in the central polar cap. These NBZ FAC currents are oppositely directed compared to the usual Region 1 FAC system. Hence the ionospheric electric field and the convection direction in the central polar cap are reversed. For the reverse convection to develop during NBZ conditions a rather high ionospheric conductivity in the central polar cap seems mandatory. Accordingly, these cases have a preferred occurrence during local summer (cf. Figs. 6.5-6.7).

For calculations of the PC index the QL correction corresponds to using as baseline the magnetic variations relating to a low-intensity sunward transpolar Hall current equivalent to a weak antisunward convection across the polar cap. This convection could be seen as part of the two-cell polar convection driven by solar wind-magnetosphere "friction" (Axford and Hines, 1965), which will prevail during intervals of zero or very small IMF intensities. Hence cases, where the convection is weaker than usual or takes a different direction such that the projected value is smaller than corresponding to the QL level, may give negative PC index values. Furthermore, when the convection is really reversed then the difference up to the usual forward level will be greater than just the negative excursion. Hence the negative PC index values will be numerically larger when using calculation procedures with QL correction than they would be without QL correction.

7.3. Amplitude spectra for PCN index and for MEF values.

As part of the verification of the attempt to equalize in a statistical sense the Polar Cap (PC) index and the interplanetary merging electric field (MEF) we have derived the amplitude distribution of 5-min samples of the PCN index series and MEF values. For each year we have calculated the number of 5-min samples of PCN index values and MEF values (measured in mV/m) in bins of 1 integer unit (i.e. ..., -1.0 to 0.0 , 0.0 to 1.0 , 1.0 to 2.0 ... etc.). It was required that both PCN and MEF values were valid for the samples to be counted in.

Examples of the calculation of amplitude spectra are presented in Figs. 7.7. and 7.8. for year 2000 and 2003, respectively. The horizontal axis is divided in unit intervals from -5 to $+10$. The vertical scale depicts the number of samples. The total possible number of samples for normal (leap) years is 105,120 (105,408). The points for the number of cases within each bin are connected by lines (for guidance only). The amplitude statistics for the PCN values derived by the new unified procedure is marked by the blue line. The PCN values derived by the old DMI procedure are marked by the green line while the statistics for the merging electric field (MEF) derived from ACE satellite data is marked by the red line.

It should be remembered that the MEF by definition is always positive while the PC index may take positive values corresponding to normal convection as well as negative values corresponding to reverse convection cases. The reverse convection conditions predominantly occur when the interplanetary magnetic field is northward (NBZ conditions). Such conditions, in turn, generates only small MEF values. Hence the first bin of MEF values, from 0.0 to 1.0 , holds MEF samples that both relate to numerically small values of the

interplanetary magnetic field, IMF, (and small solar wind velocities) and to quite large intensities of the IMF in northward direction. Accordingly, the number of MEF cases in this bin relate to small positive PCN values as well as all negative PCN cases.

For the remaining positive bins the number of PCN 5-min samples shall be equal to the number of MEF samples in the ideal case. By comparing the blue and the red traces it is seen that this condition is well met for the samples of the new PCN (unified) index. It is also reasonably well met for the samples of the old PCN-DMI index illustrated by the green trace. The amplitude distributions for other years present largely the same picture. In a few of the years 1975-2003 the amplitude spectrum of the old PCN-DMI index provides the better fit to the amplitude spectrum of the MEF samples.

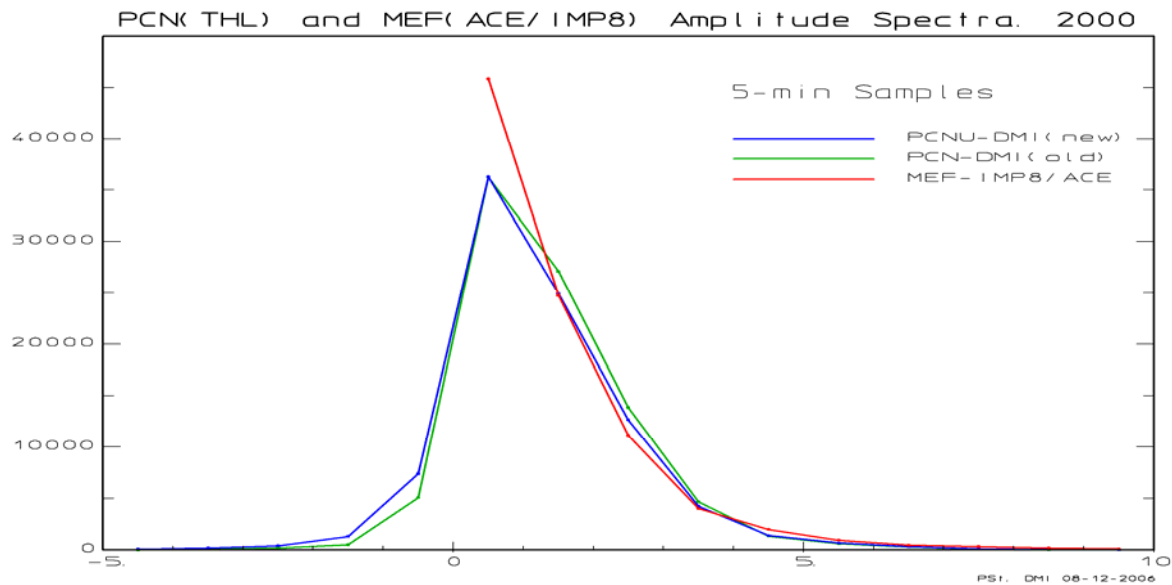


Figure 7.7. Amplitude spectra for PCNU (new), PCN (old) and MEF 5-min samples in year 2000.

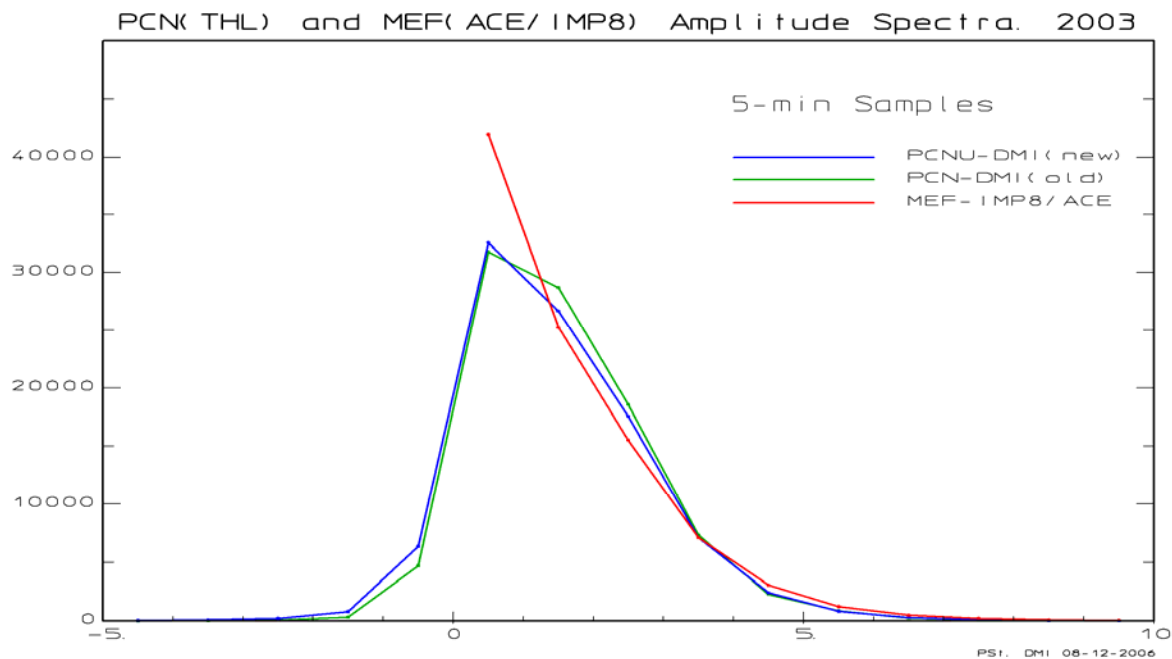


Figure 7.8. Amplitude spectra for PCNU (new), PCN (old) and MEF 5-min samples in year 2003.

7.4. Daily variations of PCN index through seasons and years.

As a further quality check of the PCN index values from different calculations we have in Fig. 7.9. grouped the data for PCN 5-min samples according to month of observation in 12 segments along the horizontal axis, and to year of observations grouped in 6 rows with sequences of 5 years in each (except the first). In the 6 sequences we have 3 sets of solar minimum years (1975-78, 1984-1988, 1994-1998) and 3 sets of solar maximum years (1979-1983, 1989-1993, 1999-2003).

The horizontal axis displays UT time from 00 to 24 hours for each of the 12 segments. Each row of the vertical axis displays PCN index value or MEF (mV/m) on a scale from 0 to 2.0. The colour coding of traces indicate the source of data.

In this representation the quality criterion is that the PCN trace should closely follow the variations in the MEF-IMP8/ACE trace (red). Except for possible large singular intervals of particular solar wind events and irregular fluctuations the MEF traces are all expected to be flat since no variation with UT time (Earth rotation) is expected. The PCN traces should behave similarly and they certainly do. The green (PCN-DMIold) and blue (PCN-DMInew) traces are both close to the red (MEF-IMP8/ACE) trace. In this representation is not possible to determine which index series is the better in this respect

Finally, a black trace for yearly (all year) MEF averages based on OMNI hourly values of solar wind velocities and interplanetary magnetic field at the Earth is included for reference. One may note that the OMNI hourly average values of the merging electric field are systematically smaller than the values derived from either IMP 8 or ACE satellites. This is probably related to non-linear effects in the calculation of the merging electric field such that the product of averages is less than the average of the product of parameters.

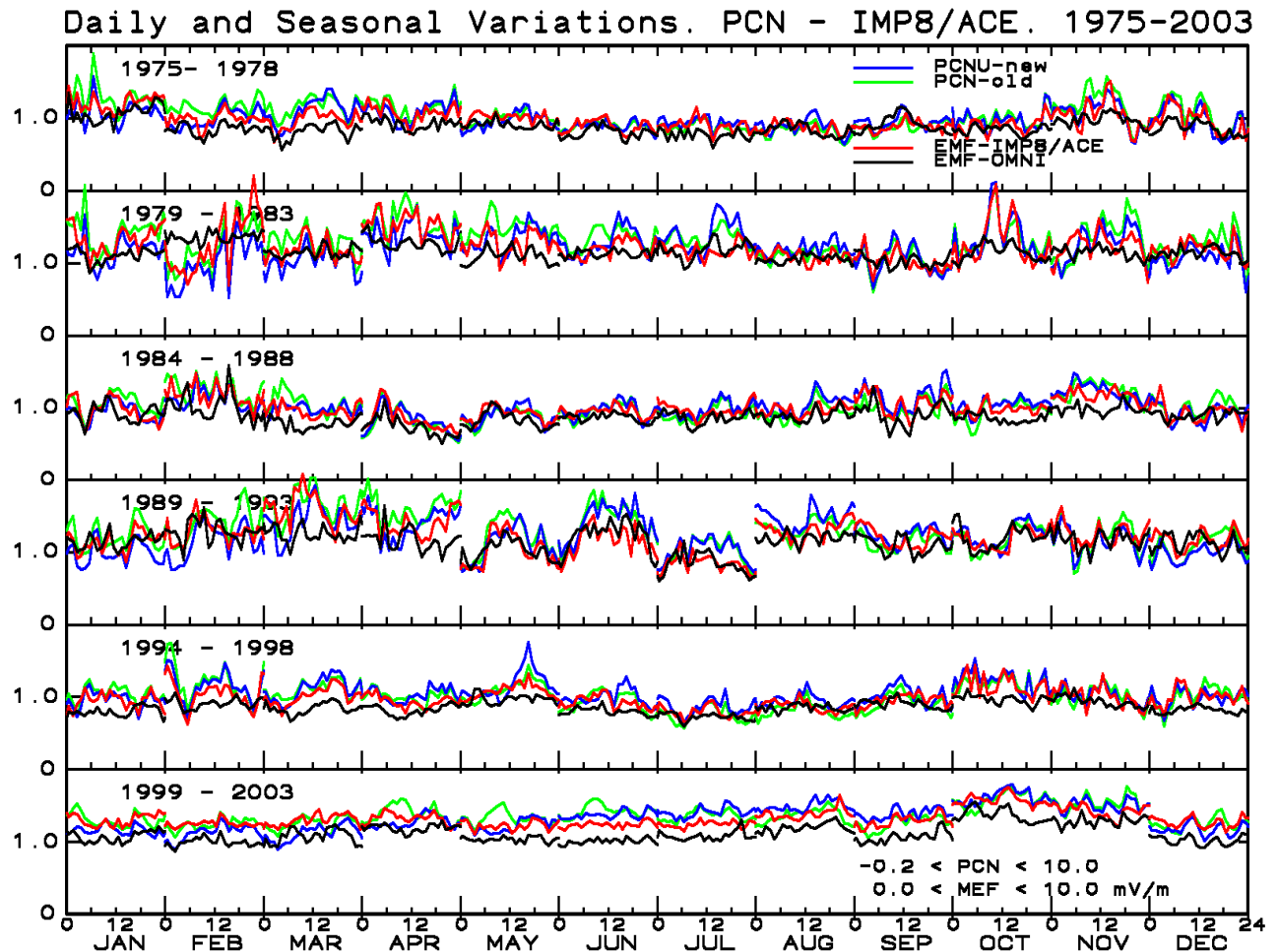


Figure 7.9. UT variations of grouped monthly and grouped yearly averages of PCN index from different calculations, as well as merging electric field values MEF-IMP8/ACE and MEF-OMNI. PCN data are only included if index value is larger than -0.2 and there are valid IMP8/ACE data.

In a further quality check of the PCN index values from different sources we have in Fig. 7.10. grouped the data for PCN 5-min samples in three columns according to season, i.e. winter, equinox and summer, and to year of observations grouped in 6 rows with sequences of 5 years each. In the 6 sequences here, like in Fig. 7.9., we have displayed 3 sets of solar minimum years (1975-78, 1984-1988, 1994-1998) and 3 sets of solar maximum years (1979-1983, 1989-1993, 1999-2003).

The horizontal axis displays UT time from 00 to 24 hours for each of the three columns. The vertical axis displays PCN index value or MEF (mV/m) from 0 to 2.0 in each row. The colour coding of traces is the same as that used in Fig. 7.9.

Here again, the quality criterion is that the PCN traces should follow the variations in the MEF-IMP8/ACE trace (red) as closely as possible. The MEF traces are all expected to be flat and the PCN traces should behave similarly. And, again, the green (PCN-DMIold) and blue (PCNU-DMI) traces, interchangeably, are closer to the red (MEF-IMP8/ACE) trace.

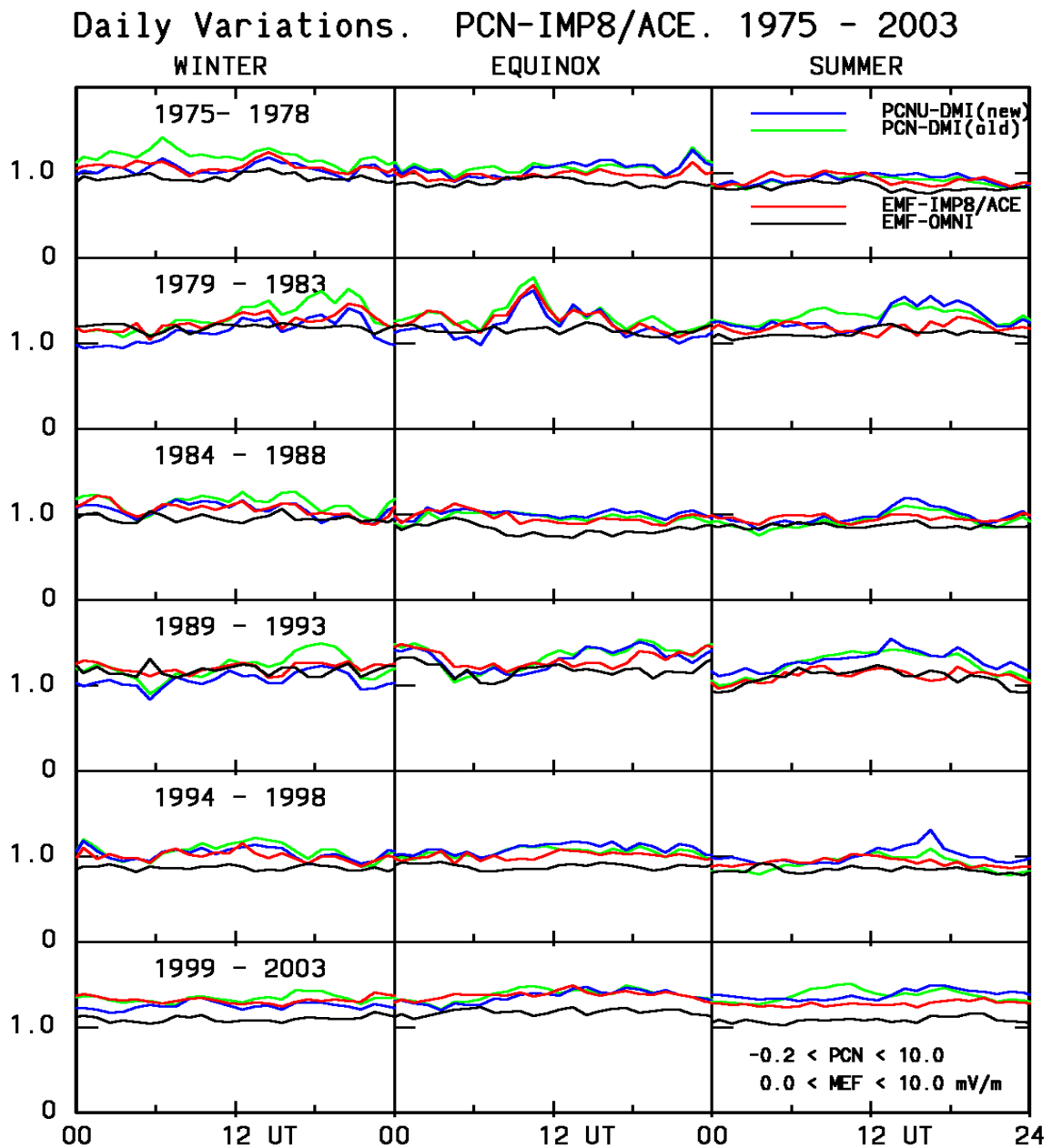


Figure 7.10. UT variations of grouped seasonal and yearly averages of PCN index from different sources and PCS-AARI, as well as merging electric field values MEF-IMP8/ACE and MEF-OMNI. PCN data are only included if larger than -0.2 and there are valid IMP8/ACE data.

7.4. Yearly averages of PCN and MEF values.

We have calculated the yearly average values of the 5-min PCN values derived from the two different procedures. Like above we have only included values of the PCN index larger than -0.2 selected from intervals with valid satellite data. Further included are traces for the MEF derived from either IMP 8 (1975-1998) or ACE (1999-2003) and from the OMNI hourly data series (1975-2003). The results are presented in Fig. 7.11. Each source of PCN or MEF is represented with a trace of different colour.

The plotted traces all show the expected large-scale variations with the 11-year solar activity cycle, that is, larger PC index and MEF values during intervals of maximum solar activity. It is seen that the blue (PCNU-DMI) trace is generally closer to the red trace (MEF-IMP8/ACE) than the green (PCN-DMIold) trace.

Finally included in Fig. 7.11. for reference is a black trace for yearly (all year) MEF averages based on OMNI hourly values of solar wind velocities and interplanetary magnetic field at the Earth.

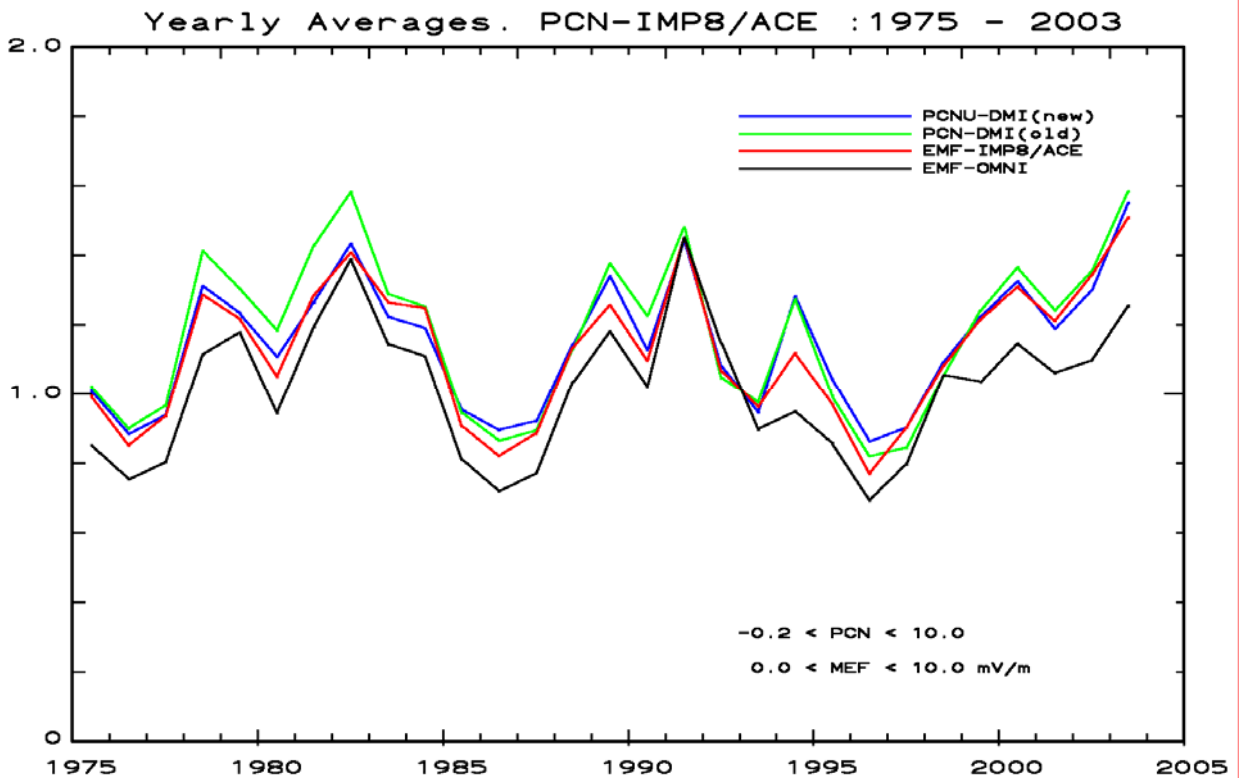


Figure 7.11. Yearly averages of PCN index from different calculations (with and without QL correction for comparison with merging electric field MEF-IMP8/ACE and MEF-OMNI).

Generally, in Fig. 7.11. the blue trace (PCNU-DMI) is closer to the red trace (MEF-IMP8/ACE) than the green trace (PCN-DMIold). This impression is substantiated by the calculations of the average deviation, S0, the average numerical (robust) deviation, S1, and the RMS deviation, S2, between yearly PCN average index values and MEF values (in units of mV/m). The results are presented in Table 7.1.

Table 7.1. Comparison of average deviations of PCN index values from MEF 1975-2003.

PCN index - MEF value	PCN-DMI (old)	PCNU-DMI (new)
Average deviation, S0	0.052	0.023
Numerical deviation, S1	0.059	0.038
RMS deviation, S2	0.074	0.048

Summary and Conclusions

Calculation of QL and scaling parameters.

The main steps of the new unified procedure to calculate the scaling parameters are the following:

1. Thule magnetic field 1-min values are resolved into geographic X- and Y-components.
2. Magnetic field values are corrected for basis level with its secular variations updated daily.
3. Quiet level (QL) values are derived from averaging of data weighted according to hourly minimum level of variability and with respect to time-of-day differences and differences of day in solar rotation phase relative to the epoch in question.
4. Magnetic field values are processed to provide 15-min averages corrected for varying QL values.
5. Merging electric field values in 15-min averages have been derived from IMP 8 (1975-1998) and ACE (1999-2003) solar wind velocities and interplanetary magnetic field data by time shifting (with solar wind speed) to reference position at 12 Re and further delayed 20 min to polar cap.
6. Optimum direction angle (ODA) have been found by correlation analysis (max. correlation) of 15-min samples of projected magnetic variations against merging electric field values derived from IMP 8 or ACE data.
7. Initial ODA values are calculated as averages over 5 years smoothed over time-of-day and month-of-year by 2-D Gaussian function. Final values found as median values through years 1975-2003.
8. Slope parameters have been found by regression analysis as the slope of the regression line for values of the projected magnetic variation (Fv) over merging electric field (MEF). Magnetic variations that would give PC index values below -1. are omitted. Intercept parameters are found from intersect with axis MEF=0 of the line at calculated slope through the centre of gravity for Fv-MEF distribution.
9. Initial slope and intercept values calculated as averages over 5 years smoothed over time-of-day and month-of-year by 2-D Gaussian function. Final values found as median values through years 1975-2003.

QL and scaling parameter data sets.

Optimum direction angle, Slope and Intercept constitute a fixed set of parameters tabulated vs. UT hour and month (they remain invariant over the years). QL data are tabulated vs. UT hour and day for one year at a time. These tabulated data sets are available at the WDC-C1 Data Center at DMI.

Calculation of PCN index

The procedure to calculate PCN index values has the following steps:

1. Thule 1- or 5-min magnetic field average values, corrected for secularly varying base level and for QL level interpolated to 1- or 5-min samples, are projected to the optimum direction.
2. PCN 1- or 5-min values are calculated from these 1- or 5-min corrected and projected field values using slope and intercept parameter values interpolated to 1- or 5-min samples, respectively.

Conclusions.

Based on the quality criteria outlined in Chap. 7 we conclude that the PCN index values (PCNU-DMI) derived at DMI using the unified procedures described in O. Troshichev et al., JGR, (2006) are superior compared to the PCN values (PCN-DMI(old)) derived at DMI using the previously adopted procedures and parameters (S. Vennerstrøm, 1991). Files and graphical presentations of 1-min and 5-min values of the calculated PCN index are available at the WDC-C1 Data Center at DMI.

Acknowledgments

The authors are deeply indebted to Ole Rasmussen, Lars William Pedersen, and Svend-Erik Ascanius for their dedicated efforts to provide magnetic data of utmost quality and continuity from the DMI geomagnetic observatory in Qaanaaq (Thule), Greenland.

References.

- Ahn, B.-H., W. Kroehl, Y. Kamide, and E.A. Kihn, Universal time variations of auroral electrojet indices, *J. Geophys. Res.*, 105, 267, 2000.
- Ahn, B.-H., W. Kroehl, Y. Kamide, and E.A. Kihn, Seasonal and solar cycle variations of the auroral electrojet indices, *J. Atmos. Solar-Terr. Phys.*, 62,1301,2000.
- Ballatore, P., C.G. MacLennan, M.J. Engebretson, M. Candidi, J. Bitterly, C.-I. Meng, and G. Burns, A new southern high-latitude index, *Ann. Geophys.*, 16, 1589, 1998.
- Ballatore, P. and C.G. MacLennan, Significance of the high-latitude geomagnetic index AES-80: comparison with the PC index, *Earth, Planets and Space*, 51 (6), 425-430, 1999.
- Bargatze, L.F., D.N.Baker, R.L.McPherron, and E.W.Hones, Magnetospheric impulse response for many levels of geomagnetic activity, *J.Geophys. Res.*, 90, 6387, 1985.
- Boudaridis, A., E. Zesta, L.R. Lyons, et al., Enhanced solar wind geoeffectiveness after a sudden increase in dynamic pressure, *J. Geophys. Res.*, 110, A05214, doi:10.1029/2004JA010704, 2005.
- Chun, F.K., Knipp, D.J, McHarg, M.G., Lu, G., Emery, B.A., Vennerstroem, S., Troshichev, O.A., Polar cap index as a proxy for hemispheric Joule heating, *Geophys. Res. Lett.*, 26 , 1101-1104, 1999.
- Chun, F.K., D.J. Knipp, M.G. McHarg, J.R.Lacey, G.Lu, and B.A.Emery, Joule heating patterns as a function of polar cap index, *J. Geophys. Res.*, 107(A7), doi:10.1029/2001JA000246, 2002.
- Huang, C.-S., Variations of polar cap index in response to solar wind changes and magnetospheric substorms, *J. Geophys. Res.*, 110, A 01203, doi:10.1029/2004JA10616, 2005.
- Kan, J.R., L.C.Lee, Energy coupling function and solar wind-magnetosphere dynamo, *Geophys. Res. Lett.*, 6, 577, 1979.
- Kokubun, S., Relationship of interplanetary magnetic field structure with development of substorm and storm main phase, *Planet. Space Sci.*, 20, 1033, 1972.
- Lee, D.-Y., L.R. Lyons, and K. Yumoto, Sawtooth oscillations directly driven by solar wind dynamic pressure enhancements, *J. Geophys. Res.*, 109, A04202, doi: 10.1029/2003JA010246, 2004.
- Liou, K., J.F.Carbary, P.T.Newell, C.I.Meng, and O.Rasmussen, Correlation of auroral power with the polar index, *J. Geophys. Res.*, 108(A3), 1108, doi:10.1029/2002JA009556, 2003
- Lukianova, R., Magnetospheric response to sudden changes in solar wind dynamic pressure inferred from polar cap index, *J. Geophys. Res.*, 108, A12, 428, doi: 10.1029/2002JA009790, 2003.
- Lukianova R., O. Troshichev, and G. Lu, The polar cap magnetic activity indices in the southern (PCS) and northern (PCN) polar caps: consistency and discrepancy, *Geophys. Res. Lett.*, 29(18), 1879, doi: 10.1029/2002GL015179, 2002.
- MacLennan, C.G., P. Ballatore, M.J. Engebretson, and L.J. Lanzerotti, A southern high latitude geomagnetic index: AES-80, Antarctic J. of the U.S., 32 (5), 193, 1997.
- Nagatsuma T., Saturation of polar cap potential by intense solar wind electric fields, *Geophys. Res. Lett.*, 29, (10), 62/1-4, 2002.
- Papitashvili, V. O., and O. Rasmussen, Effective area for the northern polar cap magnetic activity index, *Geophys. Res. Lett.*, 26 (19), 2917-2920, 1999.
- Papitashvili, V.O., B.A. Belov, D.S. Faermark, Ya.I. Feldstein, S.A. Golyshev, L.I. Gromova, and A.E. Levitin, Electric potential patterns in the northern and southern polar regions parameterized by the interplanetary magnetic field, *J. Geophys. Res.*, 99, 13,251, 1994.
- Papitashvili V.O., I.I. Gromova, V.A.Popov, and O.Rasmussen, (2001), Northern Polar Cap magnetic activity index PCN: Effective area, universal time and solar cycle variations, *Scientific Report 01-01*, Danish Meteorological Institute, Copenhagen, Denmark, 57 pp., 2001.
- Papitashvili, V.O., N.E. Papitashvili, and J.H. King, Solar cycle effects in planetary geomagnetic activity: Analysis of 36-year long OMNI dataset, *Geophys. Res. Lett.*, 27, (17), 2797-2800, 2000.
- Petrukovich, A.A. and A.A.Rusanov, AL index dependence on the solar wind input revisited, *Adv. Space Res.*, 36, 2440-2444, 2005.
- Ridley A.J. and E.A.Kihn, Polar cap index comparisons with AMIE cross polar cap potential, electric field, and polar cap area, *Geophys. Res. Lett.*, 31, L07801, doi:10.1029/2003GL019113, 2004.

- Russell, C.T., and R.L. McPherron, Semiannual variation of geomagnetic activity, *J. Geophys. Res.*, 78, 92, 1973.
- Shue, J.-H., and D.R. Weimer, The relationship between ionospheric convection and magnetic activity, *J. Geophys. Res.*, 99, 401, 1994.
- Stauning, P. and F. Primdahl, First detection of global dawn-dusk ionospheric current intensities using Ampères integral law on Ørsted orbits, *Geophys. Res. Lett.*, 27 (20), 3273-3276, 2000.
- Stauning, P., J.F. Watermann, and O. Troshichev, Transpolar and ionospheric currents derived from Ørsted and from ground, ESA Proceedings: First SWARM Science Meeting, Nantes, 2006.
- Suzuki, A. and N. Fukushima, Sunward or anti-sunward electric current in space below the MAGSAT level, *Geophys. Res. Lett.*, 9, 345, 1982.
- Takalo, J. and J. Timonen, On the relation of the AE and PC indices, *J. Geophys. Res.*, 103, 29393, 1998.
- Troshichev, O. A., Polar magnetic disturbances and field-aligned currents, *Space Sci. Rev.*, 32, 275-360, 1982.
- Troshichev, O.A., and R.Lukianova, Relation of the PC index to the solar wind parameters and substorm activity in time of magnetic storm, *J. Atmos. Solar.Terr. Phys.*, 64, 585, 2002
- Troshichev, O. A., and V. G.Andrezen, The relationship between interplanetary quantities and magnetic activity in the southern polar cap, *Planet. Space Sci.*, 33, 415, 1985.
- Troshichev, O. A., V. G. Andrezen, S. Vennerstrøm, and E. Friis-Christensen, Magnetic activity in the polar cap – A new index, *Planet. Space Sci.*, 36, 1095, 1988.
- Troshichev, O., H. Hayakawa, A. Matsuoka, T. Mukai, and K. Tsuruda, Cross polar cap diameter and voltage as a function of PC index and interplanetary quantities, *J. Geophys. Res.*, 101, 13,429, 1996.
- Troshichev, O., A.Janzhura, and P.Stauning, Unified PCN and PCS indices: method of calculation, physical sense and dependence on the IMF azimuthal and northward components, *J. Geophys. Res.*, 111, A05208, doi:10.1029/2005JA011402, 2006.
- Troshichev, O. A., R. Yu. Lukianova, V. O. Papitashvili, F. J. Rich, and O. Rasmussen, Polar cap index (PC) as a proxy for ionospheric electric field in the near-pole region, *Geophys. Res. Lett.*, 27, 3809-3812, 2000.
- Vassiliadis, D., Angelopoulos, V., Baker, D.N., Klimas, A. J., The relation between the northern polar cap and auroral electrojet geomagnetic indices in the wintertime, *Geophys. Res. Lett.*, 23, 2781, 1996.
- Vennerstrøm, S., *The geomagnetic activity index PC*, PhD Thesis, Scientific Report 91-3, Danish Meteorological Institute, 105 pp, 1991.
- Vennerstrom, S., Friis-Christensen, E., Troshichev, O.A., Andrezen, V.G., Comparison between the polar cap index PC and the auroral electrojet indices AE, AL and AU, *J. Geophys. Res.*, 96, 101, 1991.
- Vennerstroem, S., E. Friis-Christensen, O.A.Troshichev, and V.G.Andrezen, Geomagnetic Polar Cap (PC) Index 1975-1993, Report UAG-103, World Data Center A, Boulder, 1994.
- Weimer, D.R., Maps of ionospheric field-aligned currents as a function of the interplanetary magnetic field derived from Dynamics Explorer 2 data, *J. Geophys. Res.*, 106, 12,889-12,902, 2001.

Previous reports

Previous reports from the Danish Meteorological Institute can be found on:

<http://www.dmi.dk/dmi/dmi-publikationer.htm>